ASSESSING THE EFFICIENCY OF REACTIVE OXYGEN SPECIES COLORIMETRIC SENSORS FOR USE IN ENVIRONMENTALLY & BIOLOGICALLY RELEVANT SAMPLES

by

Johanna L. Herman

A dissertation submitted to the Faculty of the University of Delaware in partial fulfillment of the requirements for the degree of Doctor of Philosophy in Chemistry and Biochemistry

Summer 2020

ASSESSING THE EFFICIENCY OF

REACTIVE OXYGEN SPECIES COLORIMETRIC SENSORS

FOR USE IN ENVIRONMENTALLY & BIOLOGICALLY

RELEVANT SAMPLES

by

Johanna L. Herman

Approved: _____

Brian Bahnson, Ph.D.
Chair of the Department of Chemistry & Biochemistry

Approved: _____

John Pelesko, Ph.D.
Dean of the College of Arts & Sciences

Approved: _____

Douglas J. Doren, Ph.D.
Interim Vice Provost for Graduate and Professional Education and
Dean of the Graduate College

I certify that I have read this dissertation and that in my opinion it meets the academic and professional standard required by the University as a dissertation for the degree of Doctor of Philosophy.

Signed: _____

Sharon Neal, PhD.
Professor in charge of dissertation

I certify that I have read this dissertation and that in my opinion it meets the academic and professional standard required by the University as a dissertation for the degree of Doctor of Philosophy.

Signed: _____

Murray Johnston, Ph.D.
Member of dissertation committee

I certify that I have read this dissertation and that in my opinion it meets the academic and professional standard required by the University as a dissertation for the degree of Doctor of Philosophy.

Signed: _____

Tatyana Polenova, Ph.D.
Member of dissertation committee

I certify that I have read this dissertation and that in my opinion it meets the academic and professional standard required by the University as a dissertation for the degree of Doctor of Philosophy.

Signed: _____

Joseph Fox, Ph.D.
Member of dissertation committee

I certify that I have read this dissertation and that in my opinion it meets the academic and professional standard required by the University as a dissertation for the degree of Doctor of Philosophy.

Signed: _____

Pei Chiu, Ph.D.
Member of dissertation committee

ACKNOWLEDGMENTS

I would like to acknowledge and thank the people that have contributed to this dissertation and my development as a researcher and science educator.

Foremost, Professor Sharon Neal has been instrumental in developing my research confidence. She has been a prominent source of wisdom and motivation throughout the research process. Her unwavering support and guidance have expanded my scientific, social, and general knowledge. Her advice remains invaluable to me. Anyone would be lucky to have her as an advisor.

Many fellow graduate students have played a key role in my research and progress. I'd like to thank Natasha Kowaleuski, Erin Holahan, Yinan Zhang, and James Hartman for their contributions to my personal and profession development at the University of Delaware. Each of them, along with too many others name, have played an important role in my acclimation and growth as a graduate student. Together, they are an example of how significant and prized mentorship and community are for graduate students.

Additionally, I would like to recognize Dr. Kathryn Burke, Dr. Jacqueline Fajardo, Dr. Mark Baillie, and Dr. Alenka Hlousek-Radojcic for their guidance and support throughout my journey as a graduate teaching assistant. My teaching abilities have reached many milestones as a result of their dedication and mentoring. They provided numerous opportunities for me to grow and showcase my teaching skills and for that I am very grateful. Because of them, I feel confident moving on to a career in science education.

I would like to acknowledge the Department of Chemistry & Biochemistry at the University of Delaware for their financial support during my graduate studies. I would also like to thank the chemistry department's administrative staff for helping graduate students daily to navigate the many administrative tasks within and outside of our department. Susan Cheadle, Susan James, Lori Nesnow, and Linda Staib, we would be at a loss without each of you.

I am also thankful for the support of my husband, Raymond Herman. From day one, my husband has been present as my cheerleader, a shoulder to rest on, and wine source on the rough days. He tagged along through the department picnics and group Christmas parties, despite his reluctance in being the non–scientist in the room. His encouragement and friendship have been vital to my success.

Finally, I would be remiss to not express my gratitude to my grandmother, Violet Ray. Long before the aforementioned individuals crossed paths with mine, my brilliant grandmother cultivated a curiosity within me. In always making time for my curiosities, she raised me to be a scientist. From advocating for me in taking over a portion of my grandfather's beloved garden to plant sprouted potatoes I found in her pantry, to many other adventures completed just because I wanted to see what would happen. No matter the occasion or how busy she was, whatever the question or curiosity, she took time to help me address it, often finding answers in her encyclopedia collection, old newspapers, or through animal planet and the discovery channel. I am very grateful that my grandmother took the time to teach me a wide variety of skills and perspectives throughout my youth. Without her influence, I may not be the curious, persistent, and open–minded scientist I am today. For these reasons, I dedicate this dissertation to her.

TABLE OF CONTENTS

LIST OF TABLES

LIST OF FIGURES

LIST OF REACTION SCHEMES

ABSTRACT

A longstanding interest in reactive oxygen species (ROS) stems from their role in many environmental, biological, clinical, and industrial processes. Molecular spectroscopic methods have largely dominated the field of ROS detection due to its many advantages for real–time, localized, in *situ* analysis, with comparatively modest equipment cost and expertise requirements. This has led to a focus on spectral detection of ROS, and many advances in ROS sensor technologies for spectrophotometric (colorimetric) and luminescence measurements. Although many advances in ROS sensor technologies for spectrophotometric and luminescence measurements have been made to enhance selectivity and time response in ROS detection, there has been less attention given to the impact of sample complexity on sensor measurements. ROS are typically generated and evolve in complex settings, making their detection and quantification challenging. Often, detecting a change in a system's redox status is generally attainable, but accurate quantification is not, and poor selectivity of many classic and novel ROS sensors increases the incidence of overinterpretation of results by the scientific community.

The objective for the research contained in this dissertation is to demonstrate the efficiency, or lack thereof, of select commercially available colorimetric ROS sensors for their use in environmentally and biologically relevant samples, as well as investigate potential improvements to the analysis of optical data resulting from sensor measurements using a vigorous series of control measurements and numerical analysis strategies. In this dissertation sensor stability was evaluated using two types of assay

control measurements: broadband molar absorptivity, and photostability under broadband simulated sunlight. Then, an efficiency comparison of the imidazole plus RNO method for singlet oxygen detection in biorelevant solvents was compared to reference solvents using Rose Bengal photosensitization to produce $^1O_2$ and time-resolved, broadband UV–Vis absorbance measurements to simultaneously monitor sensor and sensitizer response profiles. In the final chapter, the impact of combining the results of systematically varied assays and controls on the analysis of colorimetric data collected using the Imd plus RNO method was investigated using a combination of numerical analysis strategies.

Chapter 1

INTRODUCTION

1.1 Motivation

Reactive oxygen species (ROS) are reactive, energetic short–lived molecules, radicals, or ions containing oxygen atoms. Singlet oxygen ($^1O_2$), superoxide ($O_2^{\bullet-}$), hydroxyl radical ($OH^{\bullet-}$), and hydrogen peroxide (H_2O_2) are most commonly listed as leading factors in ROS processes. A longstanding interest in ROS is a result of their central role in many environmental, biological, clinical, and industrial processes.[1] In environmental settings, ROS are typically generated by photolysis or photosensitization; the photo–sensitive molecules that lead to ROS production are called photosensitizers, and are a focus of this research. In biological systems, ROS can be generated endogenously during photosynthesis or respiration, or exogenously in response to xenobiotic exposure. ROS have also been connected to signaling pathways in cells, central to biological responses to pathogens, pollutants, and radiation;[2] reflecting a dual nature as both defense and signaling molecules.[3] The reactive and destructive nature of ROS has been exploited in many clinical and industrial applications. ROS have been used for wastewater remediation,[4] photodynamic therapy,[5] blood sterilization, and insecticides and herbicides.[6] Their broad range of application and complex phenomena motivates ROS as important analytical targets.

Many linear and nonlinear optical transitions have been used or suggested for ROS detection focused on exploiting interaction between the analyte of interest (the ROS) and electromagnetic radiation. Linear transitions include: single–photon

absorption, fluorescence, phosphorescence, chemiluminescence, and resonance Raman transitions. Nonlinear transitions include: two–photon absorption and fluorescence, second harmonic generation, sum–frequency generation, coherent anti–Stokes Raman scattering, and simulated Raman scattering. While electrochemical, mass spectrometric, and separation methods have also been used to detect ROS, molecular spectroscopic methods have many advantages for real–time, localized, in *situ* analysis, with comparatively modest equipment cost and expertise required.[7–9] This has led to a focus on spectral detection of ROS, and many advances in ROS sensor technologies for spectrophotometric (colorimetric) and luminescence measurements.[10–12] In the last decade, ROS sensor development has continued at an increasing rate, with less focus on spectrophotometric measurements and sustained emphasis on luminescence detection.[13] As can be expected, recent sensor advances are aimed at reducing detection limits, increasing selectivity, and reducing response times during analysis.

Countless approaches to increasing the selectivity of spectral measurements while lowering or maintaining detection limits have been used in novel and classic ROS studies. Two major lines of advances have emerged: physically or chemically isolating the analyte, or isolating the analyte signal in multicomponent response signal(s). Chromatography and electrophoresis are commonly used as physical separation tactics, while chemical reagents or sensor molecules can also be used to isolate the analyte on the basis of chemical reaction or molecular recognition; the goal in either case being to make the analyte the only sample component producing the signal at the detector. On the other hand, response signals have been isolated optically, electronically, and computationally. For example, ratiometric (dual–wavelength) spectral measurements, time–resolved spectral measurements, and “hyphenated” methods (combining two, or

more, measurement domains—i.e. paring broadband, multichannel spectral detection with time or electrical potential) have all been used to improve analyte detection. Though these methods often require multicomponent chemometric analysis for signal isolation.

Although there is increasing appreciation for the need for enhanced selectivity and time response in ROS detection, there has been less attention given to the complexity of most samples that present substantial challenges to accurate in *situ*, multicomponent ROS measurements. ROS are typically generated and evolve in complex settings and in multiples (multiple ROS), making their detection and quantification challenging. Winterbourn[14] described in 2014 that complete characterization of complex ROS processes requires detection, identification, localization, monitoring, and quantification; she concluded that these steps are increasingly difficult, particularly in *vivo*. Often, detecting a change in a system's redox status is generally attainable, but accurate quantification of individual ROS is not. Poor selectivity of many classic and novel ROS sensors increases the incidence of overinterpretation of results by the scientific community. Recognizing these limitations in ROS detection and quantification, as a few recent reports have done,[12,13,15–17] is crucial as the field of ROS detection continues forward.

1.2 Objectives & Project Outline

The objective for the research contained in this dissertation is to demonstrate the efficiency, or lack thereof, of select commercially available colorimetric ROS sensors for their use in environmentally and biologically relevant samples, as well as investigate potential improvements to the analysis of optical data resulting from sensor measurements using a vigorous series of control measurements and numerical analysis

strategies. Fundamental methodology for the instrumentation—including broadband UV–Vis spectrophotometry and solar simulation—and data analysis—including singular value decomposition and non–negative matrix factorization—used for the research contained in this dissertation are described in **Chapter 2**.

The first study, presented in **Chapter 3**, is a compilation of the stability controls used to initially assess the use of selected common ROS sensors in environmentally or biologically relevant samples. Sensor stability was evaluated using two types of assay control measurements: broadband molar absorptivity, and photostability under broadband simulated sunlight. The stability of three singlet oxygen sensors—1,3-diphenylisobenzofuran (DPBF), 9,10-anthracenedipropionic acid (ADPA), and p-nitrosodimethylaniline (RNO) plus imidazole (Imd)—in addition to three superoxide sensors—7-chloro-4-nitrobenzo-2-oxa-1,3-diazole (NBD-Cl), 1,4-benzoquinone (BQ), and 3-(4,5-dimethyl-2-thiazol)-2,5-di-phenyl-2H-tetrazolium bromide (MTT)—were evaluated. Out of the six sensors, two were determined acceptable for use in the proposed environmentally and biologically relevant conditions the Imd plus RNO method for $^1O_2$ detection, and the MTT sensor for $O_2^{\bullet-}$ detection. Due to the instability observed in the reaming sensors, caution and attention to control measurements are suggested when using these, and potentially other, ROS chemical sensors in the environmentally and biologically relevant conditions of this, and similar, work.

The second study, presented in **Chapter 4**, is an efficiency comparison of the imidazole plus RNO method for singlet oxygen detection in biorelevant solvents. In this research, the efficiency of the Imd/RNO method in complex, biorelevant solvents was compared to reference solvents using Rose Bengal photosensitization to produce $^1O_2$ monitored using time-resolved, broadband UV–Vis absorbance measurements. Rates of

sensor bleaching and sensitizer photodegradation were simultaneously monitored in each solvent to investigate correlations between the disappearance rates of sensor and sensitizer. To illustrate the efficiency of the method across the solvents, the quantum yields of $^1O_2$ production in each solvent were calculated using a relative actinometric method. The dependence of sensor bleaching and sensitizer degradation on acceptor concentration and solvent polarity, and the results of assay controls indicate differences in mechanisms underlying the reactions comprising the Imd/RNO method. These results demonstrate the need for caution and controls when using the method in complex samples including those containing cells, tissues or nanoscale particles. Much of the contents of this chapter have been published previously.[18]

The last study of this dissertation, presented in **Chapter 5**, is an attempt to increase the accuracy of colorimetric data analysis using numerical analysis strategies to isolate or reject overlapping concomitant signals. In this work, singular value decomposition[19] and non–negative matrix factorization[20] were used to resolve isolated chromophore spectral and response profiles from colorimetric data resulting from the use of the Imd plus RNO method. Spectral isolation was improved through concatenation of a series of control and ROS assay measurements—including molar absorptivities, photodegradation controls, and assay data with varied initial reagent concentration. The resulting resolved response profiles for assay reagents of the Imd plus RNO method were then subjected to kinetic profiling, to compare resolved reaction rate constants to those determined by the traditional single–wavelength analysis approach.

Chapter 2

METHODOLOGY

2.1 Abstract

This chapter describes the methods used to monitor oxygen photosensitization reactions of photosensitizers and reactive oxygen species (ROS) sensors using time resolved UV–Vis spectroscopy and a Xe arc lamp solar simulator paired with traditional, single–wavelength kinetic analysis, and broadband numerical analysis strategies.

2.2 Materials

2.2.1 Model Photosensitizer

Rose Bengal was selected as the model photosensitizer for this work, as a reliable source of $^1O_2$. RB is a commonly and widely used photosensitizer due to its intense absorption band, and high $^1O_2$ quantum yields (ϕ_Δ).

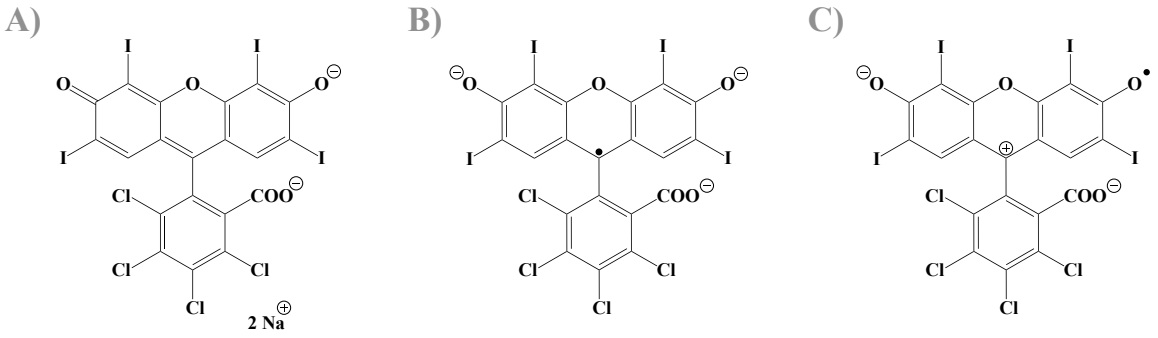

Figure 2.1: Structures of **A)** ground state Rose Bengal (RB^{2-}), and its **B)** reduced ($RB^{\bullet 3-}$) and **C)** oxidized ($RB^{\bullet -}$) forms.[21]

Rose Bengal (2,4,5,7–tetraiodo–3',4',5',6'–tetrachlorofluorescein, RB^{2-}), originally synthesized by Gnehm[22] as a fabric dye, has a strong absorption band near 550 nm. The intersystem crossing of the singlet excited dianion (RB_1^{2-}) into the fairly long–lived ($t_{1/2}$ = 0.1–0.3 ms)[23] triplet excited state (RB_3^{2-}) is very efficient, with a triplet quantum yield (ϕ_T) greater than 0.90 in both water and methanol[21]. The photochemistry of RB has been characterized previously[21,22] and **Scheme 2.1** summarizes the photochemistry steps following RB^{2-} excitation. After transformation into RB_3^{2-} (**Scheme 2.1a**), there are a number of pathways by which the excited triplet can decay: RB_3^{2-} can decay to the ground state (k_d, **Scheme 2.1b**), undergo bimolecular self–quenching (k_{sq}, **Scheme 2.1c**), exchange an electron with a ground state RB to give the reduced (**Scheme 2.1b**) and oxidized (**Scheme 2.1c**) RB forms (k_{redox^1}, **Scheme 2.1d**), undergo triplet–triplet annihilation to give the ground state and singlet RB states (k_{TT}, **Scheme 2.1e**), or disproportionate with another triplet to give the ground state redox pair (k_{redox^2}, **Scheme 2.1f**). Eventually, any formed redox pairs of RB undergo back electron transfer to form ground state RB (k_{-et}, **Scheme 2.1g**).

In addition to the many pathways outlined above, RB's relatively long–lived triplet excited state (RB_3^{2-}) is highly effective at transferring energy to ground state molecular oxygen ($^3O_2$) with a ϕ_Δ of 0.75 in water and 0.86 in methanol.[24,25] The process of RB producing $^1O_2$ is described in **Scheme 2.1h**, which occurs when a triplet excited RB molecule reacts with a ground state oxygen molecule, undergoing an energy transfer, also known as type II photosensitization.

RB (Aldrich Chem. Co., 95%) was purchased and used as received, without further purification. Stocks of RB were prepared by solvation in ethanol, then wrapped in tin foil (due to light sensitivity), refrigerated, and monitored by UV–Vis absorption

spectroscopy for signs of decay or contamination, and discarded if the absorption profile visually changed, or the peak absorption decreased by more than 5%.

(a) $RB^{2-} \xrightarrow{1.\ h\nu} RB_1^{2-} \xrightarrow{2.\ ISC} RB_3^{2-}$

(b) $RB_3^{2-} \xrightarrow{k_d} RB^{2-}$

(c) $RB_3^{2-} + RB^{2-} \xrightarrow{k_{sq}} 2\ RB^{2-}$

(d) $RB_3^{2-} + RB^{2-} \xrightarrow{k_{redox}1} RB^{\bullet-} + RB^{\bullet 3-}$

(e) $RB_3^{2-} + RB_3^{2-} \xrightarrow{k_{TT}} RB_1^{2-} + RB^{2-}$

(f) $RB_3^{2-} + RB_3^{2-} \xrightarrow{k_{redox}2} RB^{\bullet-} + RB^{\bullet 3-}$

(g) $RB^{\bullet-} + RB^{\bullet 3-} \xrightarrow{k_{-et}} 2\ RB^{2-}$

(h) $RB_3^{2-} + {}^3O_2 \xrightarrow{k_\Delta} RB^{2-} + {}^1O_2$

Scheme 2.1: Photophysical & photochemical reaction characteristics of Rose Bengal's photodegradation.[21,26]

2.2.2 Biorelevant Media

The aim of this work is comparing the performance of reactive oxygen species sensors in typical aqueous and isotropic solvents, like phosphate buffer (PB), methanol (MeOH) and ethanol (EtOH), to their performance in more complex microheterogeneous solvents, like sodium dodecyl sulfate (SDS), octanol (OctOH), and phosphate buffer saturated octanol (PBOctOH). SDS, OctOH, and PBOctOH were selected for their biomimetic and geomimetic properties. For example, octanol-water partition coefficients are commonly used to predict the pharmacokinetic characteristics of drug compounds and the toxicity and transport of pollutants in soil and groundwater systems.[27] Octanol was also selected for its structural microheterogeneity,[27,28] its

capacity to self-assemble into predominantly hydrophilic and hydrophobic regions, like the aqueous micellar solution, sodium dodecyl sulfate, to some extent. The impact of this feature on the method was investigated using phosphate buffer saturated octanol (PBOctOH), which is approximately 26% aqueous buffer.[28]

Sodium lauryl (dodecyl) sulfate (Fisher Scientific), OctOH (99% pure, Acros Organics), MeOH (HPLC grade, Fisher Chemical), EtOH (Decon Laboratories, Inc.), and HPLC-grade lab water (HOH, Fisher Chemical) were purchased and used as received. PB was prepared by combining 1.0 M sodium phosphate dibasic (Na_2HPO_4, Fisher Scientific) and 1.0 M sodium phosphate monobasic (NaH_2PO_4, Fisher Scientific) in a 7.74:2.26 volume ratio, then diluted with HOH; resulting in a buffer salt concentration of 0.01 M, and pH of approximately 7.4 (as measured by glass electrode). SDS 5% micellar solution was prepared by dissolving 25 grams of sodium lauryl (dodecyl) sulfate into 500 mL HOH. PBOctOH was prepared by combining an equal volume ratio of PB and OctOH, vigorously stirring on an electronic stir box for approximately 4–6 hours, and then allowing the mixture to rest for at least 72 hours before removing the organic phase for use.

2.3 Instrumentation

2.3.1 Broadband UV–Vis Absorbance

For this work, UV–Vis spectroscopy was used to monitor reaction progress. UV–Vis spectroscopy has been used widely for ROS detection in aqueous environments, despite its higher detection limit, principally due to its convenience, low cost, and portability. All spectral data was collected on a diode array spectrophotometer (HP, 8452A) calibrated with an air or solvent blank. Samples were contained in either

a 10 mm path length, opened top UV quartz cuvette (FireflySci, type 21), or a 10 mm path length, capped UV quartz cuvette, fitted with a SEPTA screw cap (FireflySci, type 41). For reaction progress monitoring, time–resolved spectra were obtained by manually moving the sample cuvette from in front of the solar simulator, to the sample compartment of the spectrophotometer, and manually collecting a sample spectrum.

To convert absorbance spectra into concentration vectors, molar absorptivities for each chemical reagent were obtained using solutions that have exponentially increasing concentrations. Starting with 1.8–2.0 mL of solvent in a 3.50 mL cuvette, microliter additions of stock solution were added to the cuvette, and spectra collected on the diode array spectrophotometer. The concentration sets (with 15–25 total measurements) were chosen to have a minimum absorbance of 0.1 and maximum absorbance of 3.0, as estimated from reference molar absorptivities in ethanol. Molar absorptivities were completed in quadruplicates; two trails where the spectrophotometer was calibrated with an air blank (empty cuvette), and two with a solvent blank (cuvette with solvent only). Absorption spectra were then used to construct a Beer's Law plot of absorbance versus concentration, and the molar absorptivity computed across the spectrum (190–820 nm) from the slope of the linear line of best fit at each wavelength.

In some cases, sample solutions needed to be purged of oxygen (degassed) to investigate the impact of an oxygen–free solution. To do so, the solution was contained in the capped UV quartz cuvette, and two HPLC–type needles (Hamilton) with beveled, curved non–coring points were pierced through the SEPTA of the screw cap. The first needle was 25–gauge and used as a pressure release for the purge gas, and was kept in the cuvette headspace above the solution. The second needle was 20–gauge and fitted to a 5 mm diameter hose connected to a nitrogen tank valve. This needle was pushed

through the septum and submerged in the solution, and left to aerate the solution for 30–60 minutes, depending on the solvent. A stir bar and stir plate was also used to mix the solution throughout the degassing process. When a solution like 5% sodium dodecyl sulfate (SDS) was degassed, in which bubbles formed during the degassing process, a third needle, of 20–gauge, was fitted to a second 5 mm diameter hose connected to the same nitrogen tank using a T–shaped connector. This needle was pushed through the septum and kept in the cuvette headspace to suppress any foam that forms at the surface of the solution. Due to the increase in pressure from two gas needles, the 25–gauge pressure release needle was replaced with a 20–gauge needle.

2.3.2 Solar Simulation

An important aspect to monitoring oxygen photosensitization reactions is the light source used to excite the sensitizer. In this work, environmentally significant light conditions are achieved by using a solar simulator, engineered to mimic natural sunlight. The irradiance of the sun on the outer atmosphere is approximately 1367 Wm^{-2} (known as the solar constant, I_{SC}); out of convenience, simulated solar irradiance is typically described in units of "suns", where one "sun" is equivalent to one solar constant.[29] Before reaching the ground, solar radiation passes through the atmosphere, becoming modified by absorption and scattering. Most radiation below 190 nm is blocked by atomic and molecular oxygen and nitrogen; which then leads to the production of ozone, and more absorption between 200-300 nm. As shown in **Figure 2.2**, water vapor, carbon dioxide, and molecular oxygen selectively absorb bands in the visible and near–IR regions. During a typical cloudless summer day, at zero zenith angle, the 1367 Wm^{-2} reaching the outer atmosphere is reduced to approximately 1050 Wm^{-2} (0.77 suns)

direct beam radiation, and approximately 1120 Wm^{-2} (0.82 suns) global radiation on a horizontal surface at ground level.[29]

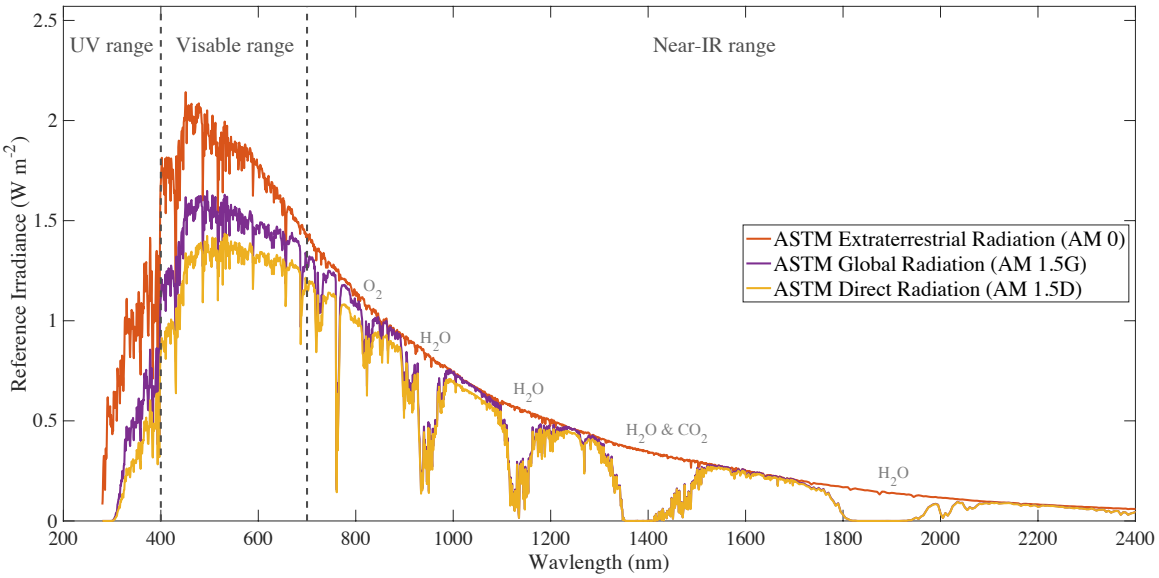

Figure 2.2: Reference solar spectra for extraterrestrial (orange), global (purple), and direct (yellow) at sea level on a clear day. Absorption bands resulting from atmospheric water vapor and carbon dioxide are indicated by labels. Spectral data acquired from ASTM Standard G173-03, 2004.

The amount and profile of radiation experienced on the ground depends on many factors; such as, seasonal variations and trends in the ozone layer, aerosol content, cloud density, and most significantly, the distance the sun's radiation must travel through the atmosphere (affected by elevation, time of year, and day).[30] To account for differences in radiation path length, the distance the radiation travels through the atmosphere at an angle is normalized to the distance directly above (zenith). The direct irradiance is considered the "Air Mass 1" (AM 1); while the irradiance at a zenith angle (θ_z) of 48.2° is considered the "Air Mass 1.5" (AM 1.5), signifying a 50% increase in the distance

the radiation traveled through the atmosphere.[29] Air mass determinations can be made using **Equation 2.1**.

$$AM \simeq P/P_0 = \sec\theta_z \qquad \textbf{2.1}$$

Solar simulator quality is currently graded on 1) spatial uniformity across a defined illumination area, 2) temporal stability through the experiment, and 3) spectral match to the sun as defined by reference spectra put forth by internationally recognized standards bodies—The International Electrotechnical Commission (IEC), Japanese Industrial Standardization (JIS), and The American Society for Testing and Materials (ASTM).[30] Spatial uniformity is an account of the consistency of light over a selected region; for a class A rating, there needs to be less than a ± 2% variation over the test region. Temporal stability is the ability for the instrument to maintain its sun output over long and short–term use; for a class A rating, the simulator must vary by no more than 0.5% over long–term use, and 2% over short term use. Spectral match is a measure of how well a solar simulator mimics the suns output spectrum. There are three established spectra standards used to evaluate a simulators spectral match: AM 0, AM 1.5D, and AM 1.5G, illustrated in **Figure 2.2** above. AM 0 is the irradiance outside of the Earth's atmosphere (zero atmosphere), AM 1.5D is the direct component of the irradiance that strikes the Earth's surface, and AM 1.5G (global) accounts for both the direct and diffuse radiation striking the Earth's surface.[30] The AM 1.5G reference is the most commonly used profile when evaluated the spectral match of solar simulators.

The commercial technology for solar simulation has been largely dominated by the xenon arc lamp for the past 15-20 years. While xenon bulbs experience a loss in intensity and a shift from blue to red in irradiance spectrum as the lamp ages, it is very close to an ideal point source of light with a relatively continuous and uniform spectrum

across the visible region.[31] Typically, filters are used to adjust the UV and IR ranges to more closely match the complete solar spectrum. Other popular lamp and filament choices include tungsten, mercury, and metal halide; though these sources fall much shorter in quality of spectral match to the sun.[29] More recently, advancements have been made in LED technology where a combination of unique LEDs can be used to match solar standards.[32] LED are becoming more popular due to their added spectral control (by tuning the individual LEDs), longer lifetime, reduced heat, and lower power consumption.

In this work, a 300 W xenon arc lamp powered by an ILC Technology PS300–1 power supply, housed in an ILC Technology R400 lamphouse, with built-in heat sink and fan, was used to simulate solar light. To improve spectral matching (to the sun), and reduce the amount of IR light reaching the sample (to lessen sample heating), source light from the lamp was passed through an in–house fabricated, 18 cm long, water filled glass cylinder equipped with a collimating quartz lens at the light entrance, and quartz window at the exit (**Figure 2.3**). The effects of the water filter on the source light are illustrated in **Figure 2.4**. The resulting simulated solar profile in comparison to the ASTM AM 1.5G standard is illustrated in **Figure 2.5**, and shows that the solar simulator used in this work is relatively successful in simulating the visible region of the standard spectrum, with a unit normalized dot product between the reference and simulated solar profiles of 0.82. The simulated solar profile does produce significantly more UV radiation than that found in the reference; this limitation could be alleviated by using long–pass filters (LPF), like a 295 nm LPF to remove more of the deep UV irradiation. Moreover, for the context of this work, the simulator successfully produces a relatively constant irradiance across the visible region, with an average irradiance of

0.0570 ± 0.075 mW/nm between 380–700 nm, as determined by chemical actinometer (described below).

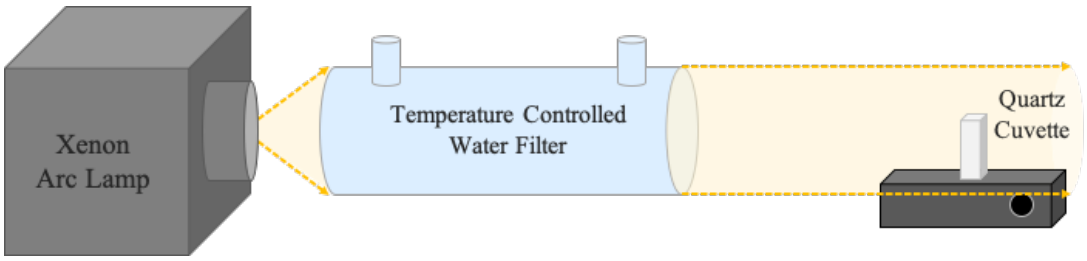

Figure 2.3: Diagram of Xenon solar simulator with a temperature–controlled water filter, and quartz sample cuvette.

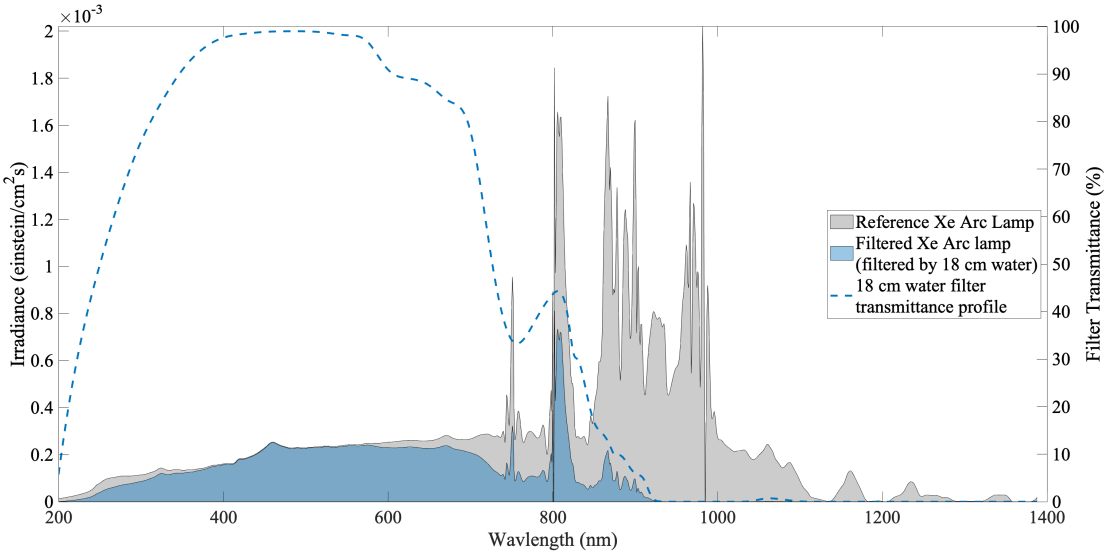

Figure 2.4: Xenon spectral profile before (gray) and after (blue) passing through the 18 cm water filter. The transmittance profile of the 18 cm water filter is included.

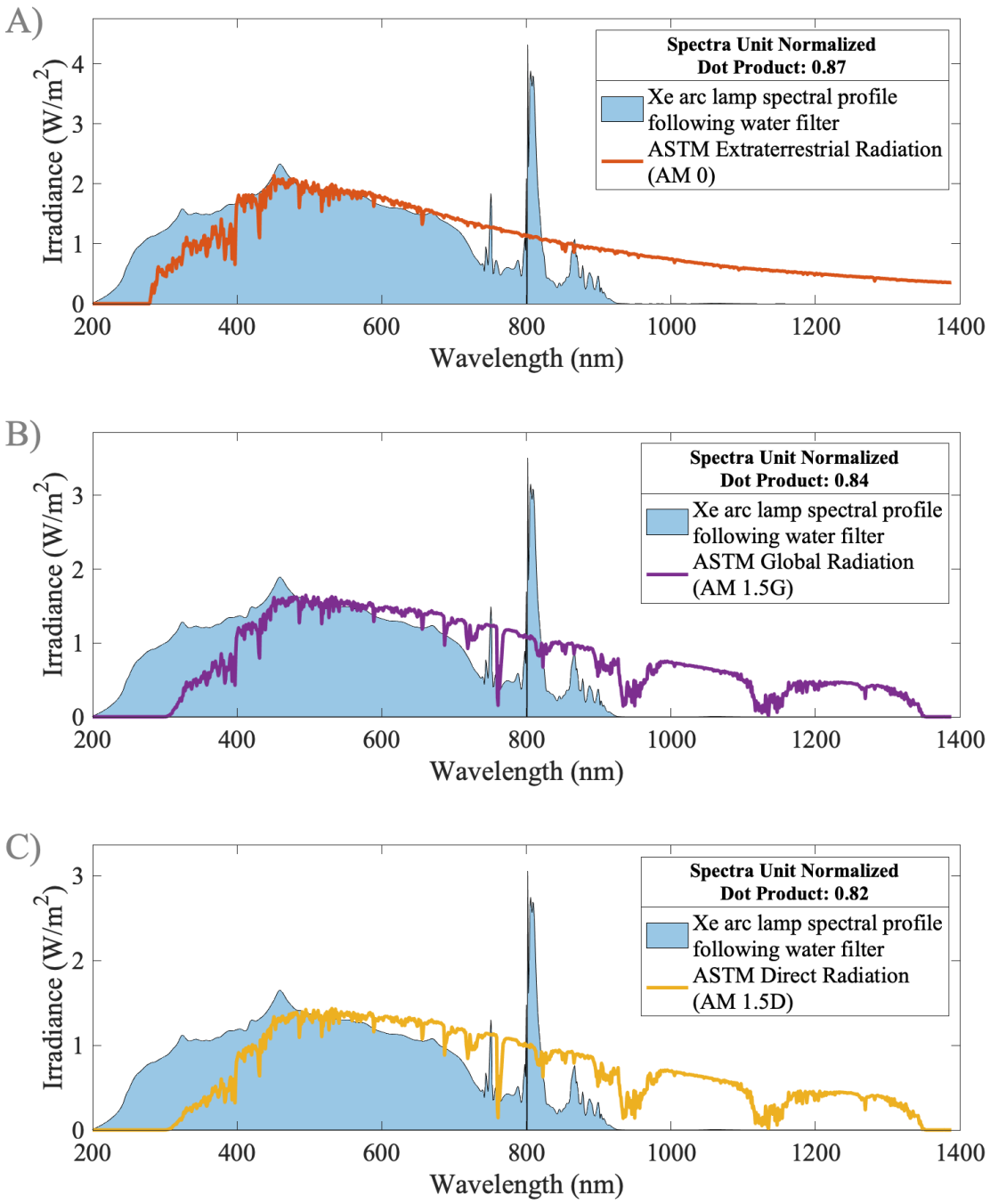

Figure 2.5: Irradiance profile of simulated sunlight compared to the ASTM A) AM 0, B) AM 1.5G, and C) AM 1.5D reference profiles. In each plot, the integrated visible irradiance of the simulated profile was normalized to that of the reference profile.

2.4 Chemical Actinometry

A common, low cost method to quantifying the output of an illumination source is chemical actinometry. A chemical actinometer must meet one main criterion, the chemical must be involved in a well–characterized photo–activated reaction whose quantum yield is well–defined and relatively constant as a function of wavelength. With this, the rate of the chemical reaction can be mathematically related to the number of photons incident on the reaction sample. Potassium ferrioxalate (FeOx) is a widely used, stable and sensitive, zero–order chemical actinometer introduced by Hatchard and Parker[33] in the 1950's, that has since been extensively characterized.[34] function of the actinometer is based on the strong UV and partial visible (~250–500 nm)[35] absorption of the FeOx complex, which leads to the reduction of Fe(III) to Fe(II). The total process of the actinometric photolysis is represented in **Reaction 2.1**.[34] After its reduction, the iron is no longer complexed by the oxalate and can then be detected colorimetrically by complexing with a developing agent, like 1,10–phenanthroline.

$$Fe(C_2O_4)_3^{3-} + h\nu \rightarrow Fe^{2+} + 2C_2O_4^{2-} + \bullet C_2O_4^{-} \qquad \textbf{2.1}$$

To achieve zero–order conditions that are independent of FeOx concentration, in which all light within the FeOx absorption band is absorbed, sufficiently high concentrations of FeOx (0.02 M) must be used. In addition, the reported quantum yield (1.25 mol einstein^{-1}) of Fe(II) formation in **Reaction 2.1** is independent of wavelength and concentration within the range of 270–365 nm.[36] Therefore, a broadband colored glass filter (UG–1, Schott Glass Tech., INC.), was used in this work to restrict the irradiance to between ~290-405 nm. **Figure 2.6** shows the transmittance spectrum of the UG–1 filter, and its effect on the absorption of the predicted solar simulator's irradiance within the FeOx absorption range (~250–500 nm).

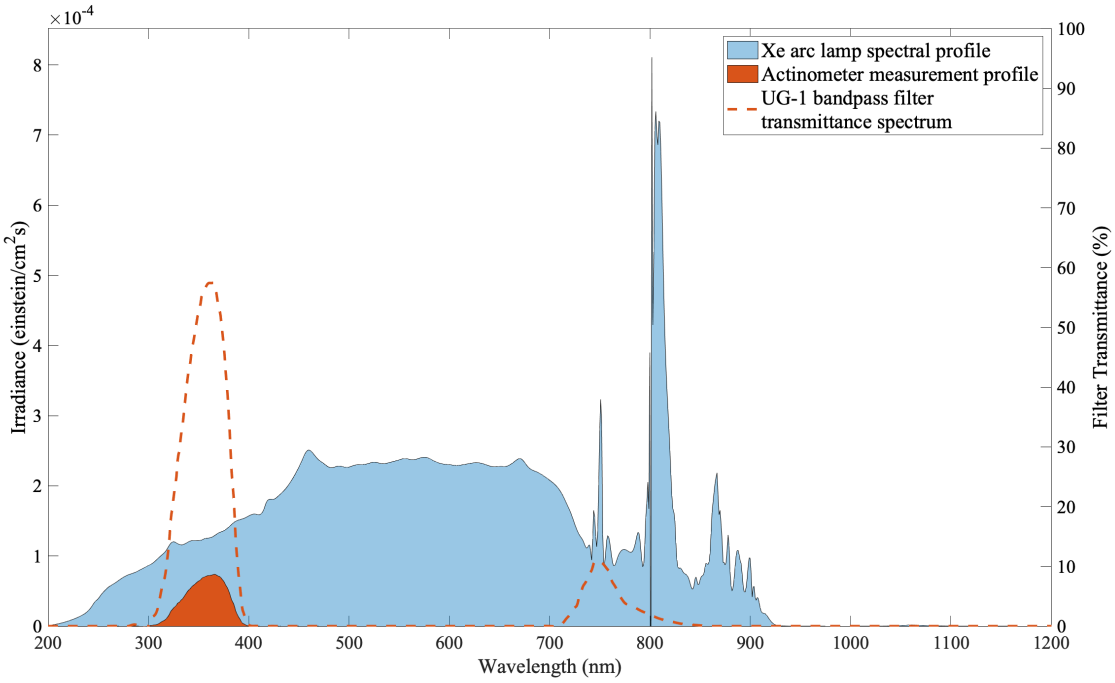

Figure 2.6: Radiant flux profile of solar simulator (blue) area in comparison to the predicted flux profile (orange area) following the UG–1 colored–glass filter (orange dashed line) used during actinometer measurements.

In this work, 3.0 mL of actinometer assay solution comprised of 0.020 M FeOx in 0.05 M H_2SO_4 were irradiated in a 3.5 mL quartz cuvette for 1 minute intervals, for a total of 10 minutes. Stock solutions of ~0.2 M FeOx in 1 M sulfuric acid was prepared by dissolving solid potassium trioxalatoferrate(III) trihydrate (Alfa Aesar) into 1.00 M sulfuric acid made from concentrated sulfuric acid (Fisher Chemical) and HPLC grade water (Fisher Chemical). Following each irradiation cycle, 10.00 µL of assay solution was transferred into 2.00 mL of colorimetric developer. The colorimetric developer solution was a 50:50 by volume mixture of 0.25 M acetate buffer and 0.2% 1,10–phenanthroline. After allowing the mixtures to develop for approximately 45 minutes in the dark, the broadband absorbance of each solution was collected by a diode array spectrophotometer (HP, 8452A) calibrated with an air blank. All reagents were prepared

fresh on each day of measurement and stored in the dark until use. Actinometric assays were compared to a control (no arc lamp irradiance) to account for iron reduction by ambient light.

The moles of Fe(II) produced during actinometric measurements was calculated from the linear regression of Fe(II) concentration (M) vs time (s) (**Figure 2.7**); in which Fe(II) concentration was determined by dividing each absorbance value at 510 nm by the Fe(II)—1,10–phenanthroline complex molar absorptivity (10610 $M^{-1}cm^{-1}$) at 512 nm. Since the FeOx actinometer functions under zero order, the slope of the linear regression of Fe(II) concentration over time will be equivalent to the reaction rate constant, k_0 (M/s). The rate constant was corrected by subtracting the rate of Fe(II) formation in the control (no arc lamp) to account for any ambient light pollution on the sample. From the corrected rate constant, the rate of Fe(II) moles produced per second can be found by accounting for the dilutions made during measurements, and then accounting for the total volume of solution used in the assay cuvette; as shown in **Equation 2.2**, where V_1 is the volume of the assay cuvette (3.00 mL), V_2 is the volume of assay solution transferred (10.00 µL) into the final volume of the colorimetric developer solution (V_3, 2.00 mL developer + 10.00 µL assay solution).

$$Fe(II)_{moles/s} = k_0 \times \frac{V_3}{V_2} \times V_1 \qquad \textbf{2.2}$$

Since the FeOx is used in high concentration, the optically concentrated nature of the FeOx make it a probe of the photo flux incident on the surface of the solution. Therefore, the measured photon flux ($E'_{p,FeOx}$, einstein/cm^{2}s) was calculated **Equation 2.3**, in which SA is the surface area of the cuvette being illuminated, and Φ is the quantum yield of the FeOx actinometer (1.25 mol/einstein).[36] The SA in this work is 3 cm^2, since the assay takes place in a cuvette that is a 1 cm x 1 cm x 4 cm rectangular

prism, filled with 3.00 mL of solution. The photon flux for this work was determined as 3.59E+15 photons/cm^{2}s.

$$E'_{p,FeOx} = \frac{Fe(II)_{moles/s}}{SA \times \Phi} \quad \textbf{2.3}$$

To determine the apparent total photon flux ($E_{p,FeOx}$) for the solar simulator used in this work, the measured photon flux ($E'_{p,FeOx}$) had to be scaled out to the full spectral profile of the simulator (shown above in **Figure 2.6**); which accounts for the use of the broadband colored–glass filter used during actinometric measurements. To do this, the trapezoidal integration method was used to obtain the integral for both the Xe arc lamp spectral profile (Z_{SS}) and the actinometer measurement profile (Z'_{SS}). **Equation 2.4** was used to determine $E_{p,FeOx}$ of the solar simulator as 1.119E+17 photons/cm^{2}s.

$$E_{p,FeOx} = Z_{SS} \times E'_{p,FeOx}/Z'_{SS} \quad \textbf{2.4}$$

Then, $E_{p,FeOx}$ was converted into a vector of photons/cm^{2}s at each wavelength ($E_{p/nm}$), by using the ratio between the total integral of the Xe arc lamp spectral profile (Z_{SS}) to that at each individual wavelength ($I_{p/nm}$) to scale the $E_{p,FeOx}$ value. $E_{p/nm}$ was used to determine the total energy of photons at each wavelength ($E_{W/nm}$) by multiplying $E_{p/nm}$ by the energy of a photon at each wavelength ($E_{photon} = hc/\lambda$). The total photon flux at the surface of the assay solution was determined to be 41.17 mW/cm^2 (411.7 W/m^2, 0.30 suns) from the trapezoidal integration of $E_{W/nm}$.

$$E_{p/nm} = E_{p,FeOx} \times I_{p/nm}/Z_{SS} \quad \textbf{2.5}$$

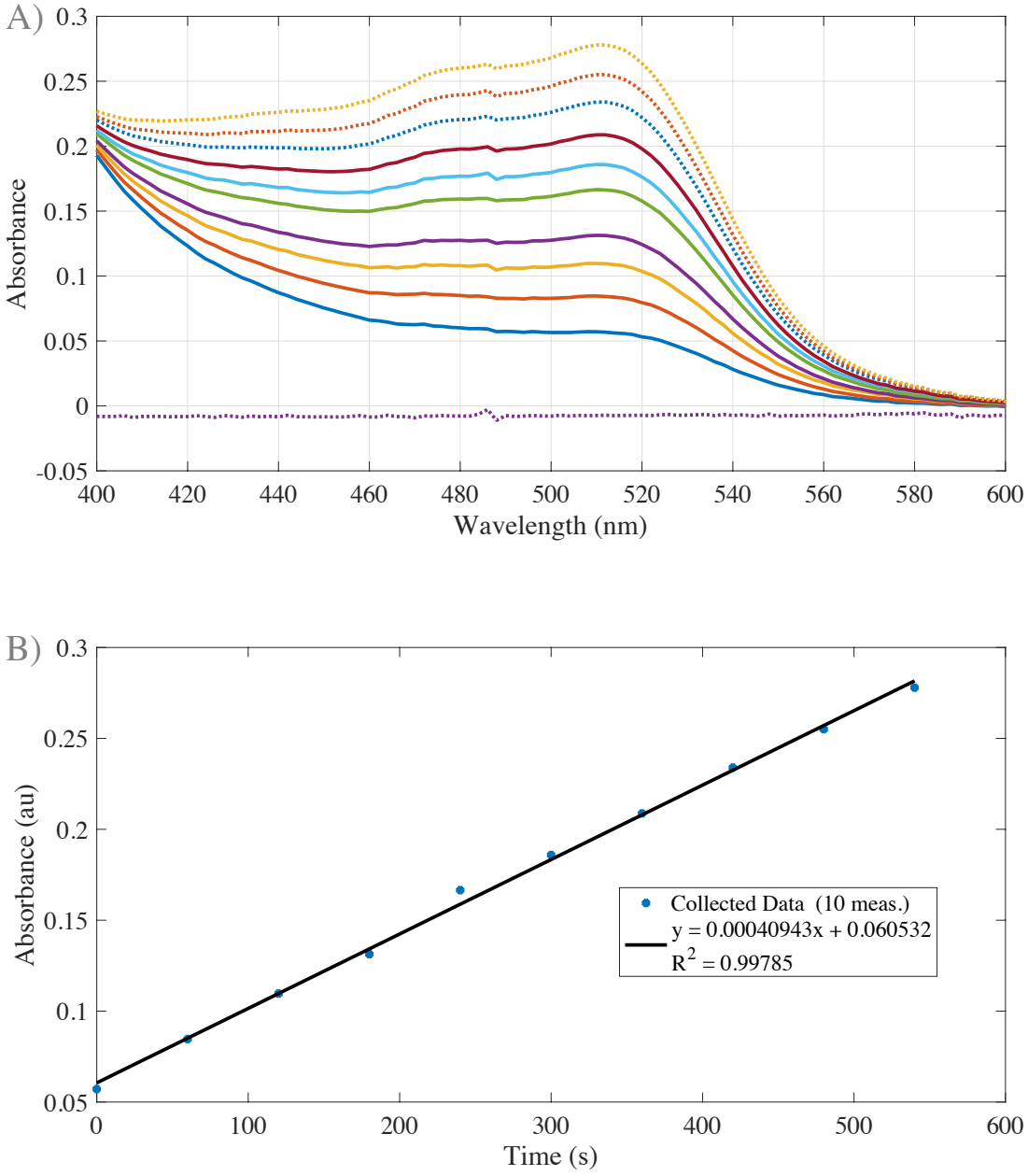

Figure 2.7: Fe(II) production during actinometer measurements. A) spectra of the Fe(II)—1,10–phenanthroline complex formation over time (1 min intervals). B) linear regression of Fe(II)—1,10–phenanthroline complex formation followed at 510 nm over 1 minute intervals.

2.5 Oxygen Photosensitization Reaction Progress Monitoring

Reaction progress was monitored using time resolved absorbance spectra obtained by the previously described diode array spectrophotometer (HP, 8452A) calibrated with an air blank. Stock solutions of model sensitizers and sensor reagents, were prepared in ethanol or the applicable assay solvent, then stored in the dark at room temperature until use. For long term storage, solutions were stored in a refrigerator at approximately 5 ºC; chilled solutions were equilibrated to room temperature before use. Assay solutions containing sensitizer and/or sensor reagents were prepared in a 5.00 mL volumetric flask, then 3.00 mL of the solution was transferred into a 3.50 mL UV quartz cuvette (FireflySci).

A 300 W xenon arc lamp (ILC Technologies, R300-3) was placed in front of samples to stimulate photo–induced reactions, as shown in **Figure 2.3**. Following the lamp, an in–house fabricated, 18 cm long, water filled glass cylinder equipped with a collimating quartz lens at the light entrance, and quartz window at the exit was used to collimate the incident light and filter out the majority of IR irradiation. The 3.50 mL UV quartz cuvette was placed on a magnetic stir plate and irradiated with 41.5 mW/cm^2 of power, as measured by the FeOX chemical actinometer (as described above). Spectra were collected every 3 to 60 seconds, depending on the rate of chromophore bleaching, for fifteen consecutive measurements by shielding the sample with a metal plate, moving the sample cuvette to the UV–Vis sample chamber for measurement, then returning the sample to the stir plate and removing the shield to continue irradiation. To avoid the accumulation and potential interference from secondary products, the chromophore bleaching was capped to no more than a 15% reduction in the initial peak absorbance. Assay trials were completed in triplicate, while control and calibration trials were completed in duplicate.

2.6 Chromophore Kinetic Analysis

In this work two approaches are used to resolve and interpret the kinetic profiles of the sensors and sensitizers during ROS assay and control measurements. The first is a more traditional approach in which the chromophore concentration is determined from the absorbance value at its wavelength of maximum absorbance (using the chromophores absorption coefficient) in baseline corrected spectra. While this method is widely applied to ROS detection, results might be misinterpreted when multiple chromophores absorb at the wavelength of concentration determinations. This can be corrected using absorption fractions relative to two, or more, known chromophores and a system of linear equations;[37] however, the interpretation is not so easily managed when unknown concomitants, like photoproducts, appear in spectra. In those cases, numerical analysis strategies like singular value decomposition paired with non–negative matrix factorization (as described below),[38] can isolate the spectral and response profile of chromophores. The isolated profiles may then be used to determine kinetic profiles with spectral overlap between chromophores—even unknown concomitants—removed; though very strong spectral overlap can undermine the recovery of accurate kinetic profiles.

2.6.1 Traditional Single–Wavelength Kinetic Analysis

The time-resolved, UV–Vis diode array absorbance data were subjected to traditional kinetic analysis, at single wavelengths, to gain insight into the efficiency and efficacy of various reactive oxygen species (ROS) sensor mechanisms. To begin, a concentration profile over time was obtained for all known chemical reagents in each data set. This was achieved by using previously obtained molar absorptivity data, to convert each chromophores absorbance profile at its lambda max into a concentration

profile. Then plots of concentration, natural log of concentration, and inverse concentration all vs. time were constructed to obtain zero, first, and second order rate law equations, respectively. From these plots, reagents in each reaction condition were profiled as following zero, first, or second order, based on the best suited linear rate law fit. In this work, most reaction reagents, in most reaction conditions, followed zero order rate laws.

2.6.2 Numerical Analysis Strategies

As was described in previous work,[38] the data sets collected within this work consist of a series of absorbance spectra monitored with respect to time or concentration. Series of spectra collected in each solvent as sensor assays, controls and calibrations were arranged into a concatenated matrix format; each forming a single matrix that captures the range of responses throughout the various measurement types. **Figure 2.8** depicts an example data matrix constructed by concatenating spectra collected in phosphate buffer for the Imd plus RNO method (RBRNOPB, described later in **Chapter 4**). Each concatenated data matrix, **A**, has dimensions equal to ***I*** columns by ***J*** rows, where ***I*** is the number of pixels (wavelengths) in each spectrum and ***J*** is the total number of measurements (acquisition times or concentrations) in each reaction or calibration progress profile.

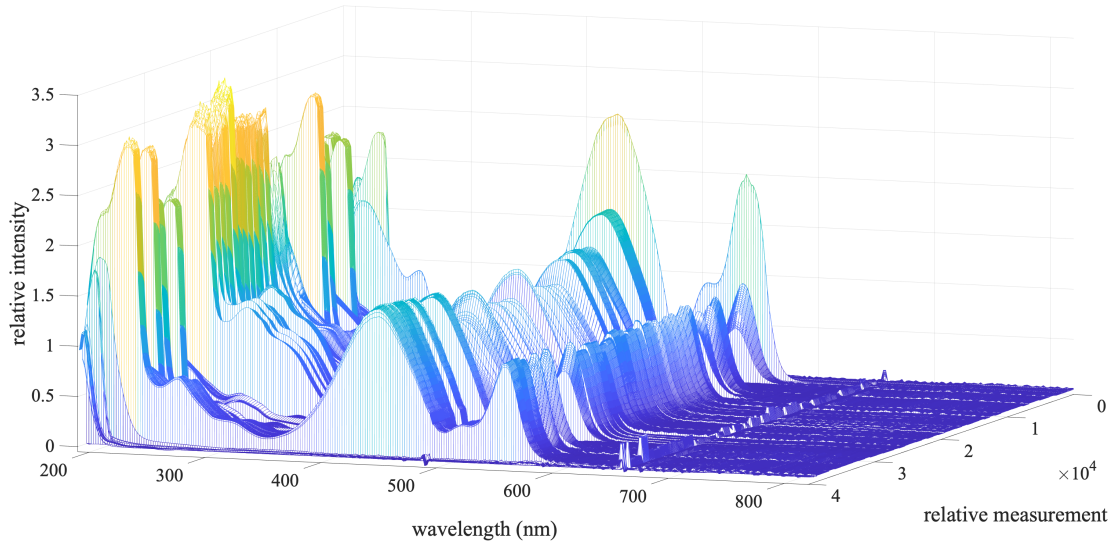

Figure 2.8: Matrix-formatted Rose Bengal in phosphate buffer data sets constructed by concatenating absorbance spectra collected during sensor assays, controls and calibrations.

As is shown in **Equation 2.6**, this matrix is described by Beer's Law and can be partitioned into matrices comprised of relative component absorptivities and concentrations as will be described below. The matrix also can be analyzed to determine the number of distinct species that contribute to the spectral and kinetic changes observed during the course of a process, reaction or sequence of measurements. The singular value decomposition (SVD)[19] partitions $\boldsymbol{A}$ into orthonormal row and column factor matrices, i.e., basis sets:

$$\boldsymbol{A} = \boldsymbol{U}\boldsymbol{\Sigma}\boldsymbol{V}^T \qquad \textbf{2.6}$$

where $\boldsymbol{U}$ is a matrix of column singular vectors, $\boldsymbol{V}$ is a matrix of row singular vectors, and $\boldsymbol{\Sigma}$ is a diagonal matrix whose elements, σ_{kk}, are the square roots of the variance product of the kth columns of $\boldsymbol{U}$ and $\boldsymbol{V}$, $u_k v_k^T$, that contribute to $\boldsymbol{A}$. $\boldsymbol{U}$ and $\boldsymbol{V}$ have the same number of columns as the smaller dimension of $\boldsymbol{A}$, $\boldsymbol{R} = min(\boldsymbol{I}, \boldsymbol{J})$. The SVD summarizes the variance of $\boldsymbol{A}$ in the smallest possible number of orthogonal factors for

the columns and rows. Consequently, in most cases, fewer than $\boldsymbol{R}$ singular vectors are required to estimate the matrix values within experimental error.

When the number of spectral components, N, which is called the pseudo–rank, is not known prior to the analysis, it can be estimated using statistical and signal processing methods.[39–42] **Figure 2.9** illustrates methods used in this work applied to the concatenated RBRNOPB data sets. Subplot D illustrates the first ten column singular vectors of the data sets. Subplot A depicts the matrix singular values (square root of each eigenvalue) and the reduced eigenvalues, scaled.[43] Subplot B shows the F-tests carried out using the reduced eigenvalues.[39] Subplot C shows plots of column (spectral) singular vector autocorrelations and column (spectral) singular vector high-frequency content.[40,42]

When data quality is high, the rank can be determined by inspection of singular value and eigenvalue plots because of the large difference in the scale of spectral and noise components. As the number of components increases and the signal-to-noise ratio drops, and more rigorous methods are needed. The noise content of spectral singular vectors is reflected in the proximity of their autocorrelation coefficients to zero and proximity of the fraction of Fourier components at frequencies above 20% of the Nyquist frequency to unity. The results depicted in **Figure 2.9** were used to set the pseudo–rank estimate of the RBRNOPB set to ten components. The remaining $R{:}N$ columns of $\boldsymbol{U}$ and $\boldsymbol{V}$ describe noise and were removed from $\boldsymbol{U}$ and $\boldsymbol{V}$ prior to additional analysis. The bar symbol, i.e., $\bar{U}$, $\bar{\Sigma}$, and $\bar{V}$ is used to specify the truncated (N-component) versions of the SVD factors. **Figure 2.10** shows the reconstructed RBRNOPB data sets, as well as the residuals when the concatenated matrix was reconstructed using the truncated SVD factors.

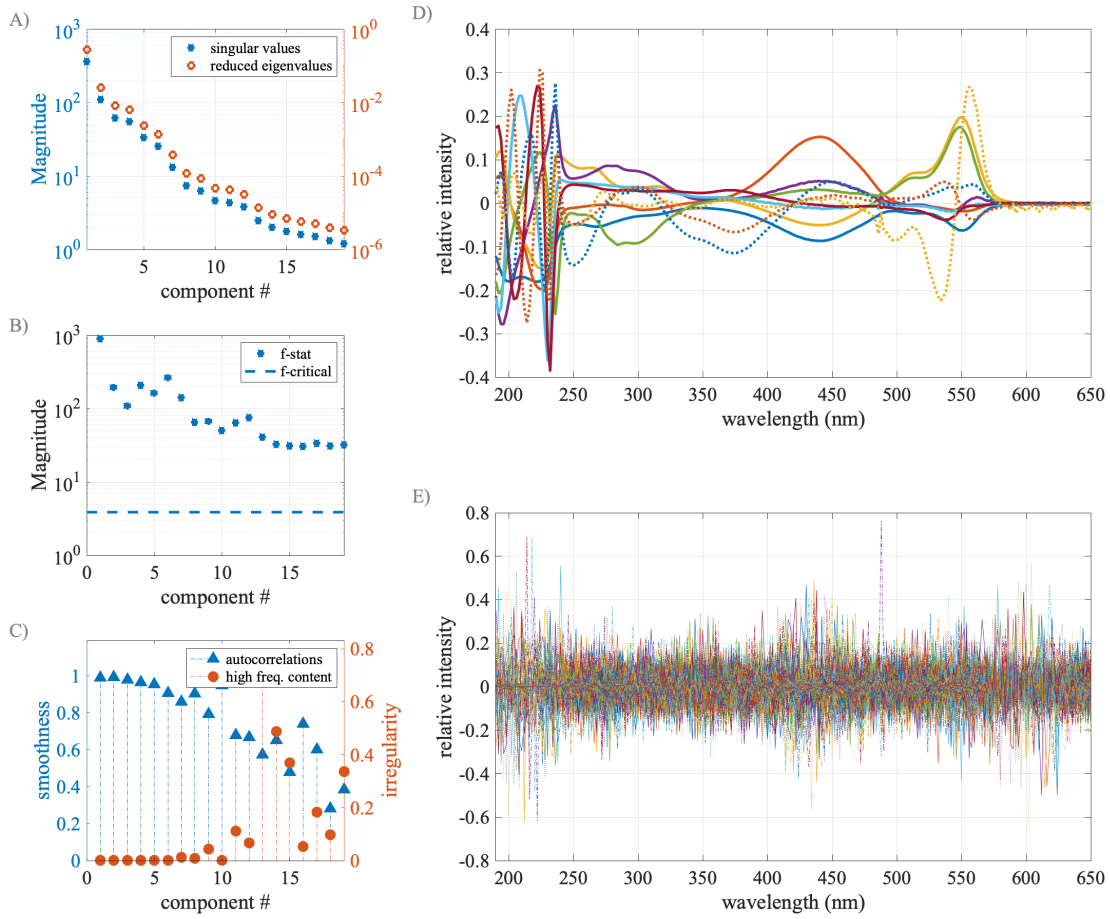

Figure 2.9: Pseudorank estimation of concatenated RBRNOPB data sets. A) Log of singular values and reduced eigenvalues. B) F–test of reduced eigenvalues and critical frequency. C) Column (spectral) singular vector autocorrelations (blue Δ's) and high–frequency content (orange O's) for the first nineteen components. D) The first ten column (wavelength) singular vectors; determined as significant. E) The remaining column singular vectors (R:N); determined as insignificant.

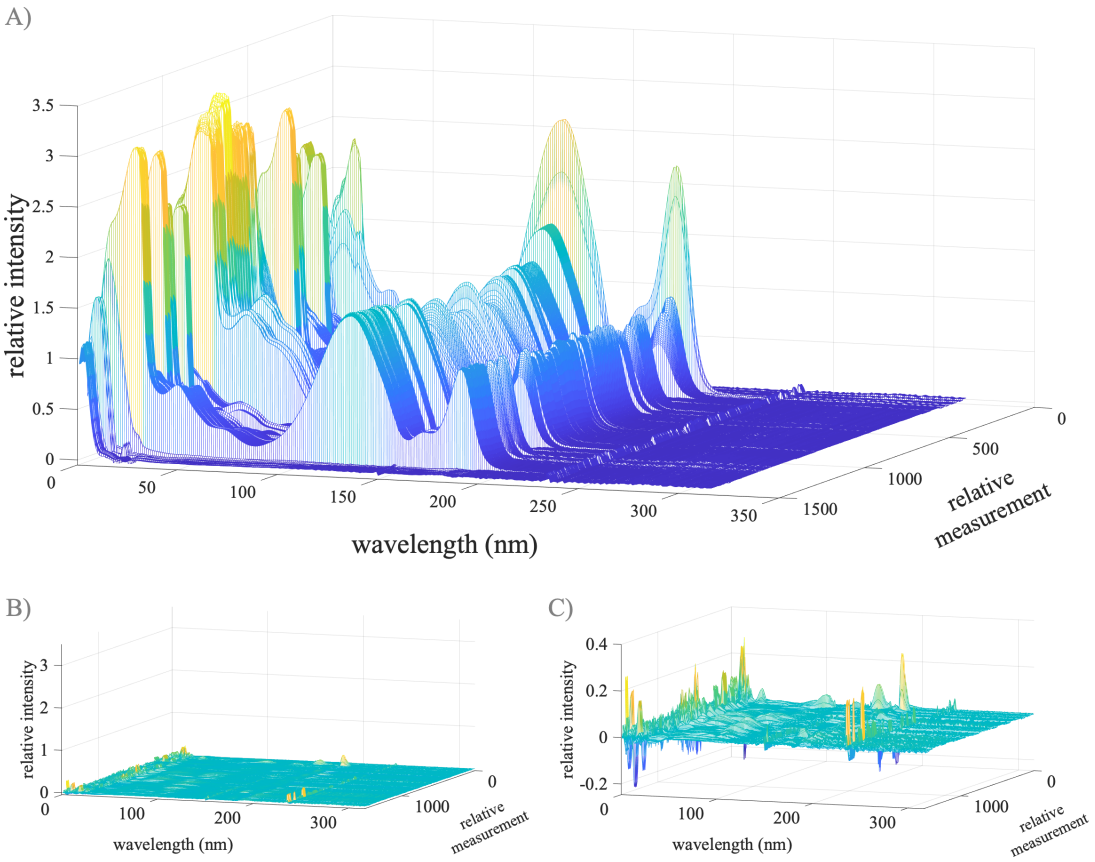

Figure 2.10: A) Mesh plot of RBRNOPB data sets reconstructed using the first ten SVD components. B) Mesh plot of the SVD reconstruction residuals set to the same scale as the measurements. C) Mesh plot of the SVD reconstruction residuals set to the scale of residuals.

Since the columns of $\boldsymbol{U}$ are linear combinations of the columns of $\boldsymbol{A}$, they are also combinations of the sample component spectra. Consequently, after pseudo-rank analysis, absorbance matrices can be factored into matrices comprised of the (normalized) sample component spectra and their corresponding concentration profiles, respectively, using various curve resolution algorithms.[44–47] Often, these algorithms involve transforming the orthonormal factors, $\boldsymbol{U}$ and $\boldsymbol{V\Sigma}$, to estimates of the spectra and concentrations, $\widehat{\boldsymbol{E}}$ and $\widehat{\boldsymbol{C}}$, respectively, using optimization routines to find the values of

the transformation matrices that implement the conversion, while avoiding physically untenable properties in the new factors, such as negative intensities and concentrations. Positive matrix factorization,[48] alternating least squares[45,49] and non-negative matrix factorization[20] are the most widely cited approaches. In the work reported here, non-negative matrix factorization (NMF) of Lee & Seung,[20] as described by Mirzal,[50] was used. This algorithm uses a multiplicative update of the estimates of the non-negative factors, $\widehat{\boldsymbol{E}}$ and $\widehat{\boldsymbol{C}}$, that minimize the loss function, i.e., the difference between the data matrix, $\boldsymbol{A}$, and factor product, $\widehat{\boldsymbol{E}}\widehat{\boldsymbol{C}}^T$:

$$\min_{\widehat{\boldsymbol{E}}\geq 0,\widehat{\boldsymbol{C}}\geq 0} L\left(\widehat{\boldsymbol{E}},\widehat{\boldsymbol{C}}\right) = \frac{1}{2} tr\left(\left(\boldsymbol{A}-\widehat{\boldsymbol{E}}\widehat{\boldsymbol{C}}^T\right)^T\left(\boldsymbol{A}-\widehat{\boldsymbol{E}}\widehat{\boldsymbol{C}}^T\right)\right) \qquad \textbf{2.7}$$

where L is the square root of the sum of the squares of the residuals when the product $\widehat{\boldsymbol{E}}\widehat{\boldsymbol{C}}^T$ is subtracted from the data matrix, $\boldsymbol{A}$. Factors that satisfy this minimization can be determined by refining arbitrary initial guesses using update factors constructed from the derivatives of L with respect to the factor being updated until they are transformed to matrices that bring the derivatives of the loss function to a minimum. Once satisfactory factors are determined, the resulting spectra, $\widehat{\boldsymbol{E}}$, and concentration, $\widehat{\boldsymbol{C}}$, profiles are constructed and subjected to kinetic analysis to obtain zero, first, and second order rate law equations, in a similar manner to the traditional kinetic analysis described above.

Chapter 3

EVALUATING COMMERCIALLY AVAILABLE SINGLET OXYGEN & SUPEROXIDE SENSORS USED UNDER ENVIRONMENTALLY & BIOLOGICALLY RELEVANT CONDITIONS

3.1 Abstract

The stability of several commercially available singlet oxygen and superoxide sensors were evaluated for their use in environmentally or biologically relevant samples. Sensor stability was evaluated using two types of assay control measurements: broadband molar absorptivity, and photostability under broadband simulated sunlight. From the molar absorptivity measurements, the sensor's stability in each solvent was observed. Through the photostability measurements, the feasibility of using the sensor in photooxidation studies was evaluated.

Three singlet oxygen sensors—1,3-diphenylisobenzofuran (DPBF), 9,10-anthracenedipropionic acid (ADPA), and p-nitrosodimethylaniline (RNO) plus imidazole (Imd)—as well as three superoxide sensors—7-chloro-4-nitrobenzo-2-oxa-1,3-diazole (NBD-Cl), 1,4-benzoquinone (BQ), and 3-(4,5-dimethyl-2-thiazol)-2,5-di-phenyl-2H-tetrazolium bromide (MTT)—were assessed. Out of the six sensors, only two were determined acceptable for use in the proposed environmentally and biologically relevant conditions, the Imd plus RNO method for $^1O_2$ detection, and the MTT sensor for $O_2^{\bullet-}$ detection. For the remaining sensors, DPBF, NBD-Cl, and BQ, instability during the controls were observed, including sensor degradation during molar absorptivity and photodegradation control measurements. The evaluation of ADPA was

incomplete, and its photostability remains a question. Due to the observed instability, caution and attention to control measurements are suggested when using these, and possibly other, commercially available ROS sensors in the environmentally and biologically relevant conditions of this, and similar, work. Much of the contents of this chapter have been published previously.[18]

3.2 Introduction

Monitoring reactive oxygen species (ROS), like singlet oxygen ($^1O_2$) and superoxide ($O_2^{\bullet-}$), is both challenging and important to investigations and applications in many fields. ROS are energetic, transient species that are produced by several chemical reactions, biological processes, and/or photoinduced processes. In natural systems, ROS are capable of oxidizing a wide variety of molecules with relatively low selectivity, and can lead to contaminants and the transformation of dissolved organic matter in aquatic environments.[51] ROS can, at high levels, cause irreversible damage to lipids, proteins, and DNA, which may lead to oxidative stress and inevitably, cell death.[52] At the same time, ROS are needed for many natural biological processes, like during molecular signaling in plants and in the maintenance of physiological functions.[17] These risks and benefits create a need for delicate balance between too few and too much ROS in many systems; leading to the importance of ROS investigations, and development of reliable ROS sensing.

Due to their transient nature, $^1O_2$ and $O_2^{\bullet-}$ are typically monitored spectrophotometrically through the use of indirect colorimetric molecular sensors. While there are direct measurement methods that record the properties of analyte transitions, indirect measurements that use the transition of sensors (i.e. analyte–responsive reagents or products of analyte–selective reactions) are often much cheaper

and available commercially. Near the start of this work, Burns et al. compiled a review summarizing direct and indirect analytical methods for the detection and quantification of common ROS. Among the $^1O_2$ absorption-based sensors, 1,3-diphenylisobenzofuran (DPBF), 9,10-Diphenylanthracene (DPA), p-nitrosodimethylaniline (RNO), 9,10-anthracenedipropionic acid (ADPA), and furfuryl alcohol (FFA) are the most widely cited.[51] Likewise, cytochrome *c*:Fe(III) (FC), Nitro Blue Tetrazolium (NBT), 7-chloro-4-nitrobenzo-2-oxa-1,3-diazole (NBD-Cl), 3-(4,5-dimethyl-2-thiazol)-2,5-di-phenyl-2H-tetrazolium bromide (MTT), 2,3-bis(2-Methoxy-4-nitro-5-sulphophenyl)-5-[(phenylamino)carbonyl]-2*H*-tetrazolium hydroxide (XTT), 1,4-benzoquinone (BQ), are some of the most cited absorption-based $O_2^{\bullet-}$ sensors.[51] The work outlined in this chapter will focus on examining the stability of a subset of the widely cited $^1O_2$ and $O_2^{\bullet-}$ spectrophotometric sensors for use in biorelevant solvents and under broadband simulated sunlight. While these sensors have been used broadly in aqueous and non–aqueous environments, there are few reports of their use in the conditions proposed in this work; specifically, broadband irradiation, since many studies choose to test photosensitization reactions using lasers.

One of the more widely cited $^1O_2$ sensors for use in photooxidation studies in organic solvent, DPBF is reported to react quickly (1.1×10^9 $M^{-1}s^{-1}$, in EtOH)[53] $^1O_2$ in a 1:1 stoichiometry (see **Scheme 3.1**) without any significant side reactions.[54] The sensor functions by decomposing upon reaction with $^1O_2$, leading to a decrease in its absorption peak around 415 nm. Reports have suggested that while DPBF has a low reduction potential and reacts with other oxidants, it is still selective to $^1O_2$ and does not react with other common ROS.[54] While DPBF is among the most cited $^1O_2$ sensors, it is not free from error. DPBF is highly sensitive to photobleaching, and is particularly

susceptible to self-photooxidation through absorption in the ultra violet (UV) region.[55] Therefore, the reagent should be prepared in the dark, shortly before each use, and stored in dark conditions. In addition, adverse chain reactions have an increased influence on the decomposition rate at high DPBF concentrations, which can occur even at low concentrations in microheterogeneous systems, due to the increased local concentration.[54] To that end, DPBF should be used in low (<150 μM) concentrations.

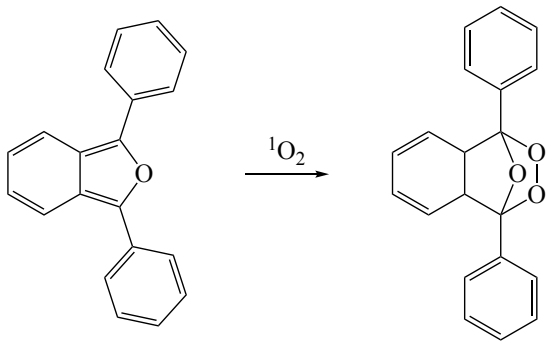

Scheme 3.1: Structure of 1,3-diphenylisobenzofuran (DPBF), followed by the $^1O_2$–DPBF product upon reaction between DPBF and $^1O_2$.

Another commonly used $^1O_2$ sensor is the water–soluble, anthracene derivative, ADPA. ADPA and $^1O_2$ react via a [4+2] Diels-Alder cycloaddition with a reported rate constant of 8 x 10^7 $M^{-1}s^{-1}$ (in heavy water)[56] to form a colorless endoperoxide product, effectively reducing the ADPA as shown in **Scheme 3.2**. As with many of the sensors discussed in this work, the progress of the reaction can be monitored by following the first order reduction in absorbance at ADPAs absorption maximum around 380 nm, or its emission peak around 430 nm.[57] There have been recent reports of ADPA being used in photooxidation studies,[58–60] though as is typical, those studies irradiated their sensitizer(s) with laser or narrowband excitation sources. ADPA has also been used in

a variety of applications ranging from simple aqueous mixtures, to nanoparticle suspensions.[56,61]

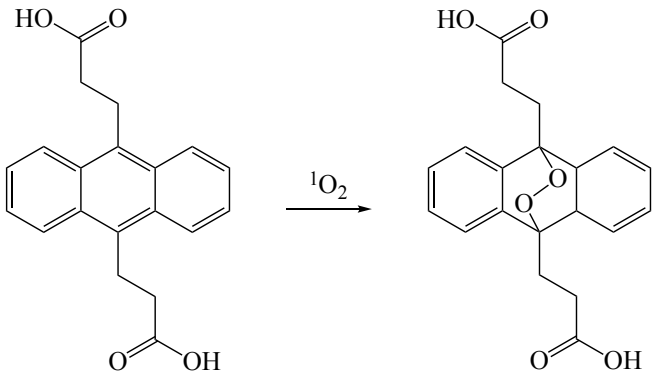

Scheme 3.2: Structure of 9,10-anthracenedipropionic acid (ADPA), followed by the $^1O_2$–ADPA product upon reaction between ADPA and $^1O_2$.

The imidazole plus RNO (Imd/RNO) method, originated by Kraljić and El Mohsni, was developed to monitor $^1O_2$ in aqueous solution.[62] In this method, $^1O_2$ is quenched by the acceptor, imidazole (Imd), at a rate of 2 x 10^7 $M^{-1}s^{-1}$,[63] the formation of a trans-annular peroxide intermediate that goes on to bleach the sensor, RNO. In the mechanism offered by Kraljić and El Mohsni, shown in **Scheme 3.3**, Imd is released as the peroxide bleaches the sensor. The rate of $^1O_2$ production is indirectly quantified by following the degradation of the sensor around 440 nm. The method has been used in the subsequent 40 years to monitor $^1O_2$ production by a large variety of homo– and heterogenous media, including antioxidants,[64] nanocarriers,[65,66] phototoxic compounds,[67] coumarins,[63,68] anthraquinones,[69] porphyrins,[70] human lens proteins,[71] and iron-sulfur proteins.[72] The published uses of Imd/RNO method have included the use of broadband irradiation, making it appear as a well–suited candidate for the conditions of this work.

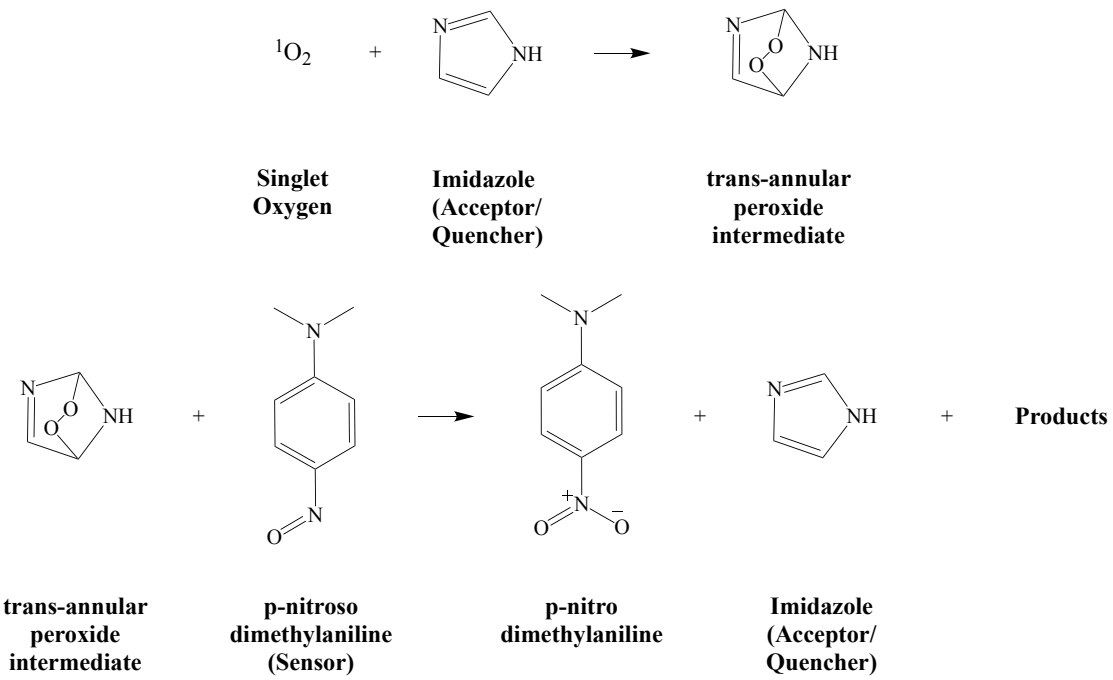

Scheme 3.3: Singlet oxygen capture and subsequent bleaching of RNO by the Imd–$^1O_2$ trans-annular peroxide intermediate as described by Kraljić and El Mohsni (1978)

NBD-Cl (shown in **Scheme 3.4**) has been used as both a fluorescent and spectrophotometric sensor for the determination of $O_2^{\bullet-}$ in aqueous solutions. The sensor has absorption maximum at 343 nm, and upon reaction with $O_2^{\bullet-}$, a new absorption peak forms at 470 nm with an emission wavelength of 550 nm.[73–75] Though NBD-Cl was originally synthesized for detection of amino acids, amines, and thiols,[74] it has been reported to have a quicker superoxide response (1.5 x 10^5 $M^{-1}s^{-1}$, in DMSO)[73] the more popular XTT sensor (8.59 x 10^4 $M^{-1}s^{-1}$, in pH 7.8 0.05 M PB).[76] While NBD-Cl is reported to react with nucleophiles to form reversible Meisenheimer adducts,[74] to my knowledge, current literature has not offered a definitive reaction scheme between NBD-Cl and superoxide. Research has shown NBD-Cl to have a limit of detection in the nM–μM range, that is unaffected by common biological concomitants (H_2O_2, NADH, NADPH, & NAD^+).[51] While NBD-Cl has been shown to reliably and rapidly

detect and quantify superoxide in aqueous solution,[73] there have not yet been reports on its photostability, especially under broadband simulated sunlight.

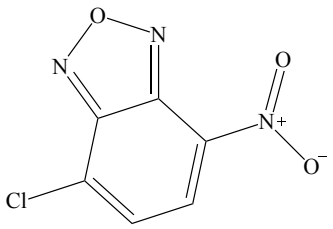

Scheme 3.4: Structure of 7-chloro-4- nitrobenzo-2-oxa-1,3-diazole (NBD-Cl).

A less popular $O_2^{\bullet-}$ sensor, 1,4-benzoquinone (BQ), as shown in **Scheme 3.5**, reacts with $O_2^{\bullet-}$ in an electron transfer process to give the semiquinone radical anion ($BQ^{\bullet-}$) with a reported bimolecular rate constant around 9.8 x 10^8 $M^{-1}s^{-1}$ (in water).[77,78] It is then the absorbance of the semiquinone product near 430 nm that is used as a means of counting $O_2^{\bullet-}$ ions. BQ has been used in many applications for both the quantitive detection[79,80] and qualitative scavenging of $O_2^{\bullet-}$,[81–85] with a large subset of citations focused on laser flash photolysis measurements and determinations of novel molecular photocatalytic activity for *in vitro* use. However, quinones have been identified as effective photosensitizers in photodynamic therapy applications;[86] in which case, BQ acting as a $O_2^{\bullet-}$ sensor may be compromised if its own contribution to the ROS measurement cannot be determined and accounted for.

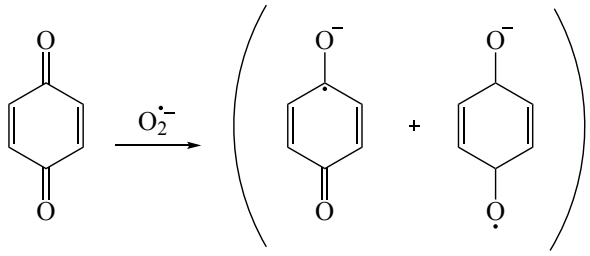

Scheme 3.5: Structure of 1,4-benzoquinone (BQ), followed by the $O_2^{\bullet-}$–BQ product upon reaction between BQ and $O_2^{\bullet-}$.

MTT is a tetrazolium compound that can be reduced to its colored formazan upon reaction with $O_2^{\bullet-}$, in the two-step process illustrated in **Scheme 3.6**. First, a tetrazolinyl radical intermediate is formed via a one-electron transfer from $O_2^{\bullet-}$; the intermediate then disproportionates to the MTT tetrazolium salt and monoformazan.[87] The $O_2^{\bullet-}$ formation can be quantified by monitoring the appearance of the monoformazan around 570 nm over reaction time. Unlike similar tetrazolium compounds (XTT and MTS), MTT and its formazan reduction products are not freely soluble in neat aqueous solvents, which may present issues for this work at high MTT concentrations. MTT has been used for detection of intracellularly generated $O_2^{\bullet-}$,[52] cytotoxicity potential of drugs in liposomes,[88] and, most commonly, to estimate cell viability and proliferation for many systems.[87,89,90]

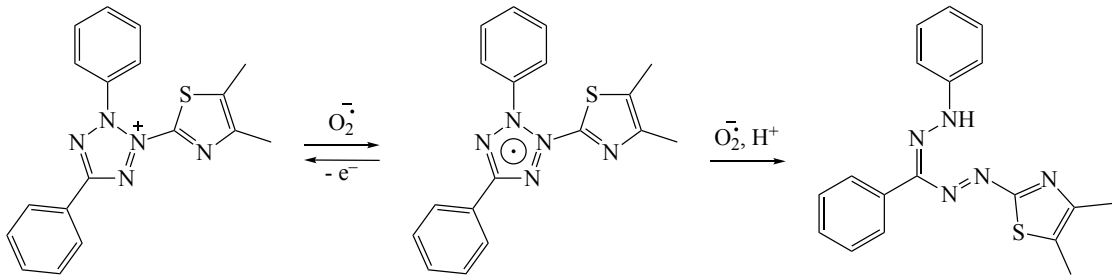

Scheme 3.6: Structure of 3-(4,5-dimethyl-2-thiazol)-2,5-di-phenyl-2H-tetrazolium bromide (MTT), followed by the intermediate tetrazolinyl radical, and then the MTT formazan product resulting from the reaction between MTT and two successive $O_2^{\bullet-}$ radicals.

The aim of the research reported here is to examine the stability of the six aforementioned $^1O_2$ and $O_2^{\bullet-}$ sensors using two types of assay control measurements. In the first control, the broadband absorbance of the sensor during molar absorptivity measurements will be monitored in a variety of isotropic and microheterogeneous solvents. A sensor's broadband molar absorptivity spectrum can bring insight into how stable the sensor is in each solvent by monitoring the linearity of the sensor's absorption profile over a broad concentration range. A stable molar absorptivity is also crucial in determining sensor concentration from absorbance profiles; an important step in interpreting assay results. In addition, monitoring the molar absorption coefficient of the sensor across solvents of varying dielectric constants and structure type (isotropic vs. microheterogeneous) may later inform the sensors behavior during ROS assay measurements, i.e. whether a sensor "favors" one particular portion of a micellar solution or is solvated in the interfacial region of the micelle.[24]

These sensors are intended to be used in later work for ROS assay measurements, in which the assay solution is irradiated with broadband simulated sunlight, to mimic environmental conditions. Therefore, in the second control

measurement, the rates of sensor bleaching induced by simulated sunlight in each of the proposed solvents will be monitored. Drastic sensor bleaching during the control, and later in assay measurements could lead to a buildup of concomitants, effecting the efficiency of the sensor for ROS detection. Therefore, the sensor will ideally exhibit minimal bleaching during the control and in the absences of ROS producing concomitants—less than 5% during the typical assay measurement range of 15 minutes (~0.055 $\%/s$).

The performance of each sensor was evaluated in aqueous and isotropic solvents commonly used in ROS sensing, like pH 7.4 phosphate buffer (PB), pH 10.0 borate buffer (BB), and ethanol (EtOH), as well as in more complex microheterogeneous solvents with biomimetic and geomimetic properties, like 5% sodium dodecyl sulfate (SDS), neat octanol (OctOH), and pH 7.4 phosphate buffer saturated octanol (PBOctOH). Octanol-water partition coefficients are commonly used to predict the pharmacokinetic characteristics of drug compounds and the toxicity and transport of pollutants in soil and groundwater systems.[27] Octanol was also selected for its structural microheterogeneity,[27,28] i.e. its capacity to self-assemble into predominantly hydrophilic and hydrophobic regions, like the aqueous micellar solution, sodium dodecyl sulfate. The impact of this feature on the method was investigated using phosphate buffer saturated octanol (PBOctOH), which is approximately 26% aqueous buffer.[28]

3.3 Methods

3.3.1 Materials

1,3-diphenylisobenzofuran (DPBF, Acros Organics), 9,10-anthracenedipropionic acid (ADPA, chemodex), p-nitrosodimethylaniline (RNO, Acros

Organics), imidazole (Imd, Fisher Scientific), 7-chloro-4- nitrobenzo-2-oxa-1,3-diazole (NBD-Cl, Alfa Aesar), 1,4-benzoquinone (BQ, Sigma Aldrich), 3-(4,5-dimethyl-2-thiazol)-2,5-di-phenyl-2H-tetrazolium bromide (MTT, Acros Orgaincs), acetonitrile (Acn, Fisher Chemical), dimethyl sulfoxide (DMSO, Fisher Chemical), HPLC grade water (HOH, Fisher Chemical), pH 10.0 borate buffer (BB, Alfa Aesar), octanol (OctOH, 99% pure, Acros Organics), and ethanol (EtOH, Decon Laboratories, Inc.) were purchased and used as received. Phosphate buffer (PB) was prepared by combining 1.0 M sodium phosphate dibasic (Na_2HPO_4, Fisher Chemical) and 1.0 M sodium phosphate monobasic (NaH_2PO_4, Fisher Scientific) in a 7.74:2.26 volume ratio, then diluted to 1.0 L with HOH; resulting in a buffer salt concentration of 0.01 M, and pH of approximately 7.4 (as measured by glass electrode). Sodium dodecyl sulfate 5% micellar solution (SDS) was prepared by dissolving 25 grams of sodium lauryl sulfate (Fisher Scientific) into 500 mL. Phosphate buffer saturated octanol was prepared by combining an equal volume ratio of pH 7.4 PB and OctOH, stirring on an electronic stir box for approximately 4 hours, and then allowing the mixture to rest for at least 72 hours before removing the organic layer for use.

Stocks of each sensor were initially prepared by solvation in EtOH to obtain stock solutions that were later diluted using one of the desired solvents. All stock solutions were wrapped in tin foil (to avoid ambient light exposure), refrigerated, and monitored by UV–Vis absorption spectroscopy for signs of decay or contamination; stocks were discarded if the chromophores peak absorption band decreased by more than 5%.

3.3.2 Molar Absorptivity

Molar absorptivities (ε) were obtained using solutions of increasing concentrations, in a single cuvette. Starting with 1.8–2.0 mL of solvent in a 3.5 mL quartz cuvette, µL additions of stock solution were added to the cuvette, and spectra collected by a diode array spectrophotometer (HP, 8452A). Depending on the sensor, molar absorptivities were conducted in a subset of the following solvents: phosphate buffered water (PB) of pH 7.4 or 11.8, borate buffered water (BB) of pH 10.0, 5% sodium dodecyl sulfate micellar solution (SDS), ethanol (EtOH), dimethyl sulfoxide (DMSO), acetonitrile (Acn), octanol (OctOH), and pH 7.4 PB saturated OctOH (PBOctOH). Molar absorptivities were, at minimum, completed in duplicates, with at least one trial in which the spectrometer was calibrated with an air blank (empty cuvette), and one with a solvent blank (cuvette filled with solvent). Absorption spectra were collected by a diode array spectrophotometer (HP, 8452A), then used to construct a Beer's Law plot of absorbance versus concentration. The molar absorptivity was computed from the slope of the linear line of best fit at the sensor's wavelength of maximum absorbance.

3.3.3 Sensor Photodegradation

The photodegradation of each sensor was monitored over time. Solutions of 5.0 mL were prepared containing an appropriate sensor concentration (50–200 µM—based on recommended assay concentrations from recent publications). Depending on the sensor, photodegradation was measured in a subset of the following solvents: phosphate buffered water (PB) of pH 7.4 or 11.8, borate buffered water (BB) of pH 10.0, 5% sodium dodecyl sulfate micellar solution (SDS), ethanol (EtOH), dimethyl sulfoxide (DMSO), acetonitrile (Acn), octanol (OctOH), and pH 7.4 PB saturated

OctOH (PBOctOH). A 300 W xenon arc lamp (ILC Technologies, R300-3) was placed in front of samples, as shown in Figure **2.3**. Between the lamp and sample, an 18 cm temperature–controlled water column fitted with quartz lenses was used to collimate the incident light and filter out the majority of the IR irradiation. For each photodegradation trial, 3.0 mL of the prepared solution was placed into a 10 mm pathlength quartz cuvette (FireflySci), placed on a magnetic stir plate, and irradiated in 3 second to 5 minute consecutive time intervals. At the end of each time interval, the sample was manually shielded with a metal plate, moved to the UV–Vis sample chamber for measurement, then returned to the stir box where the metal shield was removed for further irradiation. All spectra were collected by a diode array spectrophotometer (HP, 8452A) calibrated with an air blank (empty cuvette). Trials were, at minimum, completed in duplicates. Degradation profiles were calculated by converting the sensor's absorbance at the wavelength of maximum absorbance to a concentration at each time interval. Degradation percentage rates were determined by normalizing the sensor concentration at each interval to the first (i.e. point #1 was set as 0% degradation), then plotting the degradation percent over time; the slope of this plot was reported as the degradation percent rate, in %/s.

3.4 Results & Discussion

The stability of multiple singlet oxygen ($^1O_2$) and superoxide ($O_2^{\bullet-}$) colorimetric sensors in select isotropic and microheterogeneous solvents was examined. For each sensor, the ideal result would include a stable, linear relationship between the chromophores absorbance over a broad range of concentrations in each solvent, as well as minimal sensor degradation over irradiation time, with no more than 5% degradation at the wavelength of maximum absorbance over the typical assay time (15 minutes).

The results of all sensor molar absorptivity and photostability have been summarized in **Tables 3.1** and **3.2**, respectively. These results are necessary for the sensor to be utilized in subsequent reactive oxygen species (ROS) detection methods in which the sensor absorbance will be monitored over time while the sensors and a photosensitizer are irradiated with broadband, simulated sunlight.

Table 3.1: Absorbance properties, wavelength of maximum absorbance and molar extinction coefficient (ε), of ROS sensors observed in selected solvents.

	DPBF	**ADPA**	**RNO**	**NBD-Cl**	**BQ**	**MTT**
PB ($\varepsilon_r \approx 80$) ‡	-	400 nm, 9040 $M^{-1}cm^{-1}$	440 nm, 20800 $M^{-1}cm^{-1}$	-	248 nm, 14000 $M^{-1}cm^{-1}$	380 nm, 6680 $M^{-1}cm^{-1}$
BB ($\varepsilon_r \approx 80$) ‡	-	-	-	334 nm, 10400 $M^{-1}cm^{-1}$	-	-
DMSO ($\varepsilon_r = 47$)	418 nm, 26000 $M^{-1}cm^{-1}$	-	-		-	-
Acn ($\varepsilon_r = 38$)	412 nm, 16800 $M^{-1}cm^{-1}$	-	-		-	-
SDS ($\varepsilon_r \approx 32$) †	-	400 nm, 9120 $M^{-1}cm^{-1}$	440 nm, 23400 $M^{-1}cm^{-1}$	-	-	388 nm, 6410 $M^{-1}cm^{-1}$
EtOH ($\varepsilon_r = 25$)	412 nm, 15000 $M^{-1}cm^{-1}$	398 nm, 10450 $M^{-1}cm^{-1}$	422 nm, 24900 $M^{-1}cm^{-1}$	338 nm, 8770 $M^{-1}cm^{-1}$	-	378 nm, 8080 $M^{-1}cm^{-1}$
PBOctOH	-	-	422 nm, 12100 $M^{-1}cm^{-1}$	-	-	380 nm, 7130 $M^{-1}cm^{-1}$
OctOH ($\varepsilon_r = 10$)	416 nm, 32700 $M^{-1}cm^{-1}$	-	418 nm, 24000 $M^{-1}cm^{-1}$	338 nm, 7800 $M^{-1}cm^{-1}$	246 nm, 15400 $M^{-1}cm^{-1}$	378 nm, 7410 $M^{-1}cm^{-1}$

Dielectric constants (ε_r) were obtained from reference Maryott 1951 [91]
‡ Buffer solution ε_r estimated to be similar to that of pure water.
† SDS ε_r obtained from Chaudhuri 2009 [92]

Table 3.2: Photostability (Degradation %/s) of ROS sensors observed in selected solvents.

	DPBF	RNO	NBD-Cl	BQ	MTT
PB ($\varepsilon_r \approx 80$) ‡	-	6.90 x 10^{-4} $\%/s$	-	0.371 $\%/s$ (w/ 418 nm LPF: 0.0479 $\%/s$)	7.32 x 10^{-4} $\%/s$
BB ($\varepsilon_r \approx 80$) ‡	-	-	0.170 $\%/s$ (w/ 418 nm LPF: 0.0194 $\%/s$)	-	-
DMSO ($\varepsilon_r = 47$)	0.586 $\%/s$ (w/ 295 nm LPF: 0.571 $\%/s$) (w/ 450 nm LPF: 0.144 $\%/s$)	-	-	-	-
SDS ($\varepsilon_r \approx 32$) †	-	1.01 x 10^{-3} $\%/s$	-	-	9.98 x 10^{-4} $\%/s$
EtOH ($\varepsilon_r = 25$)	-	2.41 x 10^{-3} $\%/s$	-	-	2.23 x 10^{-3} $\%/s$
PBOctOH	-	4.59 x 10^{-3} $\%/s$	-	-	4.89 x 10^{-3} $\%/s$
OctOH ($\varepsilon_r = 10$)	2.07 $\%/s$ (w/ 295 nm LPF: 1.80 $\%/s$)	4.88 x 10^{-3} $\%/s$	0.133 $\%/s$	0.381 $\%/s$	7.86 x 10^{-3} $\%/s$

Dielectric constants (ε_r) were obtained from reference Maryott 1951 [91]
‡ Buffer solution ε_r estimated to be similar to that of pure water.
† SDS ε_r obtained from Chaudhuri 2009 [92]

3.4.1 DPBF

The widely cited $^1O_2$ sensor, 1,3-diphenylisobenzofuran (DPBF), has been used most commonly in organic solvents, like DMF[93,94] and Acn,[95] and while it is not soluble in neat water, its use has been reported in micellar solutions and mixed alcohol/water solvents.[96] In this work, if soluble, all stock solutions were prepared in EtOH. Since reports have been made of DPBF being prepared in EtOH,[96] it was the first solvent in which a molar absorptivity measurement was performed. As can be seen in **Figure 3.1A**, the three molar absorptivity trials of DPBF in EtOH performed within 24 hours, from the same stock solution, exhibited significant inconsistencies. Trial one and two, performed minutes apart, do not agree, with trial two resulting in a molar extinction coefficient (ε) nearly ¾ of that in trial one. While the ε decreased between trials one

and two, an increase was observed between trials two and three when the solution was stored and refrigerated overnight in an amber bottle. Typically, an increase of ε for the same solution over time suggests a solubility limitation. The average ε of DPBF in EtOH is inconclusively reported as $15000 \pm 6000\ M^{-1}cm^{-1}$; significantly different from recent reports ($23000 \pm 250\ M^{-1}cm^{-1}$ in 50/50 (v/v) EtOH/H_2O.[96] In addition, after prolonged storage (>2 days) the DPBF in EtOH stock solution formed a white precipitate, suggesting the solute either reprecipitated or reacted with the solvent to produce a new compound. After these results, it was concluded that DPBF was not stable enough in EtOH for use in this work.

Since many citations indicated use of DPBF in organic solvents, like DMSO and DMF, molar absorptivities of DPBF were also conducted in Acn, DMSO, and OctOH. Due to the interactions between DPBF and EtOH described above, glassware in these runs were cleaned with Acn, instead of EtOH, as any residual EtOH caused the formation of a white precipitate. As shown in **Figure 3.1D**, the stability of DPBF in Acn was improved in comparison to the EtOH trials, however, the results were still inconsistent, with an reported ε of $16800 \pm 3000\ M^{-1}cm^{-1}$. In DMSO (as shown in **Figure 3.1C**), DPBF was more stable, with some variation between day of use, and a reported ε of $26000 \pm 4000\ M^{-1}cm^{-1}$. DPBF was most stable in OctOH (as shown in **Figure 3.1D**), with a reported ε of $32700 \pm 3000\ M^{-1}cm^{-1}$. Still, the stability of DPBF in all solvents studied here, is inconsistent at best, and may suggest that the compound is either too sensitive to ambient conditions, or reactive towards the solvents themselves.

In addition to the stability concerns of DPBF in the solvents studied above, the photodegradation of the chromophore was tested. As stated previously, a degradation rate of less than 5% during the measurement range (15 minutes) is ideal—equivalent to

~0.0055 %/s. As illustrated in **Figure 3.2A** & **B**, DPBF degrades significantly in the first few seconds of irradiation. This is less than optimal performance for a sensor that is so widely used in photosensitization studies. Since this sensor is often used in studies conducted with narrow excitation light sources, photodegradation controls in which a long–pass filter (LPF) was placed in front of the sample cuvette, were conducted (**Figure 3.2C**–**E**). DPBF has been shown to self–photooxidate through absorption in the ultra violet (UV) region,[55] therefore a 295 nm LPF was used to block any UV radiation incident on the sample. In both OctOH and DMSO, the 295 nm LPF did not sufficiently reduce the photodegradation rate of DPBF, only reducing the rate by ~15% and ~4% in OctOH and DMSO, respectively. Using a LPF with a 450 nm cutoff significantly decreased the rate of photodegradation; however the degradation rate was still greater than 0.0055 %/s, making the sensor unstable for this, and other photooxidation work in which broadband sources are used.

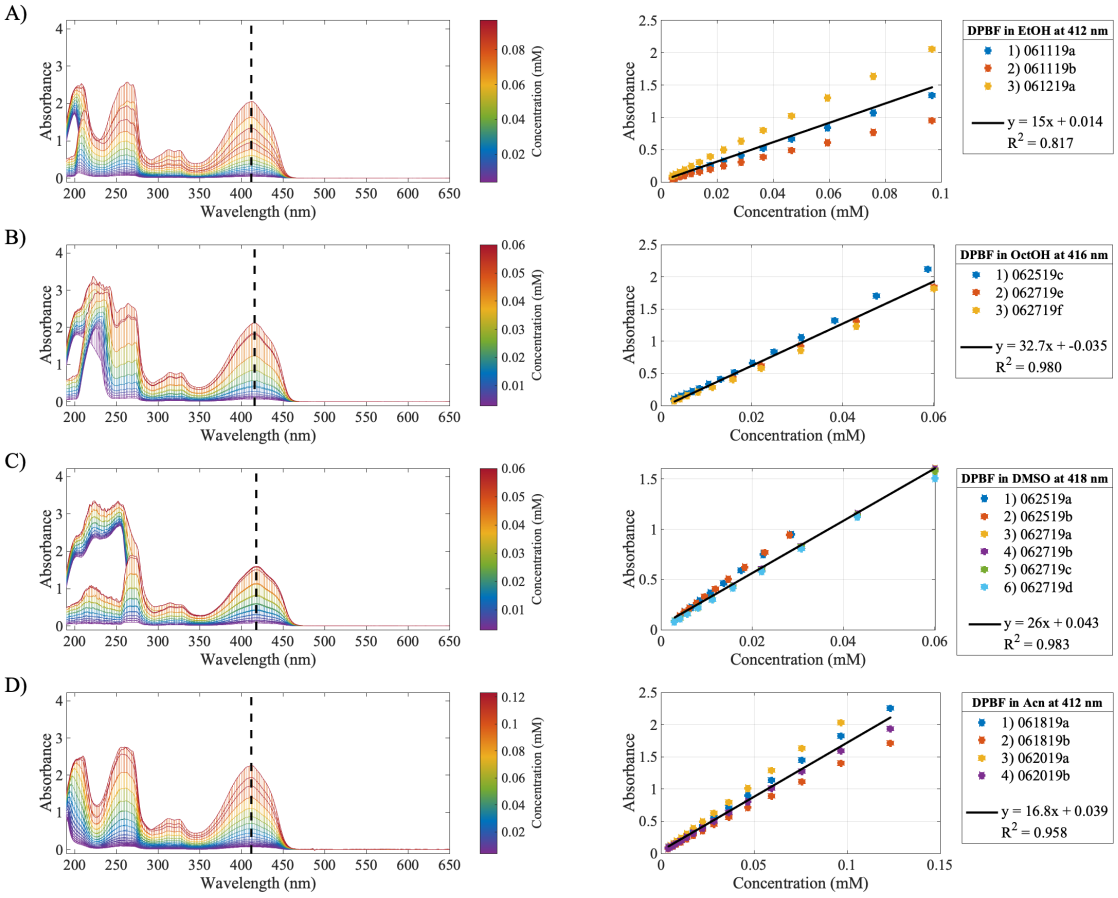

Figure 3.1: Molar absorptivity measurements for DPBF in **A)** EtOH, **B)** OctOH, **C)** DMSO, and **D)** Acn. Each figure panel contains composite spectra from molar absorptivity measurement sets (left) and a composite linear regression at the chromophores wavelength of maximum absorbance (right).

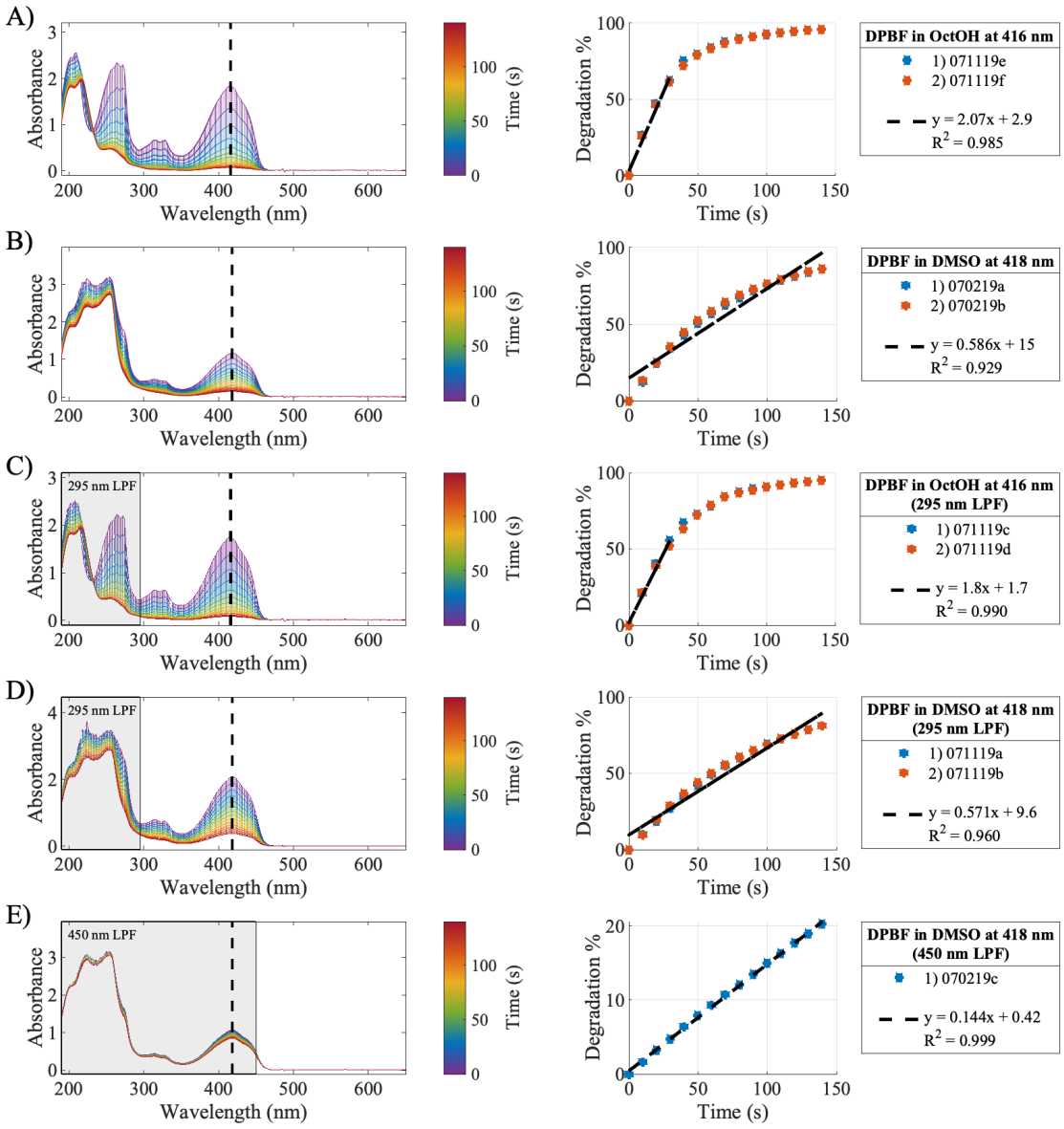

Figure 3.2: Photodegradation measurements for DPBF in **A)** OctOH, **B)** DMSO, **C)** OctOH filtered by a 295 nm LPF, **D)** DMSO filtered by a 295 nm LPF, and **E)** DMSO filtered by a 450 nm LPF. Each figure panel contains composite spectra from the photodegradation measurement sets (left) and a composite linear regression of the chromophore degradation % at the chromophores wavelength of maximum absorbance (right). [DPBF] = 50 μM.

3.4.2 ADPA

The molar absorptivity of the anthracene derivative ADPA was determined in pH 7.4 PB, 5% SDS, and EtOH. As can be seen in **Figure 3.3**, the stability of ADPA in these solvents is well behaved; indicating that ADPA may be utilized in these solvents with success. The determined ε was $9040 \pm 40\ M^{-1}cm^{-1}$ in PB, $9120 \pm 20\ M^{-1}cm^{-1}$ in SDS, and $10450 \pm 10\ M^{-1}cm^{-1}$ in EtOH; all similar to a previously reported value ($8300\ M^{-1}cm^{-1}$ in pH 10.5 ammonium acetate)[60] Unfortunately, the evaluation of ADPA's photodegradation was not able to be performed, and remains a future direction of this work.

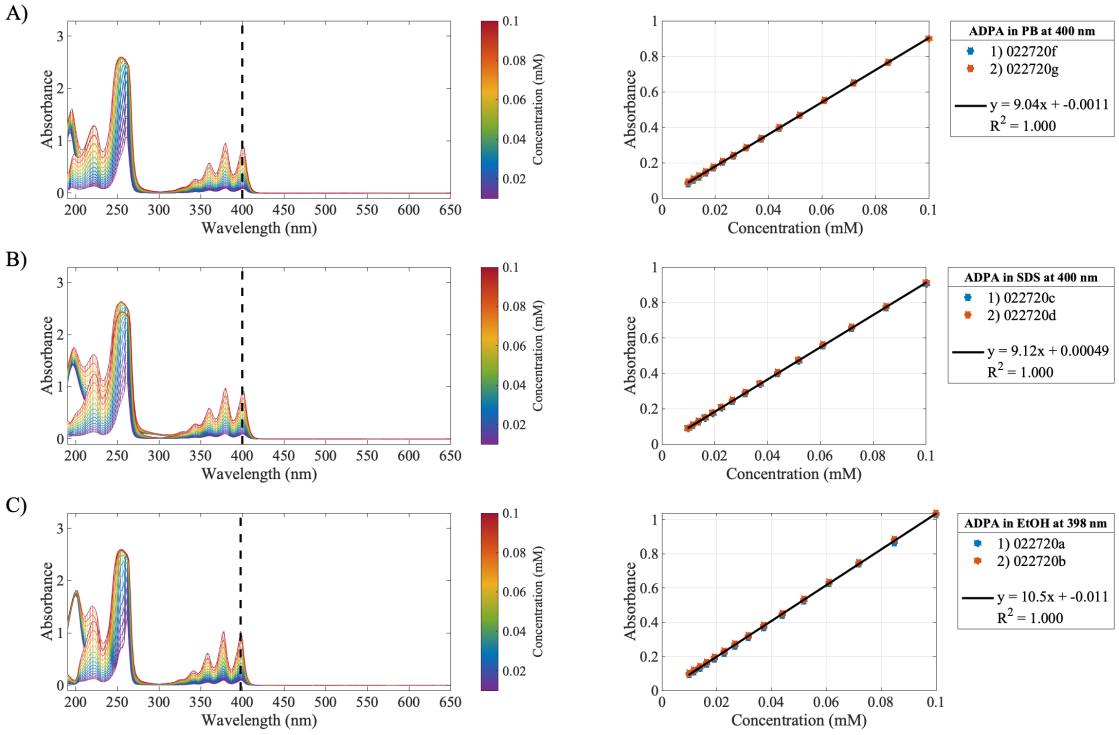

Figure 3.3: Molar absorptivity measurements for ADPA in **A)** pH 7.4 PB, **B)** 5% SDS, and **C)** EtOH. Each figure panel contains composite spectra from molar absorptivity measurement sets (left) and a composite linear regression at the chromophores wavelength of maximum absorbance (right).

3.4.3 Imd plus RNO

The imidazole plus RNO method requires two reagents, Imd and RNO; therefore, the stability of each reagent was analyzed individually. To begin, the molar absorptivity of RNO was determined in pH 7.4 PB, 5% SDS, OctOH, PBOctOH, and EtOH. As is illustrated in **Figure 3.4**, RNO has a nearly ideal linear correlation (≥0.997) between concentration and absorbance in all of the selected solvents. RNO is generally positively solvatochromic, i.e., there is a bathochromic (red) λ_{max} shift as solvent dielectric constant (ε_r) increases. Moreover, the sensor band exhibits a hypochromic shift, decreasing in ε by approximately 14% as the dielectric constant (ε_r) increases from 10 in octanol to 80 in phosphate buffer.

In addition, RNO has relatively stable behavior under the simulated solar irradiation conditions tested here, as shown in **Figure 3.5**. In all the solvents studied, the sensor's photodegradation was less than 0.005 %/s; all below the ideal 0.0055 %/s threshold. The trend in rate of sensor photodegradation was as follows: OctOH>PBOctOH>EtOH>PB>SDS, in which RNO degrades the fastest in OctOH at a rate of 0.0049 %/s, and the slowest in SDS at a rate of 0.0010 %/s; nearly following an inverse relationship to solvent ε_r, with the exception of SDS. In some cases, the sensor's photodegradation control had relatively low reproducibility. In PB, the observed low correlation coefficient (0.817) may be due to low signal to noise quality as a result of minimal bleaching (<1% over 15 minutes) between each measurement. On the other hand, in OctOH the low correlation coefficient (0.894) may be due to a baseline shift, creating disparity between separate trials and the composite linear regression. Plotting linear regressions for each individual trial improves the overall correlation. These results, coupled with the nearly ideal linear correlation between the sensor's concentration and absorbance, suggests RNO as a strong candidate for $^1O_2$ detection

using UV–Vis spectrophotometry in environmentally and biologically relevant conditions.

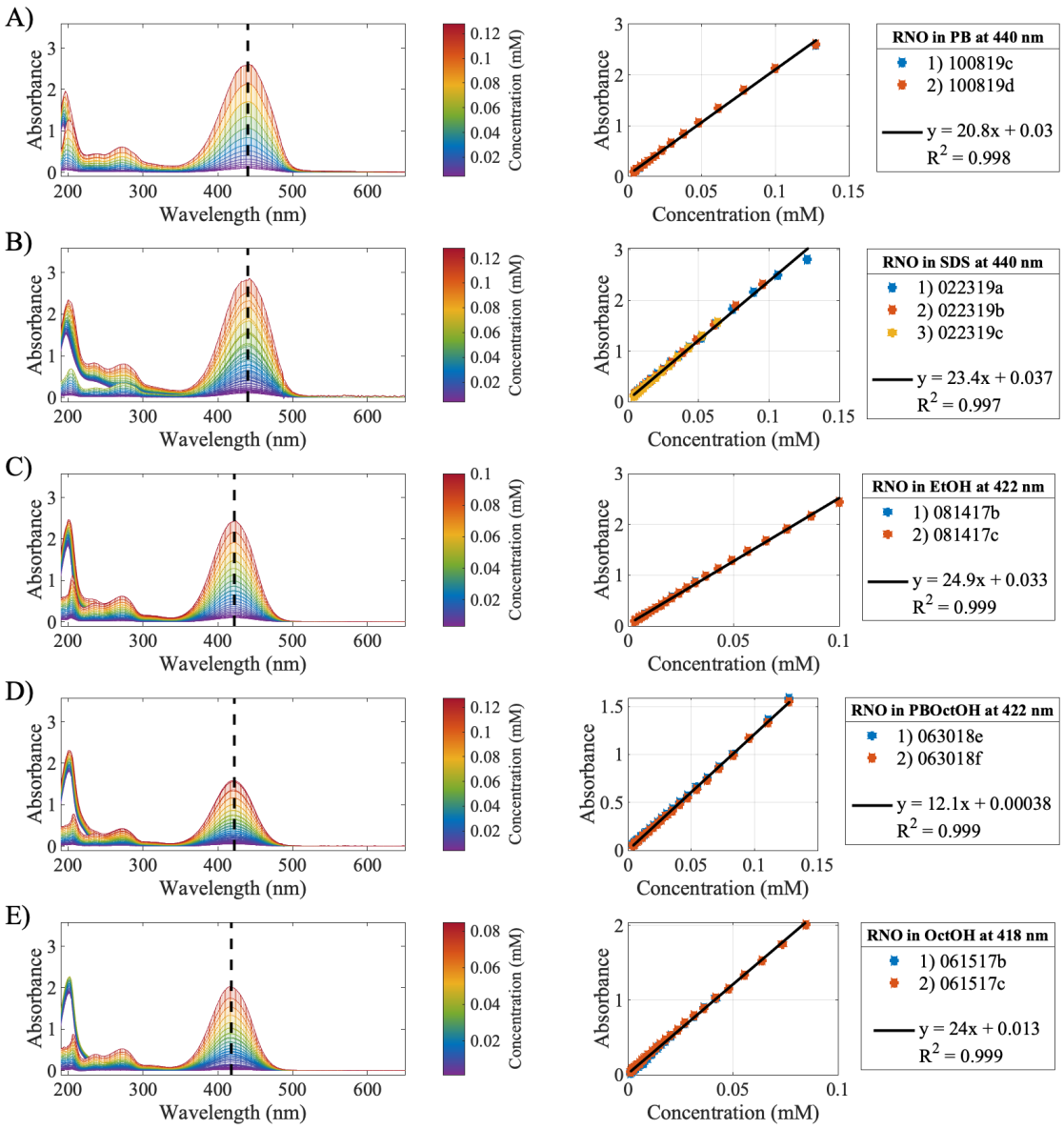

Figure 3.4: Molar absorptivity measurements for RNO in **A)** pH 7.4 PB, **B)** 5% SDS, **C)** EtOH, D) PBOctOH, and **E)** OctOH. Each figure panel contains composite spectra from molar absorptivity measurement sets (left) and a composite linear regression at the chromophores wavelength of maximum absorbance (right).

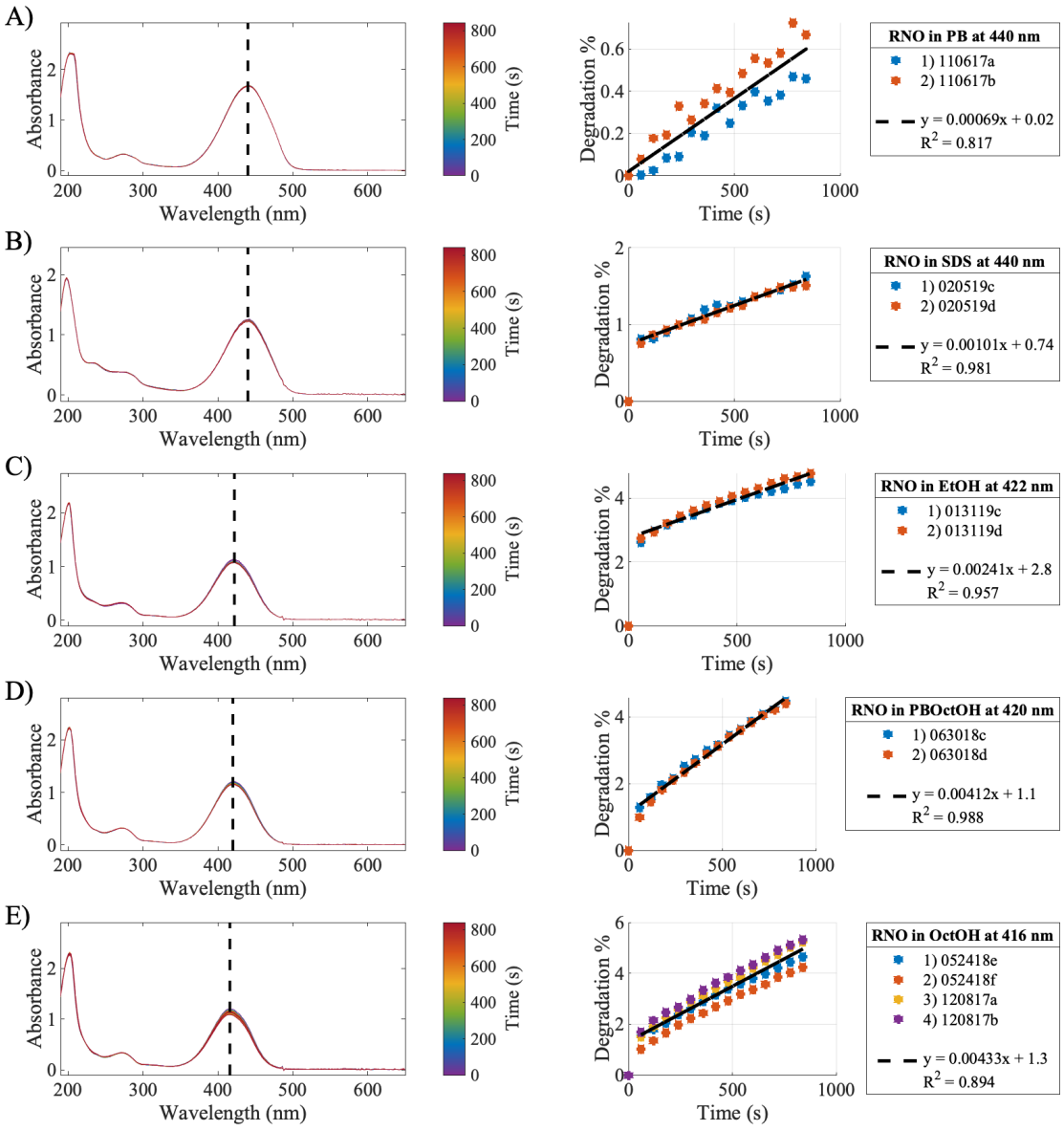

Figure 3.5: Photodegradation measurements for RNO in **A)** pH 7.4 PB, **B)** 5% SDS, **C)** EtOH, **D)** PBOctOH, and **E)** OctOH. Each figure panel contains composite spectra from measurement sets (left) and a composite linear regression of the chromophore degradation % at the chromophores wavelength of maximum absorbance (right). [RNO] = 50 µM.

The second component of the Imd plus RNO method, Imd, has a much more complex relationship between its absorbance and concentration. As shown in

Figure 3.6, multiple features emerge in the Imd spectrum as concentration increases. At low concentrations (<0.5 mM), there is an approximate wavelength of maximum absorbance near 210 nm; however, this peak red shifts with each concentration addition in all solvents. At higher concentrations (>0.5 mM), a new peak appears around 284 nm, that increases linearly in all solvents studied. While I not found insight to suggest the cause of these spectral abnormalities, these spectral changes suggest that the quenchers ability to act as an effective $^1O_2$ accepter may vary with concentration. Due to the inconsistencies in the spectrum of Imd, the photodegradation results were not tracked over time at a single wavelength; though, over the typical measurement range (15 mins), there were no observations of Imd spectral degradation at low or high Imd concentration.

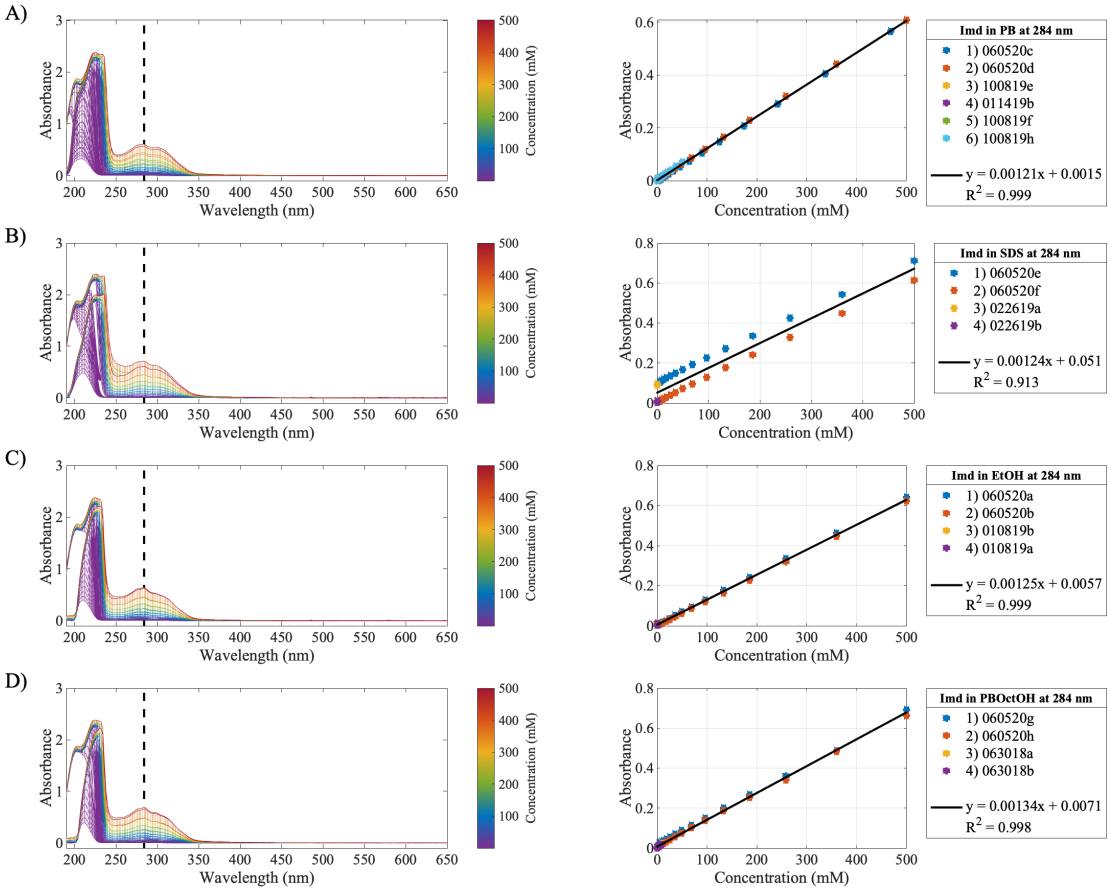

Figure 3.6: Molar absorptivity measurements for Imd in **A)** pH 7.4 PB, **B)** 5% SDS, **C)** EtOH, and **D)** PBOctOH. Each figure panel contains composite spectra from molar absorptivity measurement set (left) and a composite linear regression at the chromophores wavelength of maximum absorbance (right).

3.4.4 NBD-Cl

The molar absorptivity and photodegradation of NBD-Cl in pH 10.0 BB and OctOH, as well as the molar absorptivity in EtOH, were determined. **Figure 3.7** shows that NBD-Cl has a nealy ideal linear correlation (≥0.997) between its absorbance and concentration in the solvents studied here. The ε of the sensor was found to be $10400 \pm 200\ M^{-1}cm^{-1}$ in pH 10.0 BB, $8770 \pm 20\ M^{-1}cm^{-1}$ in EtOH, and $7800 \pm 100\ M^{-1}cm^{-1}$ in OctOH. Perhaps because NBD-Cl as a $O_2^{\bullet-}$ sensor is primarily

focused around the product, I have not found reported molar absorptivities of the NBD-Cl sensor for comparison to these results. Since NBD-Cl functions as a $O_2^{\bullet-}$ sensor by forming a product with a lambda max around 470 nm, it is noteworthy that during the molar absorptivity measurements in this work, no peak appears around 470 nm; suggesting that the sensor is not self–oxidizing during the control.

In the photodegradation measurements of NBD-Cl, it was discovered that the sensor is not stable under broadband, simulated sunlight. As shown in **Figure 3.8A** & **B**, NBD-Cl degrades quickly in both pH 10.0 BB and OctOH, in which the initial rate of degradation in the aqueous BB was 0.170 %/s, and 0.113 %/s in OctOH. These values are higher than the ideal sensor degradation limit (0.0055 %/s) outlined above, and therefore unacceptable. As with previous sensors that were unstable under the broadband simulated sunlight, a LPF was used to remove higher energy wavelengths. In **Figure 3.8C**, the results of using a 418 nm LPF are shown; the LPF slowed the sensor's degradation to 0.0194 %/s in BB, roughly 10% of the rate without the filter, and within the acceptable degradation limit. In either case though, it is of concern that a photoproduct formed with a similar spectra profile to that of the expected $O_2^{\bullet-}$–NBD-Cl product. This suggests that in aqueous BB, NBD-Cl may self–oxidize; which could compromise the efficiency of the sensor for $O_2^{\bullet-}$ determinations, even when a narrowband excitation beyond 418 nm is used.

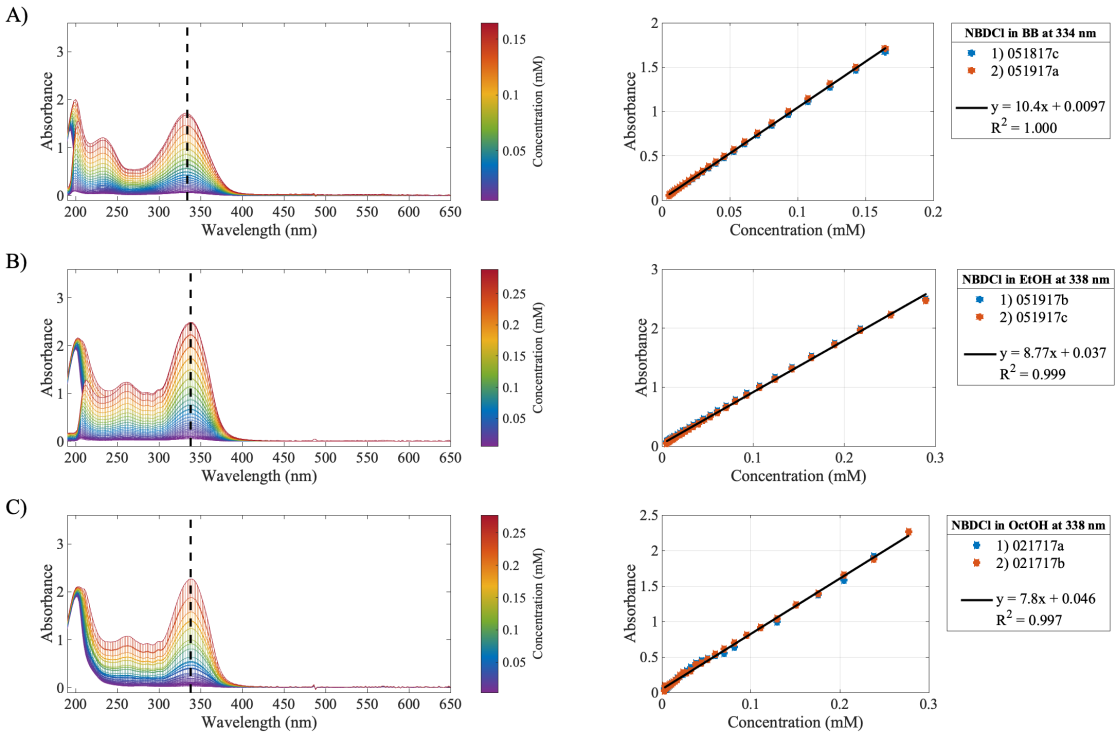

Figure 3.7: Molar absorptivity measurements for NBD-Cl in **A)** pH 10.0 BB, **C)** EtOH, and **D)** OctOH. Each figure panel contains composite spectra from molar absorptivity measurement sets (left) and a composite linear regression at the chromophores wavelength of maximum absorbance (right).

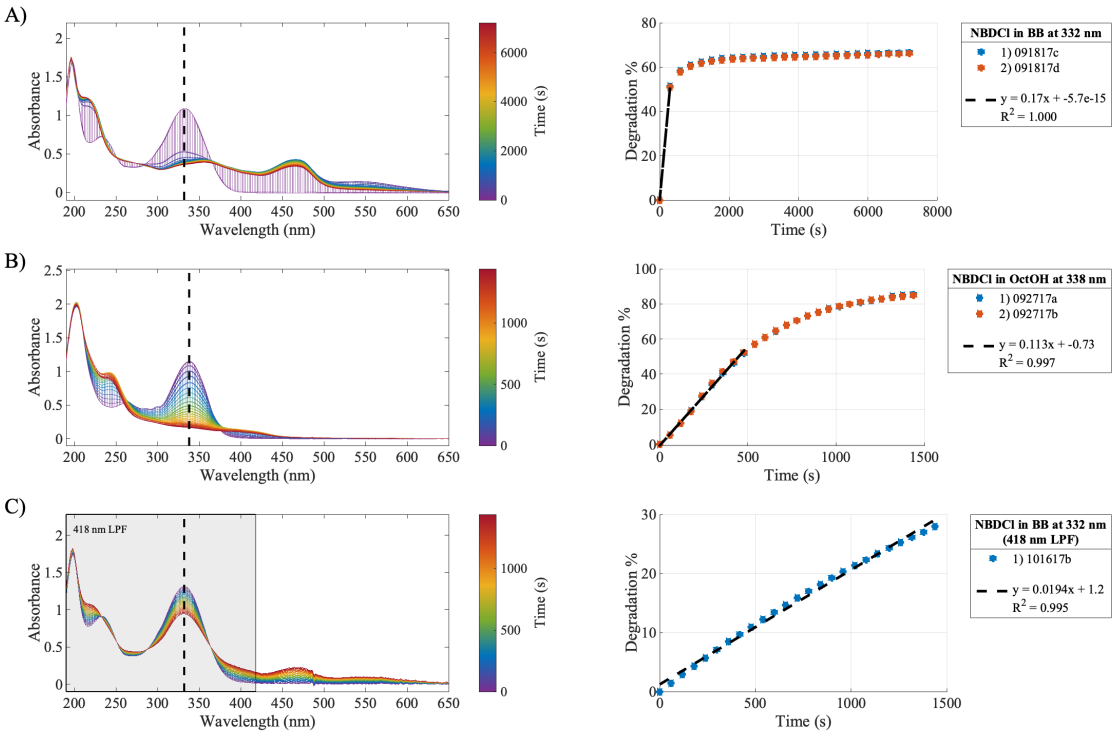

Figure 3.8: Photodegradation measurements for NBD-Cl in **A)** pH 10.0 BB, B**)** OctOH, and **C)** pH 10.0 BB with a 418 nm LPF placed before the sample. Each figure panel contains composite spectra from measurement sets (left) and a composite linear regression of the chromophore degradation % at the chromophores wavelength of maximum absorbance (right). [NBD-Cl] = 100 µM.

3.4.5 BQ

The molar absorptivity and photodegradation of the quinone–based $O_2^{\bullet-}$ sensor, BQ, was tested in aqueous pH 7.4 PB and OctOH. As is shown in **Figure 3.9**, in both solvents, BQ has a relatively well–behaved correlation between its concentration and absorbance. In pH 7.4 PB, the composite correlation coefficient is compromised by the spectral baseline alteration that occurs between the air and solvent blank trials. The ε was determined as 14000 ± 500 $M^{-1}cm^{-1}$ and 15400 ± 1000 $M^{-1}cm^{-1}$ in PB and OctOH, respectively. Nonetheless, the sensor stability in the two solvents is acceptable.

On the other hand, the sensors stability under the broadband solar simulator is less ideal. In pH 7.4 PB, the initial rate of degradation was 0.371 %/s, significantly greater than the ideal 0.0055 %/s control rate. Likewise, in OctOH, the initial degradation rate was 0.229 %/s, again greater than the ideal rate. As was done with similarly performing sensors, a LPF with a cutoff wavelength of 418 nm was used to slow the degradation in pH 7.4 PB. With the filter the degradation was reduced to 0.0479 %/s; ~13% of the rate without the filter. Even with the reduction in degradation, and the lack of a photoproduct at the expected BQ–$O_2^{\bullet-}$ product peak, this sensor's stability is unacceptable for this and other photooxidation work in which a broadband light source is used.

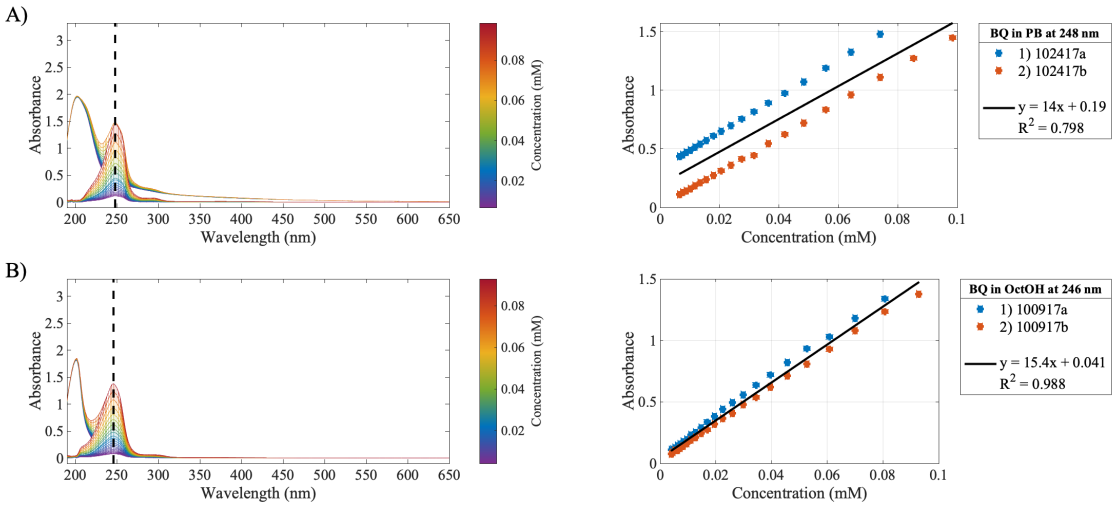

Figure 3.9: Molar absorptivity measurements for BQ in **A)** pH 7.4 PB, and **B)** OctOH. Each figure panel contains composite spectra from molar absorptivity measurement sets (left) and a composite linear regression at the chromophores wavelength of maximum absorbance (right).

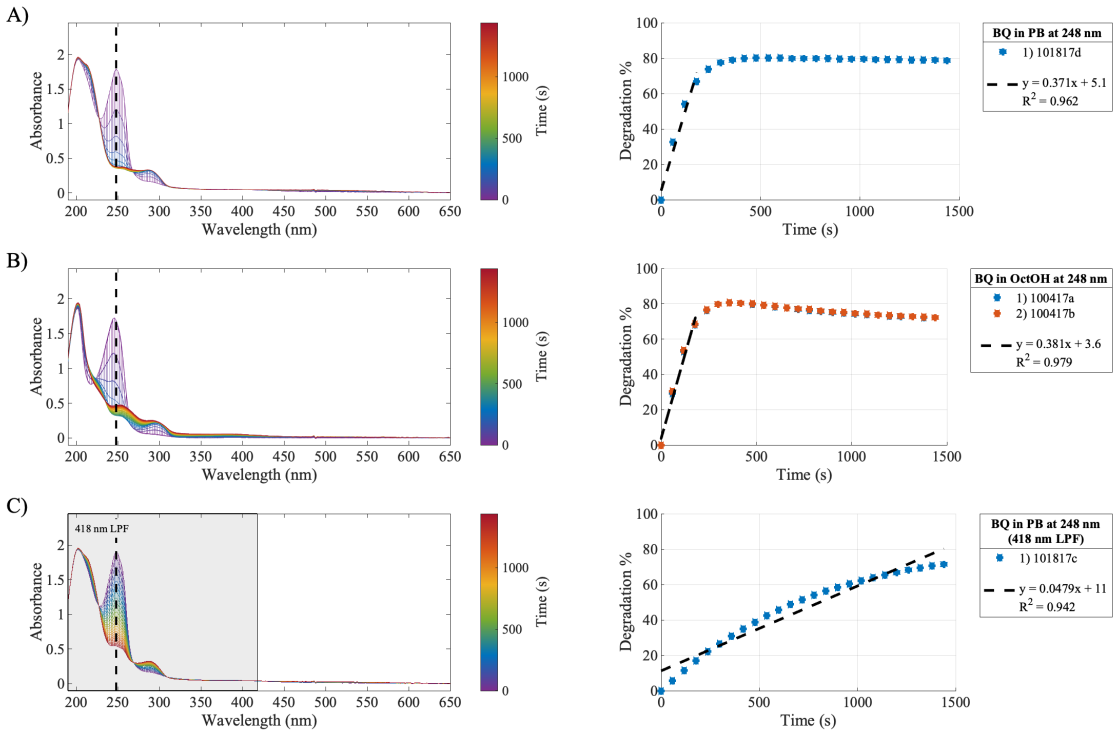

Figure 3.10: Photodegradation measurements for BQ in **A)** pH 7.4 PB, **B)** OctOH and **C)** pH 7.4 PB with a 418 nm long–pass filter placed before the sample. Each figure panel contains composite spectra from measurement sets (left) and a composite linear regression of the chromophore degradation % at the chromophores wavelength of maximum absorbance (right). [BQ] = 100 µM.

3.4.6 MTT

The molar absorptivity and photodegradation of the tetrazolium $O_2^{\bullet-}$ sensor, MTT, was analyzed in pH 7.4 PB, 5% SDS, EtOH, PBOctOH, and OctOH. The ε of MTT, as shown in **Figure 3.11**, had a high correlation coefficient (>0.992) in all solvents when the absorbance of the sensor at its wavelength of maximum absorbance was plotted against sensor concentration. There was no notable trend in ε nor wavelength of maximum absorbance across the various solvents. The ε was determined as $6680 \pm 80\ M^{-1}cm^{-1}$ in PB, $6400 \pm 300\ M^{-1}cm^{-1}$ in SDS, $8100 \pm 200\ M^{-1}cm^{-1}$ in EtOH, $7130 \pm 100\ M^{-1}cm^{-1}$ in PBOctOH, and $7400 \pm 200\ M^{-1}cm^{-1}$ in OctOH.

In all of the photodegradation data sets, with the exception of OctOH, the rate of degradation was below the ideal limit of 0.0055 %/s. The degradation rates in PB, SDS, EtOH, and PBOctOH were 0.000732 %/s, 0.000998 %/s, 0.00223 %/s, and 0.00489 %/s, respectively. In neat OctOH the degradation rate jumped to 0.00786 %/s; just above the ideal limit. Since the aqueous "water pools" in neat OctOH are likely smaller than that in the PBOctOH, the increased rate may be due to an increase in the effective concentration of MTT; though this conclusion is not supported by the molar absorptivity data, in which the molar absorptivity of MTT in OctOH is not enough similar to that in PB. Nonetheless, at this stage the sensor is promising for use in environmentally and biologically relevant conditions selected here for $O_2^{\bullet -}$ detection.

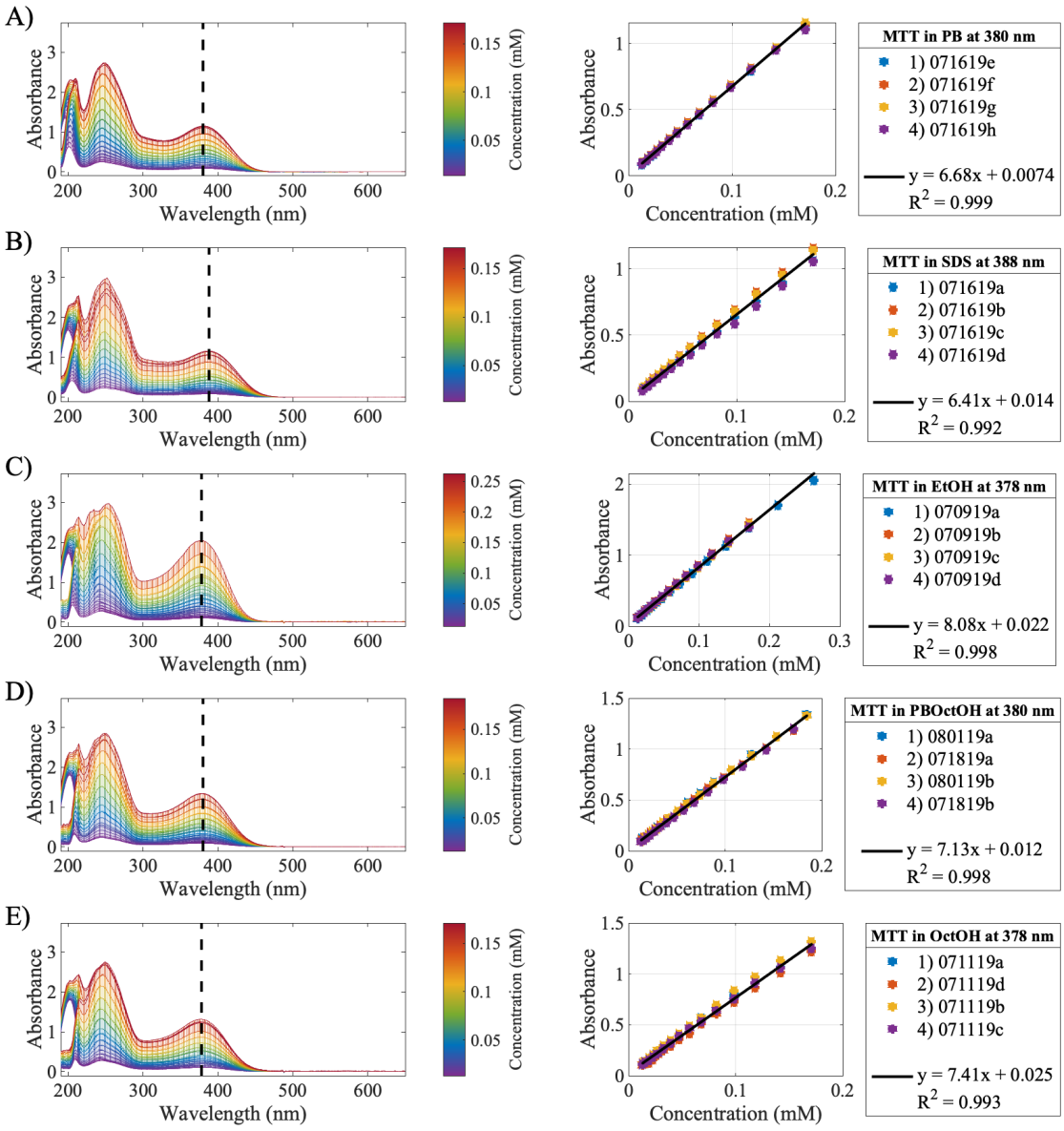

Figure 3.11: Molar absorptivity measurements for MTT in **A)** EtOH, **B)** pH 7.4 PB, **C)** SDS, **D)** OctOH, and **E)** PBOctOH. Each figure panel contains composite spectra from all molar absorptivity measurements (left) and a composite linear regression at the chromophores wavelength of maximum absorbance (right).

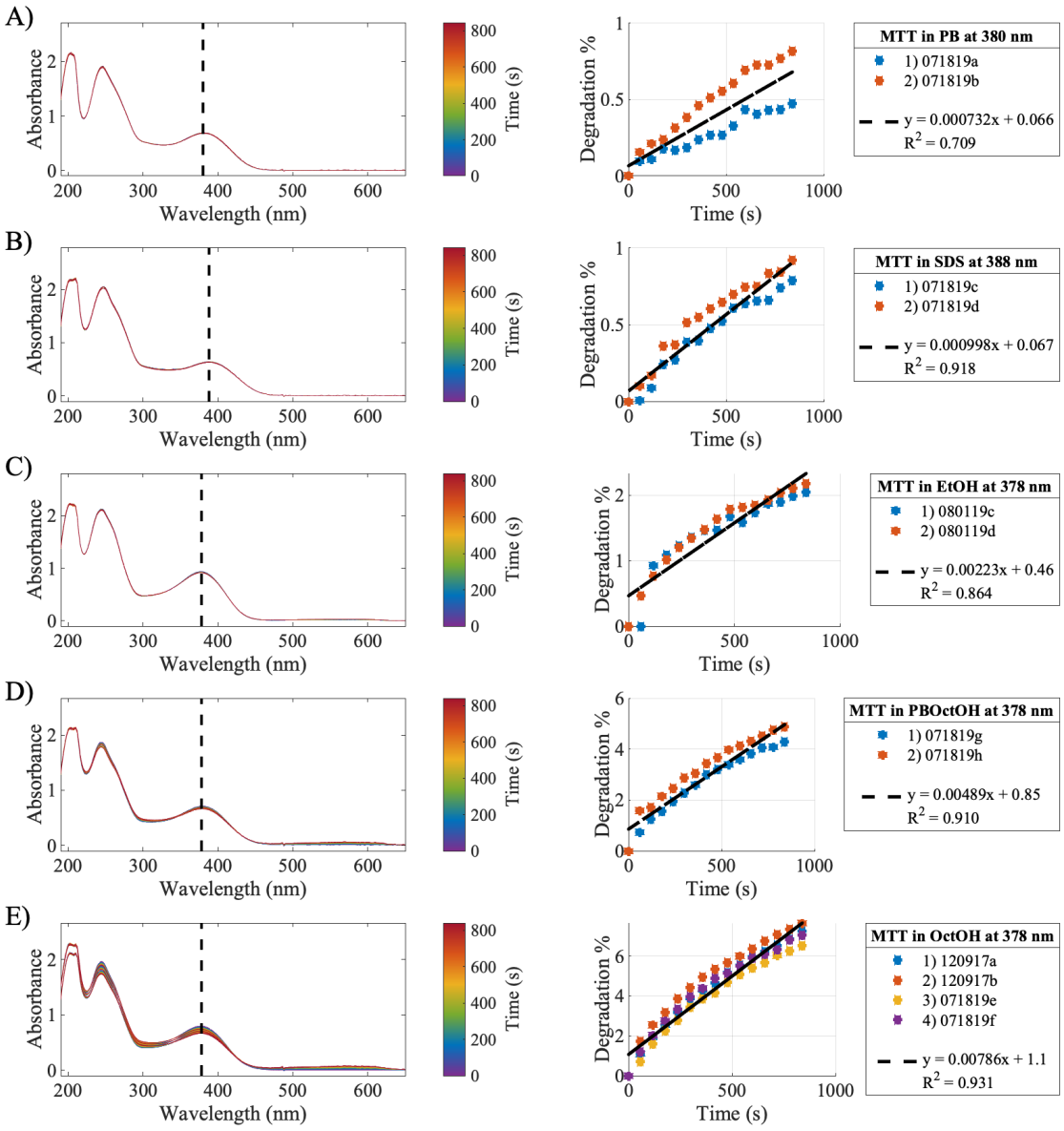

Figure 3.12: Photodegradation measurements for MTT in **A)** pH 7.4 PB, **B)** 5% SDS, **C)** EtOH, **D)** PBOctOH, and **E)** OctOH. Each figure panel contains composite spectra from measurement set (left) and a composite linear regression of the chromophore degradation % at the chromophores wavelength of maximum absorbance (right). [MTT] = 100 µM.

3.5 Conclusions

In this work, the stability of several singlet oxygen ($^1O_2$) and superoxide ($O_2^{\bullet-}$) sensors were evaluated for their use in environmentally or biologically relevant samples, including isotropic and microheterogeneous solvents, as well as broadband simulated sunlight. Sensors stability was evaluated using two types of assay control measurements: broadband molar absorptivity, and photostability under broadband simulated sunlight. From the molar absorptivity measurements, the sensors stability in each solvent was observed. Through the photostability measurements, the feasibility of using the sensor in photooxidation studies was evaluated. Out of the six sensors assessed, two were determined acceptable for future work, the Imd plus RNO method for $^1O_2$ detection, and MTT for $O_2^{\bullet-}$ detection.

The Imd plus RNO method, consisting of a two–step mechanism in which Imd quenches $^1O_2$ and then bleaches the sensor, RNO, was deemed appropriate for further investigation due to the sensor's strong linear correlation in molar absorptivity measurements and limited sensor bleaching in the photodegradation control. In the five solvents studied—pH 7.4 PB, 5% SDS, EtOH, PBOctOH, and OctOH— the rate of sensor degradation was below the ideal limit for this work (0.0055 %/s). However, it was found that Imd does not follow a linear trend in its absorbance over the broad concentration range potentially needed for the assay. Though Imd has non–linear bands, it acts as a catalyst in the mechanism, not being consumed, so the non–linearity may not be an issue in future work.

The MTT method for superoxide detection was the second sensor considered suitable for future work. Similar to RNO, MTT has a strong linear correlation in molar absorptivity measurements and limited sensor bleaching in the photodegradation control. In the five solvents studied—pH 7.4 PB, 5% SDS, EtOH, PBOctOH, and

OctOH—the rate of sensor degradation was below the ideal limit for this work (0.0055 %/s). One aspect of the method that may remain a challenge however, is the solubility of the monoformazan product that forms following MTT reacting with $O_2^{\bullet-}$. The lack of solubility could make it challenging for use in the aqueous PB and SDS solvents. Though, the stable behavior of the MTT sensor in the work presented here, suggests that the MTT absorbance may be used to monitor the disappearance of the sensor and in turn provide an indirect determination of $O_2^{\bullet-}$ formation.

The other sensors studied, DPBF, NBD-Cl, and BQ were all eliminated from future work in this study due to the instability of their molar absorptivity measurements and/or photodegradation measurements under broadband simulated sunlight. Unfortunately, the work with ADPA was cut short, and its photostability remains to be measured. In addition, there are more ROS sensors in recent and foundational publications that were not addressed here and should be considered as well. For example, furfuryl alcohol (FFA) is a highly regarded $^1O_2$ sensor used in many photooxidation studies utilizing mixed and heterogeneous media. XTT (2,3-bis(2-Methoxy-4-nitro-5-sulphophenyl)-5-[(phenylamino)carbonyl]-2*H*-tetrazolium hydroxide) is a highly regarded, water–soluble $O_2^{\bullet-}$ sensor used in many recent photooxidation studies. These two sensors, and many more, may perform well under the environmentally and biologically relevant conditions of this work and should be evaluated in the future.

Overall, the results of this work highlight the necessity of control measurements in the use of chemical sensors. Many of the sensors evaluated here have been used for years in large and broad scale of applications. Some of the results presented here were surprising, and suggest that sensors, like DPBF, that has over a thousand citations, may

be suspectable to substantial degradation in the control. If this degradation is not being accounted for, the subsequent evaluation of the sensor's degradation could be misinterpreted.

Chapter 4

EFFICIENCY COMPARISON OF THE IMIDAZOLE PLUS RNO METHOD FOR SINGLET OXYGEN DETECTION IN BIORELEVANT SOLVENTS

4.1 Abstract

Singlet oxygen ($^1O_2$), is the focus of study in many fields, including phototoxicity, antioxidant activity, pollutant weathering, photodynamic therapy, and water disinfection. The imidazole plus RNO (Imd/RNO) method, originated by Kraljić and El Mohsni, is commonly used to monitor $^1O_2$ production. In this method, $^1O_2$ is quenched by an acceptor, imidazole (Imd), during the formation of a trans-annular peroxide intermediate that bleaches the colorimetric sensor, p-nitrosodimethylaniline (RNO). Though the method has been widely used, including to monitor $^1O_2$ production in complex environments, such as surfactants and cells, studies reporting the efficiency of the assay in complex solvents have not been reported.

In this research, the efficiency of the Imd/RNO method in complex, biorelevant solvents, i.e., sodium dodecyl sulfate, octanol, and phosphate buffer saturated octanol, was compared to reference solvents, i.e., phosphate buffer, ethanol, and methanol, using Rose Bengal photosensitization to produce $^1O_2$ and time-resolved, broadband UV–Vis absorbance measurements. Rates of sensor bleaching and sensitizer photodegradation were simultaneously monitored in each solvent to investigate correlations between the disappearance rates of sensor and sensitizer. To illustrate the efficiency of the method across the solvents, the quantum yields of $^1O_2$ production (ϕ_Δ) in each solvent were calculated using a relative actinometric method.

The dependence of sensor bleaching and sensitizer degradation on acceptor concentration and solvent polarity, and the results of assay controls indicate differences in mechanisms underlying the reactions comprising the Imd/RNO method. These results demonstrate the need for caution and controls when using the method in complex samples including those containing cells, tissues or nanoscale particles. Much of the contents of this chapter have been published previously.[18]

4.2 Introduction

Monitoring singlet oxygen ($^1O_2$), a reactive oxygen species (ROS), is important to investigations and applications in many fields,[97] including phototoxicity,[67] antioxidant activity,[64,98] pollutant weathering,[99] DNA damage,[100] photodynamic therapy,[101] electrochemical (bio)sensing,[102] and water disinfection.[103] Routine $^1O_2$ monitoring can be challenging because it's an energetic and short-lived species that can be produced by several chemical reactions, biological processes, or photoinduced processes—particularly type II photosensitization, as shown in **Figure** Error! Reference s ource not found..

Monitoring $^1O_2$ is complicated because its spectrum appears in the near infrared. Direct measurement of $^1O_2$ phosphorescence emission near 1270 nm is the definitive detection method; however, this technique requires specialized equipment and typically produces a weak signal.[104] Consequently, $^1O_2$ is often detected indirectly via its impact on more readily observed sensors. Many molecular sensors have been developed as convenient and seemingly reliable detection alternatives for $^1O_2$ emission. In a recent review, You[104] categorized $^1O_2$ sensors into three types by signaling modalities: absorption-based sensors, photoluminescent sensors, and chemiluminescent sensors. Amongst the absorption-based sensors, 1,3-diphenylisobenzofuran (DPBF), 9,10-

Diphenylanthracene (DPA), p-nitrosodimethylaniline (RNO), and furfuryl alcohol (FFA) are the most widely cited throughout the last two decades. Though an extensive list of $^1O_2$ sensors is available,[51] including widely cited chemical sensors, concerns regarding accurate and reliable singlet oxygen determinations continue to be reported,[13,14] because the dynamic range and selectivity required for many biological and environmental samples exceeds the performance of most methods in wide use.

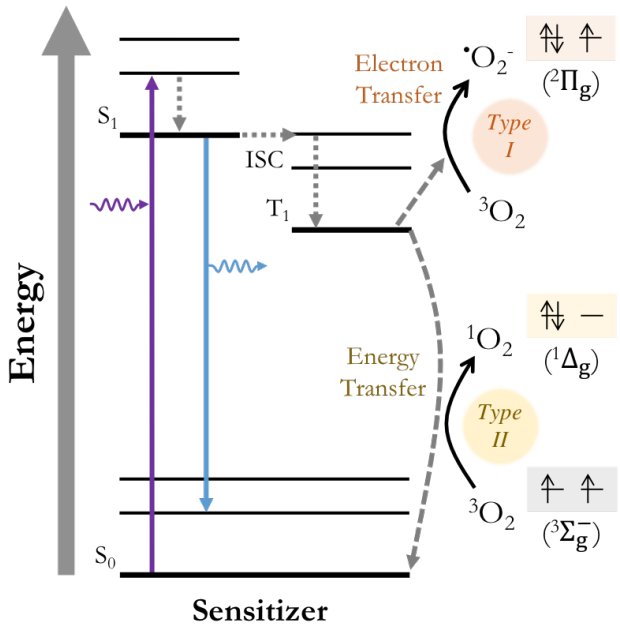

Figure 4.1: Generalized photosensitization mechanisms of type I and type II photosensitization that result in the production of superoxide and singlet oxygen, respectively; where either pathway could take place in a complex system. ISC: intersystem crossing.

The imidazole plus RNO (Imd/RNO) method, originated by Kraljić and El Mohsni, was developed to monitor $^1O_2$ in aqueous solution.[62] In this method, $^1O_2$ is quenched by the acceptor, imidazole (Imd), during the formation of a trans-annular

peroxide intermediate that goes on to bleach the sensor, RNO. In the mechanism offered by Kraljić and El Mohsni, shown in **Scheme** Error! Reference source not found., Imd is released as the peroxide bleaches the sensor. In their original publication, Kraljić and El Mohsni analyzed the dependence of the sensor bleaching on acceptor concentration, reporting maximal sensor bleaching for Imd concentrations in the mM range in aqueous phosphate buffer (PB); this range was later confirmed in aqueous buffer by Krishna et al. and Zhang et al.[71,105]

The Imd/RNO method has been used in the subsequent 40 years to monitor $^1O_2$ production by antioxidants,[64] nanocarriers,[65,66] phototoxic compounds,[67] coumarins,[63,68] anthraquinones,[69] porphyrins,[70] human lens proteins,[71] and iron-sulfur proteins.[72] Many of these studies were carried out in complex, microheterogeneous media containing surfactants,[67] protein suspensions,[71,72] and nanoparticles.[65,66] In spite of this wide range of applications, studies measuring the efficiency of the Imd/RNO method for $^1O_2$ detection in solvents more complex than aqueous PB have not been reported.

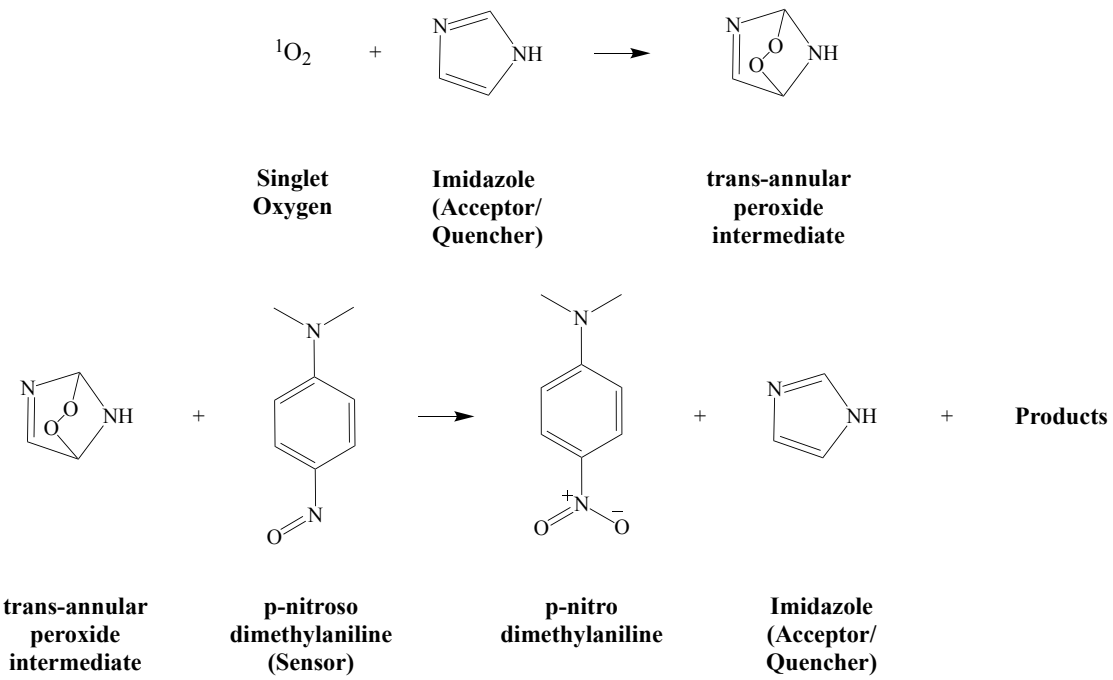

Figure 4.2: Singlet oxygen capture by Imd and subsequent bleaching of RNO by the Imd–$^1O_2$ trans-annular peroxide intermediate, as described by Kraljić and El Mohsni (1978)[62]

In addition to singlet oxygen production rates, several researchers have used the Imd/RNO method in a relative actinometric approach to compute relative $^1O_2$ quantum yields, ϕ_Δ, for new photosensitizers.[63,68–71] In this approach, a reference sensitizer is measured under the same conditions as the new sensitizer, then the new sensitizer quantum yield ($\phi_\Delta$is calculated from the reference quantum yield, $\phi_{\Delta\,Ref}$, by scaling to a ratio of the $^1O_2$ production rates of the two sensitizers:

$$\phi_\Delta = \phi_{\Delta\,Ref} \bullet [V_{AO2}/V_{AO2\,Ref}] \qquad \textbf{4.1}$$

where V_{AO2} is the apparent rate of $^1O_2$ production by the new photosensitizer, and $V_{AO2\,Ref}$ is the apparent rate of $^1O_2$ production by the reference sensitizer.[26] Gottschalk et al.[106] adapted the relative actinometric approach for use on the same sensitizer across solvents by ensuring that the rate determinations in **Equation 4.1** are conducted above

a critical concentration of the $^1O_2$ quencher, $[A]_{crit.}$, to insure zero order reaction kinetics with respect to $^1O_2$ quencher rates. The critical concentration exists when it is clear that $^1O_2$ quenching by the sensor is the dominant process in both solvents. This condition is indicated when the ratio of $^1O_2$ production in the new solvent and reference solvent ($V_{AO2}/V_{AO2\,Ref}$) stops changing with quencher concentration (illustrated later in **Figure 4.7**).[106] Since none of the reports analyzing the efficiency of the Imd/RNO method for $^1O_2$ determinations include determinations in microheterogeneous media, it is not clear that the method can be efficiently used to determine relative quantum yields by comparing sensor disappearance rates in aqueous and microheterogeneous or non-aqueous solvents.

The aim of this report is to examine the Imd/RNO method efficiency and reliability for relative sensitizer $^1O_2$ quantum yield determinations by simultaneously monitoring the rates of sensor bleaching and sensitizer degradation induced by simulated sunlight in several solvents. The performance of the method in the original assay solvent, pH 7.4 PB, was compared to its efficiency in common $^1O_2$ quantum yield reference solvents, methanol (MeOH) and ethanol (EtOH). Microheterogeneous solvents, 5% sodium dodecyl sulfate (SDS), octanol (OctOH) and pH 7.4 phosphate buffer saturated octanol (PBOctOH), were selected for their biomimetic and geomimetic properties. For example, octanol-water partition coefficients are commonly used to predict the pharmacokinetic characteristics of drug compounds and the toxicity and transport of pollutants in soil and groundwater systems.[27] Octanol was also selected for its structural microheterogeneity,[27,28] i.e. its capacity to self-assemble into predominantly hydrophilic and hydrophobic regions, like the aqueous micellar solution, SDS, to some extent. The impact of this feature on the method was investigated using

pH 7.4 phosphate buffer saturated octanol (PBOctOH), which is approximately 26% aqueous buffer by volume.[28]

4.3 Materials & Methods

4.3.1 Materials

Rose Bengal (RB, Aldrich Chem. Co.), p-nitrosodimethylaniline (RNO, Acros Organics), imidazole (Imd, Fisher Scientific), sodium lauryl (dodecyl) sulfate (Fisher Scientific), octanol (OctOH, 99% pure, Acros Organics), methanol (MeOH, HPLC grade Fisher Chemical), ethanol (EtOH, Decon Laboratories, Inc.), and HPLC-grade lab water (HOH, Fisher Chemical) were purchased and used as received. Phosphate buffer was prepared by combining 1.0 M sodium phosphate dibasic (Na_2HPO_4, Fisher Scientific) and 1.0 M sodium phosphate monobasic (NaH_2PO_4, Fisher Scientific) in a 7.74:2.26 volume ratio, then diluted with HOH; resulting in a buffer salt concentration of 0.01 M, and pH of approximately 7.4 (as measured by glass electrode). Sodium dodecyl sulfate 5% micellar solution (SDS) was prepared by dissolving 25 grams of sodium lauryl (dodecyl) sulfate into 500 mL HPLC grade water. Phosphate buffer saturated octanol (PBOctOH) was prepared by combining an equal volume ratio of PB and OctOH, vigorously stirring on an electronic stir box for approximately 4–6 hours, and then allowing the mixture to rest for at least 72 hours before removing the organic layer for use.

Stocks of RB and RNO were prepared by solvation in EtOH to obtain stock concentrations of approximately 5 mM and 1 mM, respectively. Imd was prepared in each of the six assay solvents at a concentration of 5 mM – 1.5 M to achieve a broad range of concentrations. All stock solutions were wrapped in tin foil, refrigerated, and

monitored by UV–Vis absorption spectroscopy for signs of decay or contamination, and discarded if their peak absorption decreased by more than 5%.

4.3.2 Molar Absorptivities

Molar absorptivities were obtained using solutions that have exponentially increasing concentrations, in a single cuvette. Starting with 1.8–2.0 mL of solvent in a 3.5 mL quartz cuvette, µL additions of chromophore stock solution were added to the cuvette, and spectra collected by a diode array spectrophotometer (HP, 8452A). Molar absorptivities were, at minimum, completed in duplicates, with at least one trail wherein the spectrometer was calibrated with an air blank (empty cuvette), and one with a solvent blank (cuvette filled with solvent). Absorption spectra were then used to construct a Beer's Law plot of absorbance versus concentration, and the molar absorptivity computed from the slope of the linear line of best fit at each measured wavelength.

4.3.3 Imd Plus RNO Assays

The apparent rate of $^1O_2$ production was determined by monitoring the bleaching of the sensor, RNO, over time. Solutions of 5.0 mL were prepared in volumetric glassware with an RB and RNO final concentration of 10 µM and 50 µM, respectively, while Imd was varied logarithmically between 50 µM–0.5 M. Assays and a series of controls were conducted in each solvent, in at least triplicate and duplicate, respectively.

A 300 W xenon arc lamp (ILC Technologies, R300-3) was used to irradiate samples with simulated sunlight, as shown previously in **Figure 2.3**. Following the lamp, an 18 cm temperature-controlled water column fitted with quartz lenses was used to collimate the incident light and filter out a majority of the IR irradiation. A chemical

actinometer, Trioxalate Fe(III) complex (FeOx), in which Fe(III) is reduced to Fe(II) and quantified colorimetrically by complexation with 1,10–phenanthroline (described previously in **Chapter 2**), was used to determine the affective irradiance at the surface of the quartz cuvette. The irradiance was determined to be 41.17 mW/cm^2 (411.7 W/m^2, 0.30 suns).

For photooxidation studies and control measurements, 3.0 mL of the prepared solution was placed into a 10 mm pathlength quartz cuvette (FireflySci), placed on a magnetic stir plate, and irradiated. All UV–Vis assay and control spectra were collected by a diode array spectrophotometer (HP, 8452A) calibrated with an air blank. Measurements were collected every 3 seconds to 5 minutes, depending on the rate of RNO bleaching, for fifteen consecutive measurements (beginning with time "0") by manually shielding the sample with a metal plate, moving the sample cuvette to the UV–Vis sample chamber for measurement, then returning the sample to the stir box and removing the shield for further irradiation. To avoid the accumulation and potential interference from secondary products, the sensor bleaching was capped to no more than a 15% reduction of the initial absorbance at the sensor's wavelength of maximum absorbance.

4.3.4 Data Analysis

The time-resolved, UV–Vis diode array absorbance data, collected as the progress of Imd/RNO $^1O_2$ assays was monitored, were analyzed to assess the efficiency of the assay in the selected solvents. Zero order rate constants (k_0) of the sensor bleaching and sensitizer photodegradation reactions were calculated as usual, i.e., from the best linear fit of the concentration time dependence at the species wavelength of maximum absorbance.

4.4 Results & Discussion

The efficiency of the Imd/RNO method in reference alcohols and selected microheterogeneous solvents was compared to its efficiency in PB, the solvent originally used by the method creators, Kraljić and El Mohsni. The efficiency was measured using the apparent production of $^1O_2$ indicated by RNO bleaching induced by the model photosensitizer, RB. Sensor bleaching and sensitizer photodegradation were monitored simultaneously using time-resolved, broadband UV–Vis absorbance measurements of solutions containing RB, RNO, and Imd subjected to simulated solar irradiation. Molar absorptivities at the maximum absorbance wavelengths (λ_{max}) for RNO and RB, reported in Table **4.1**, were used to convert measured absorbances to concentrations, which were used to determine zero order rate constants (k_0). In addition to monitoring the dependence of sensor bleaching on the Imd concentration, the method suggested by Gottschalk[106] was used to determine relative $^1O_2$ production quantum yields (ϕ_Δ) for RB in PB, SDS, EtOH, OctOH, and PBOctOH using the reported RB ϕ_Δ in MeOH as the reference.

4.4.1 Sensor & Sensitizer Absorbance Properties

The data in **Table 4.1** shows an interesting contrast in the behavior of RNO and RB in the pure solvents. The sensor, RNO, is generally positively solvatochromic, i.e., as solvent polarity increases there is a bathochromic (red) λ_{max} shift. Moreover, the sensor band exhibits a hypochromic shift, decreasing in absorptivity (ε) by approximately 14% as the dielectric constant (ε_r) increases from 10 in octanol to 80 in phosphate buffer. Conversely, the sensitizer, RB, is negatively solvatochromic, exhibiting a hypsochromic (blue) λ_{max} shift as the solvent polarity increases. The main sensitizer band also exhibits a hypochromic shift of approximately -10% over the 8-fold

increase in solvent ε_r. These data indicate that RNO is stabilized in more polar solvents as RB is stabilized in more nonpolar solvents, and are consistent with the difference in the size and functionalization of the two molecules.

Since the solvatochromism of both absorbance maxima correlate well with the relative permittivities of the pure solvents, the absorbance maxima of RNO and RB in the micellar solution (SDS) and buffer saturated octanol (PBOctOH) can be correlated to the polarity of the solvent environment around each solute. In SDS, RNO senses an environment similar to water (ε_r = 80) while the RB spectrum indicates a less polar environment similar to methanol (ε_r = 33). This is consistent with previous reports of RB interaction with SDS micelles without functionalization to remove electrostatic repulsion.[24] Since the absorptivity of RNO is substantially higher in SDS than in water, and more similar to that in the isotropic alcohols, the data suggest that RNO is solvated within the micelle, exposed to a less polar environment. A similar argument applies to the RB data.

In PBOctOH, RNO senses an environment similar to 1-propanol (ε_r = 21.5) while the RB spectrum indicates a slightly less polar environment similar to 2-butanol (ε_r = 17.4). This difference is not dramatic enough to indicate RNO in buffered water pools surrounded by non-polar octanol chains solvating RB, but is consistent with some affinity of each molecule for a compatible environment in the interfacial structure of the solvent. This is also consistent with the observation that the molar absorptivities of both compounds in PBOctOH are substantially smaller than simple solvent mixing would predict, suggesting that both molecules experience greater intermolecular association at the interface of the mixed solvent than in either pure counterpart.[107]

Table 4.1: Absorbance properties of RNO and RB observed in selected solvents.

		RNO		RB	
Solvent	**ε_r**	**λ_{max} (nm)**	**ε (M^{-1}•cm^{-1})**	**λ_{max} (nm)**	**ε (M^{-1}•cm^{-1})**
PB	~80	440	20780 ± 9	550	90000 ± 5000
SDS	~32	440	23400 ± 800	558	97000 ± 5000
MeOH	33	426	23590 ± 50	558	97000 ± 5000
EtOH	25	422	24860 ± 20	560	86000 ± 9000
PBOctOH	-	422	12100 ± 60	564	82000 ± 2000
OctOH	10	418	24000 ± 1000	564	102000 ± 8000

Dielectric constants (ε_r) were obtained from reference Maryott 1951 [91]
‡ Buffer solution ε_r estimated to be similar to that of pure water.
† SDS ε_r obtained from Chaudhuri 2009 [92]

4.4.2 Sensor & Sensitizer Kinetic Rates During Assay Measurements

Plots of the dependence of the sensor zero order bleaching rate constants (k_0) on the acceptor, Imd, concentration are shown in **Figure 4.3A** for each solvent studied. In previous reports,[62,71,105] a maximum in the dependence of sensor bleaching on the concentration of acceptor was observed between 3–10 mM in aqueous PB. **Figure 4.3A** shows a similar dependence of sensor bleaching in aqueous PB on the acceptor concentration, peaking in the millimolar concentration range, with a rate of 890 ± 50 nM/s. In SDS, two maxima in the dependence of sensor bleaching on the acceptor concentration was observed near 500 μM and 50 mM in aqueous SDS micellar solution, with rate constants of 50 ± 1.3 nM/s and 49 ± 1.4 nM/s, respectively. On the other hand, the sensor bleaching rate increased monotonically with acceptor concentration in the alcohols, including PBOctOH, without a plateau or peak below the maximum measured acceptor concentration. It is noteworthy that the peak sensor bleaching rates in the alcohols and micellar solution were much slower, exhibiting rates less than 30% of the peak rate in PB; note that the PB sensors bleaching rates in **Figure 4.3A** were reduced to ¼ their value to enhance figure resolution. This difference in dependence on the acceptor concentration suggests that the mechanism of acceptor sensor bleaching in

aqueous solvents could be different from the mechanism in the alcohols used in this study. Mechanistic differences could present challenges to measurements of relative $^1O_2$ production rates or quantum yields of sensitizers in varying media made using the Imd/RNO method.

In an effort to contextualize the unexpected differences in the dependence of sensor bleaching rates on the acceptor concentration in the comparison solvents, the dependence of sensitizer zero order photodegradation rate constants, which were acquired in the same measurement as the sensor bleaching data, were computed and plotted in **Figure 4.3B**. Not only is the dependence of sensitizer photodegradation rates on the acceptor concentration quite different from that of the sensor rate in every solvent, but the difference in the sensitizer disappearance rate dependence on acceptor concentration across the solvents supports the idea that assay reactions in each solvent may follow different mechanisms. In PB, the sensitizer photodegradation rate is highest at lower acceptor concentrations (<5 mM) and falls to very low rates at acceptor concentrations (> 5 mM). In most of the alcohols, the sensitizer disappearance rates tend to increase with acceptor concentration, but fall above 50 mM. Though, the rates barely change in MeOH and change most dramatically in EtOH. The data presented in **Figure 4.3B** also show that the polarity dependence of the sensitizer photodegradation rates shift in the mM acceptor range. At low acceptor concentration (50 μM), sensitizer photodegradation rates generally increase with increasing solvent polarity and the rates in aqueous solvents are roughly twice the rates in alcohols. Near the high end of the range (50 mM), the polarity dependence of sensitizer photodegradation rates is reversed, generally decreasing with increasing solvent polarity. Moreover, the rates in the alcohols in the higher acceptor range are several times larger than the rates in aqueous

solvents. These sensitizer result, paired with the previously described sensor results suggest variations in the Imd/RNO method performance across the various solvents studied.

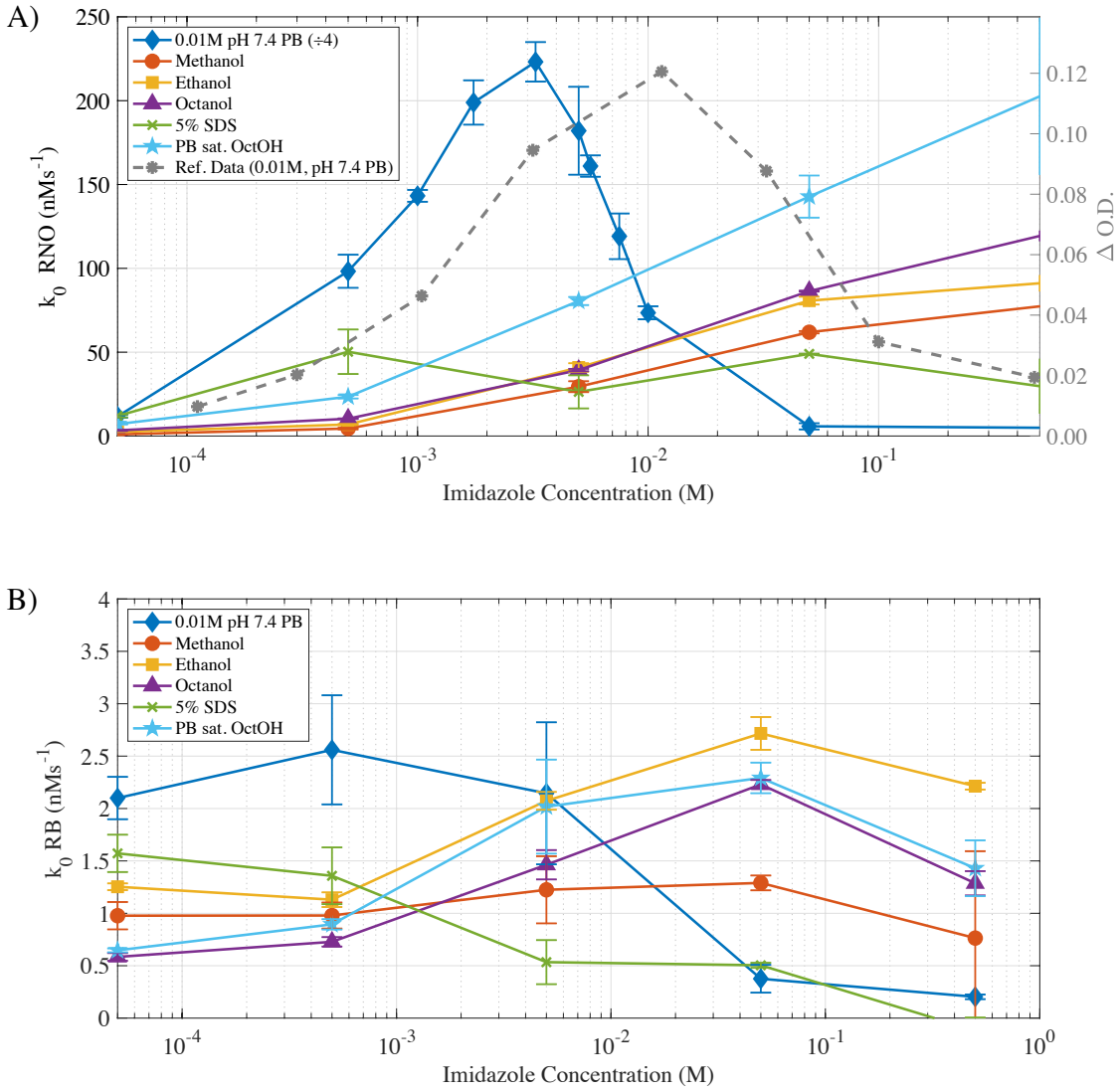

Figure 4.3: Comparison of zero order photobleaching rate constants of A) RNO and B) RB at various Imd concentrations as a result of RB photosensitization and subsequent $^1O_2$ production. In the right axis of panel A, reference data[62] is included for comparison. Reaction: [RB] = 10 μM, [RNO] = 50 μM, [Imd] = 50 μM - 500 mM. RNO bleaching rates in PB were reduced to ¼ to enhance figure details. Uncertainties represent 1 standard deviation from the mean. N ≥ 3.

4.4.3 Sensor & Sensitizer Kinetic Rates During Control Measurements

In the original paper, Kraljić and El Mohsni used controls to isolate the sensor response to $^1O_2$ generated by the sensitizer. In this study, their controls were replicated and expanded in each solvent studied. For consistency, each control is designated by the component accompanying the sensor in the measurement. For example, controls containing RNO alone are described as blanks, while those containing Imd and RNO described as acceptor controls. Measurements containing all three components described as assays. In the terminology of Kraljić & El Mohsni, the bleaching controls without the acceptor, i.e., blanks and sensitizer controls, are considered primary bleaching controls—in which the sensor is bleached directly by the sensitizer or $^1O_2$. As **Figures 4.4** shows, the primary bleaching controls tested by Kraljić and El Mohsni were augmented by low and high concentration acceptor controls. In addition, similar controls for the sensitizer were performed and presented in **Figure 4.5**.

Based on the reaction mechanism cited by Kraljić and El Mohsni, the response of the acceptor controls for RNO bleaching are expected to be comparable to the blanks as little to no transannular peroxide is expected to form in the absence of a $^1O_2$ source. On the other hand, some increase in the bleaching rate is expected in sensitizer controls, because even in the absence of the acceptor, some $^1O_2$–sensor collisions could be expected to produce primary bleaching. As **Figure 4.4** illustrates, RNO bleaching rates rarely respond as expected, even in PB, the original solvent. The data show that bleaching rates in the blank and acceptor controls show a strong dependence on the solvent polarity, with the dramatic exception of rates in PBOctOH. The rate of the sensor blank increases to nearly 4x as the dielectric constant drops from 80 in PB to 10 in OctOH. The unusually high bleaching rates observed in PBOctOH controls and assays are surprising, and may reflect a greater degree of intermolecular association between

the assay components at the interfaces of the mixed solvent—as suggested by the previous molar absorptivity data. The data in **Figure 4.4** also show that the increase expected in sensitizer controls is only observed in the aqueous solvents, PB and SDS, and EtOH. Though the remaining solvents, the range of measurement error is too close to conclude either an increase or decrease between the blank and sensitizer control.

In PB, sensor bleaching rates lower than the blank control were observed in the acceptor controls: adding a low concentration of acceptor to the sensor produced a substantial decrease (~80%) in the sensor irradiation bleaching rate. An even greater impact (~95% reduction) was observed at higher acceptor concentration. The explanation for this decrease is unclear. If the spectra of the sensor and acceptor overlapped, the rate decrease on acceptor addition could be interpreted as a result of acceptor absorbance. It suffices to note that lower bleaching rates in the presence of acceptor alone do not undermine assay performance and may promote higher assay response and sensitivity. Bleaching rates in the PB sensitizer control conform to expectations: the control rate is roughly 8x larger than the blank rate. As the assay data in **Figure 4.3** indicate, combining the acceptor and sensitizer amplifies the sensor response substantially, even at low acceptor concentration.

SDS is the only solvent other than PB, in which the sensitizer control shows a sensor bleaching rate increase relative to the blank. However, SDS acceptor bleaching controls were somewhat larger than the blank rates, rather than equal as expected or smaller as in PB. In these controls, the sensor bleaching increased (~50%) with addition of 50 μM acceptor, and even more (~200%) with addition of 50 mM acceptor. Though the rates of these controls are minimal (<2%) relative to the bleaching rates observed during $^1O_2$ assays at peak acceptor concentration, they indicate that caution should be

used when performing the Imd/RNO assay in aqueous micellar solutions using low acceptor concentrations, as appreciable sensor bleaching may be due to the acceptor alone.

In the alcohols, the expected similarity between the blanks and accepter controls was usually not observed. In fact, the high concentration acceptor control rates are larger than the blanks in all the pure alcohols. As noted, generally none of the sensitizer controls conducted in alcohols produced an appreciable increase in bleaching rate, with the sole exception of EtOH, though the increase was relatively minimal in comparison to that observed in the aqueous solvents. The lack of increase in the sensitizer control in alcohols may reflect reactions that compete with sensor bleaching, given that $^1O_2$ lifetimes are longer in MeOH and EtOH than in water (measured directly at 1270 nm).[108] As in the aqueous solvents, the rates of primary bleaching observed in the sensitizer controls are substantially smaller (<2%), than the maximum bleaching rates observed in the alcohol assays at high acceptor concentration. However, when the sensitizer control is compared to assays at low acceptor concentrations, direct bleaching is particularly significant (~45–75%), reinforcing the importance of finding an optimal acceptor concentration for the solvent, which, again, may differ between solvent conditions.

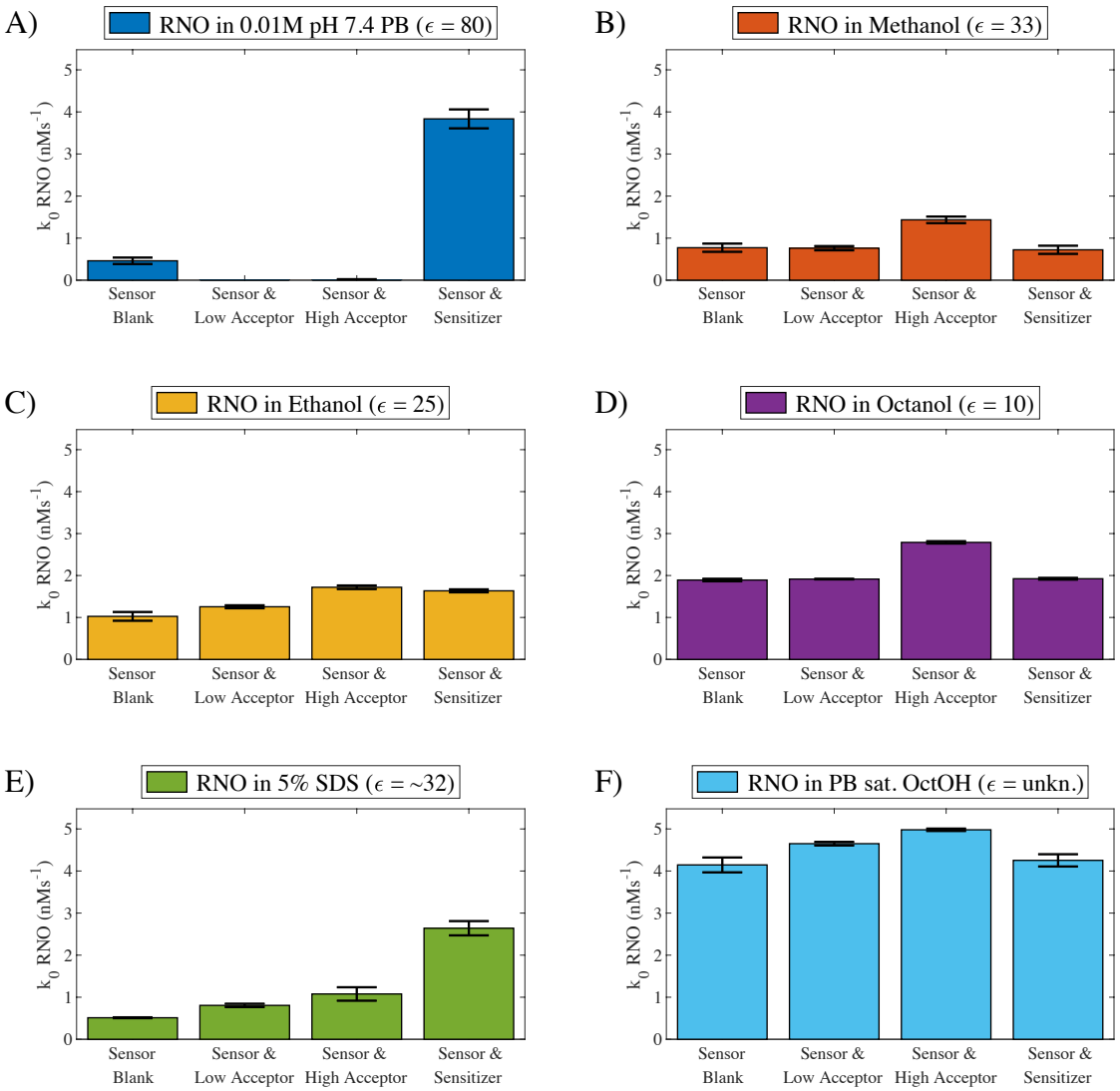

Figure 4.4: Comparison of zero order photobleaching rate constants of the sensor (RNO) during control measurements of the Imd/RNO method. Solvent dielectric constants (ϵ_r) are listed in legend when available. Reaction conditions: [RB] = 10 μM, [RNO] = 50 μM, $[Imd]_{low}$ = 50 μM, $[Imd]_{high}$ = 50 mM. Uncertainties represent 1 standard deviation from the mean. N ≥ 2.

Control measurements for the sensitizer photodegradation were conducted in a similar fashion to the sensor controls and are illustrated in **Figure 4.5**. Here, in analogy to the sensor bleaching controls, each sensitizer photodegradation control is labeled by

the component that accompanies the sensitizer in the measurement. Following the mechanism adopted by Kraljić and El Mohsni, it is expected that the blank control would exhibit the highest photodegradation rate. In the presence of $^1O_2$ quenchers, like Imd and RNO, the excited triplet sensitizer should relax to the ground state, intact and unbleached at a higher rate. Therefore, the acceptor and sensor controls, illustrated in **Figure 4.5**, are expected to show slower sensitizer photodegradation compared to the blank.

The sensitizer controls for PB generally follow the implications of the accepted mechanism. Adding sensor or high acceptor to the sensitizer lowered sensitizer photodegradation rates, likely reflecting an effective transfer of energy from $^1O_2$ to the sensor. In addition, across the controls and assays in PB, as acceptor concentration increases sensitizer photodegradation decreases, as expected if the acceptor efficiently captures $^1O_2$. When the acceptor concentration is above the optimal value (5 mM in PB), sensitizer photodegradation is reduced to ~32% of the rate observed in the blank, apparently as a result of $^1O_2$ capture. These observations reinforce the critical nature of optimal acceptor concentration on the efficiency of the Imd/RNO method and illustrate the correlation between lowered sensitizer photodegradation rates and method efficiency.

In the comparison solvents, sensitizer sensor controls (sensitizer photodegradation with the sensor, without the acceptor) exhibited behavior similar to the sensor control in PB. Adding the sensor to the sensitizer lowered the photodegradation rates, as expected. However, in EtOH, the change is small and may be negligible. In contrast to PB and mechanism-based predictions, acceptor controls at both levels in the remaining solvents generally showed increases in sensitizer

photodegradation of various proportions, with the high acceptor controls exhibiting significant increases. In MeOH and SDS the increases in the high acceptor controls were the lowest at ~280% and ~488%, respectively, while OctOH and PBOctOH had the greatest increases of ~1400% and ~1500%, respectively. Even the low acceptor controls produced sensitizer degradation rates that were double the size of the blanks in most solvents. The reversal of the polarity dependence observed in the assays (**Figure 4.3**) is also observed in these controls; however, the atypically high rates observed in the high acceptor controls in SDS and EtOH require additional study. The source of this unexpected behavior of the sensitizer in the presence of the acceptor may be radical formation through reaction of the excited triplet sensitizer and Imd.[109] The observation of unanticipated reactions rapid enough to mask or undermine the $^1O_2$ capture function of the acceptor for a productive model sensitizer, like RB, indicates that caution is warranted when comparing assay rates without controls.

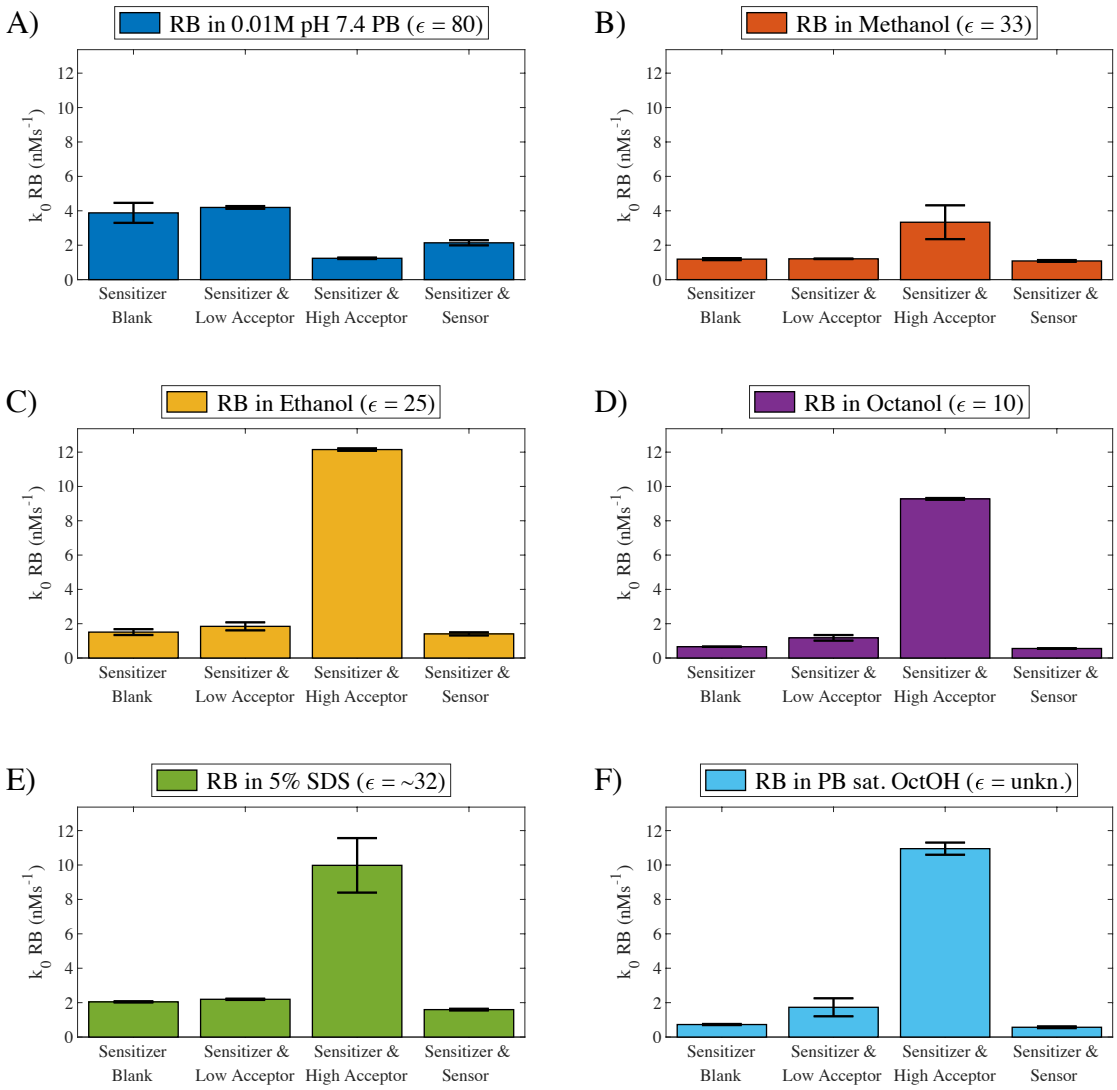

Figure 4.5: Comparison of zero order photobleaching rate constants of the sensitizer (RB) during control measurements of the Imd/RNO method. Solvent dielectric constants (ϵ_r) are listed in legend when available. Reaction conditions: [RB] = 10 μM, [RNO] = 50 μM, $[Imd]_{low}$ = 50 μM, $[Imd]_{high}$ = 50 mM. Uncertainties represent 1 standard deviation from the mean. N ≥ 2.

Taken together, the differences in RNO bleaching rate dependence on the Imd concentration in the aqueous and non-aqueous solvents (**Figure 4.3A**), reversal in the polarity dependence of the sensitizer photodegradation with increasing Imd

concentration in the presence or absence of the sensor (**Figures 4.3B & 4.5**), absence of direct sensor response to sensitizer in non-aqueous solvents (**Figure 4.5**) suggests that the mechanism of the bleaching of RNO by Imd or the nature of competing reactions in PB is different from that in the alcohols. Additional evidence of a mechanistic change with Imd concentration is observed in the kinetic profile of the sensitizer as the Imd concentration is increased from zero, to low (50 μM) and high (50 mM) Imd. In PB, not only is the rate of sensitizer degradation reduced, as expected for increasing $^1O_2$ trapping, the RB kinetic profile was observed as zero order at all three Imd concentration levels. In contrast, the rate of sensitizer degradation in the alcohols not only is increased dramatically with increased Imd concentration, but the kinetic profiles are observed as first, not zero, order.

In light of the potential for the model photosensitizer, RB, to produce ROS other than $^1O_2$, like superoxide ($O_2^{\bullet-}$) as illustrated in **Figure** Error! Reference source not found., that could result in non–ideal bleaching of the sensor, the well–known $^1O_2$ scavenger 1,4 diazabicyclo [2.2.2] octane (DABCO) was used to investigate the sensors selectivity—as was done in several previous studies utilizing the Imd/RNO method.[63,69,71] DABCO has a comparable rate constant with $^1O_2$ as Imd, and therefore should compete equally, and irreversibly, for any dissolved $^1O_2$ in the assay solution. If the sensor is being bleached as a result of $^1O_2$ alone, the equal competition between the sensor and DABCO for $^1O_2$ molecules should result in a ~50% reduction of the sensor bleaching rate when DABCO is used in an equal concentration to the sensor.[71] This selectivity control was performed in three of the solvents, PB, SDS, and PBOctOH, at the low and high acceptor points used in previous controls.

As the results in **Figure 4.6** illustrate, generally DABCO does not reduce the sensor bleaching rate by the anticipated ~50% when compared to the original assay in each of the solvents. In PB, there was an increase in the sensor bleaching of roughly three–fold between the low acceptor/quencher control and original assay. However, at high acceptor/quencher concentration the sensor bleaching rate dropped to ~8% in comparison to the original assay. These results could suggest that in PB the sensor bleaching could be a result of concomitants, in addition to the expected $^1O_2$. Though the trend, like many others in this report, are inconsistent at low and high acceptor concentrations, and may be a reflection of DABCO exhibiting non–ideal mechanisms rather than poor selectivity of the sensor.

In contrast to PB, the quencher control in SDS did produce a ~56% reduction in the sensor bleaching rate when compared to the original assay at low acceptor/quencher concentration. However, at high acceptor/quencher concentration, the sensor bleaching rate increased, and a broader error was observed in both the control and original assay. These results are interesting in the fact that they are in contrast to those in PB. During the assay measurements (**Figure 4.3**) SDS and PB exhibited similar trends in sensor bleaching dependence on acceptor concentration. Again, the abnormal increase in sensor bleaching as a result of DABCO addition may suggest non–ideal reactions between the sensor and quencher.

The quencher control results were closest to ideal expectations in PBOctOH. Roughly a 73% and 54% reduction in the sensor bleaching was observed for the low and high quencher controls, respectively, when compared to their original assay counterparts. These results suggest that the Imd/RNO method is selective towards $^1O_2$ in PBOctOH, though caution is still warranted given the previously presented controls.

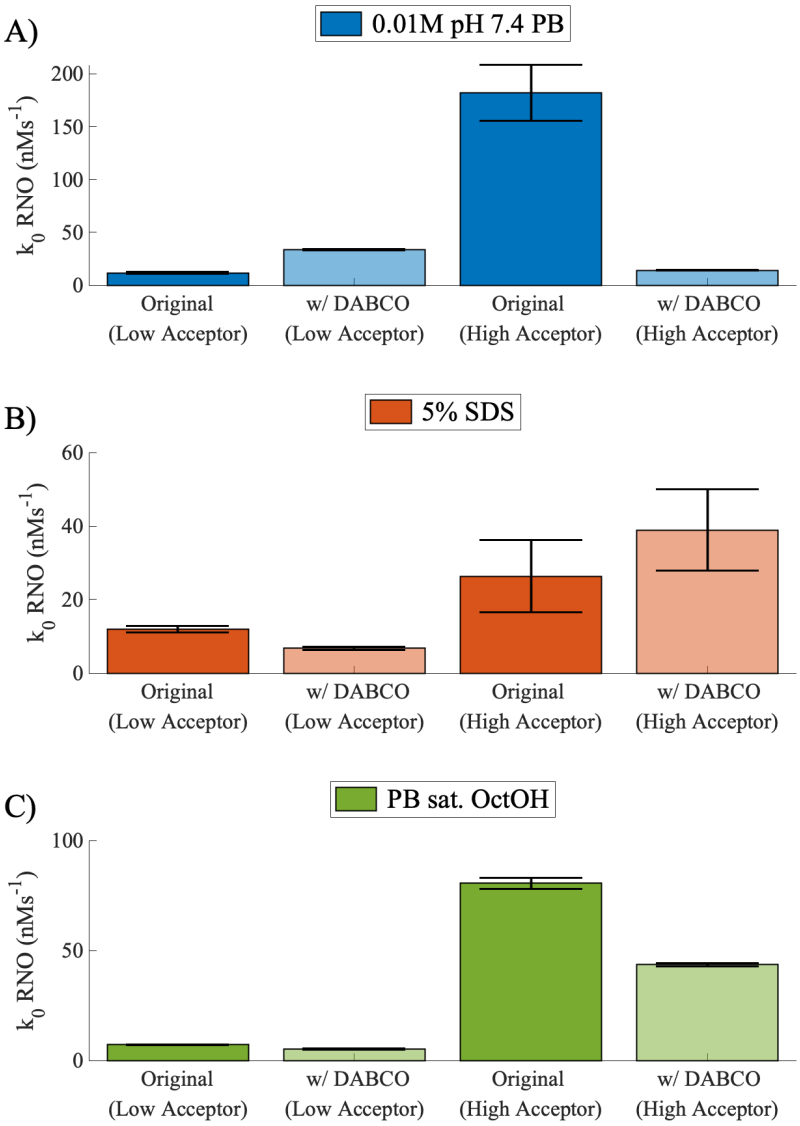

Figure 4.6: Comparison of the zero order photobleaching rate constants of the sensor (RNO) during quencher control measurements in comparison to original assay measurements of the Imd/RNO method. Reaction conditions: [RB] = 10 µM, [RNO] = 50 µM, $[Imd]_{low}$ = 50 µM, $[Imd]_{high}$ = 50 mM, $[DABCO]_{low}$ = 50 µM, $[DABCO]_{high}$ = 50 mM. Uncertainties represent 1 standard deviation from the mean. $N \geq 2$.

4.4.4 Sensitizer Relative Quantum Yield Determinations

In spite of concern that the aforementioned mechanistic differences could undermine the calculation, relative $^1O_2$ quantum yields (ϕ_Δ) for RB in the solvents studied were computed from the sensor zero order bleaching rate constants, using the relative kinetic method described by Gottschalk.[106] The method bases the relative ϕ_Δ on the ratio of a $^1O_2$ quenching rate (V_{AO_2}, the rate of RNO bleaching) in a new solvent to the rate in the reference solvent (MeOH) when the concentration of acceptor (Imd) is above a critical concentration. The critical Imd concentrations in this work were 5 mM in the alcohols and 50 mM in the aqueous solvents, as indicated by stabilization of the bleaching rate ratios with increasing Imd concentration (**Figure 4.7**). The experimental ϕ_Δ values in PB (0.06 ± 0.02) and EtOH (0.99 ± 0.07) do not agree with the reported values of 0.76, and 0.80, respectively, reported by Wilkinson et al.[24] To our knowledge, quantum yields for $^1O_2$ production in SDS, OctOH, or buffer saturated OctOH have not been reported, however ϕ_Δ larger than 1.0 are not expected for the sensitizer. **Figure 4.7** illustrates the dependence of the calculated ϕ_Δ on Imd concentration in the five solvents. Since the ϕ_Δ is determined by the ratio of $^1O_2$ production in the new solvent to production in the reference solvent, the validity of the calculated ϕ_Δ depends greatly on mechanistic parity between the assay reactions in the two media. Even when PB, the original solvent used by Kraljić and El Mohsni, was set as the reference, the relative ϕ_Δ results do not improve. These results illustrate that validating consistent behavior between the $^1O_2$ assay systems is critical to measuring reliable relative sensitizer quantum yields.

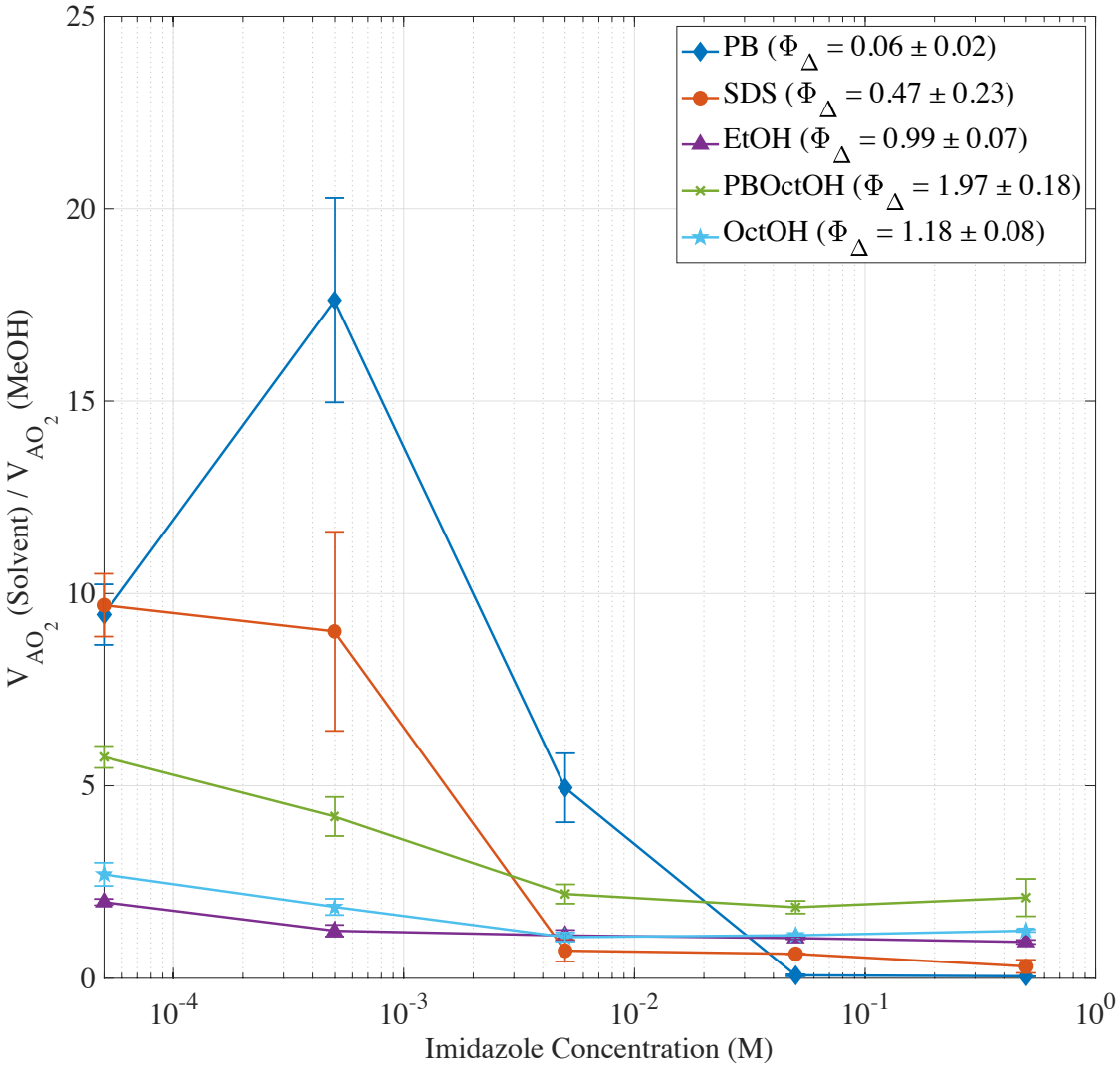

Figure 4.7: Relative $^1O_2$ production rates from RB photooxidation determined by the relative bleaching rates of $^1O_2$ sensor (V_{AO_2}) in PB (blue, ◊), SDS (orange, ●), EtOH (purple, Δ), PBOctOH (green, ×), and OctOH (light blue, ★) to the rates in MeOH. Uncertainties represent 1 standard deviation from the mean.

4.5 Conclusions

In this report, the efficiency of the imidazole plus RNO (Imd/RNO) method for monitoring the production of singlet oxygen ($^1O_2$) was compared in several solvents using time-resolved, broadband UV–Vis absorbance measurements. The bleaching of

the sensor, RNO, and photodegradation of the sensitizer, RB, were simultaneously monitored in PB, the solvent used by the methods creators, Kraljić and El Mohsni, then compared to the performance in reference solvents, EtOH and MeOH, and biorelevant solvents, SDS, OctOH, and PBOctOH. The expected dependence of sensor bleaching and sensitizer photodegradation on the $^1O_2$ acceptor, Imd, concentration was observed in PB, with maximum sensor bleaching rates in the millimolar range. The change in bleaching and acceptor rates with the addition of the reagents in control measurements in PB were consistent with the mechanism proposed for the method. However, that series of control and assay measurements in the comparison solvents indicate discrepancies from the expected mechanism that may undermine the assay in non–aqueous solvents and certainly preclude using the assay in alcohols as references in relative $^1O_2$ determinations. The unexpected response to controls in all the microheterogeneous solvents, including aqueous SDS, suggest that caution is warranted and adequate controls are advised when using the assay to investigate nanostructured systems.

Calculating relative quantum yields using the sensor bleaching rates across solvent types produced untenable results, even when care was taken to conduct assays above the critical acceptor concentration in each solvent. These results reinforce the conclusion that the reactions comprising the Imd/RNO method exhibit inconsistent solvent dependences that complicate comparisons of sensitized ROS production in different media. For relative ROS sensor methods and quantum yield determinations to be reliable, they require the sensitization, $^1O_2$ capture, and subsequent sensor reaction to proceed without significant changes in mechanism in the new environment. The solvent–dependent differences in the performance of the Imd/RNO method reported

here indicate that caution is warranted and confirmatory controls are advised when using the Imd/RNO assay in any solvent other than PB. They also raise questions about the robustness of the method in complex samples that contain cells, biological tissues, or nanoparticles. These observations also underscore the importance of using appropriate controls in ROS detection measurements beyond the specific method used in this study, as the sensors and systems under investigation become increasingly complex.

Chapter 5

TOWARDS RESOLVED ROS SENSOR EVALUATION USING BROADBAND NUMERICAL ANALYSIS STRATEGIES

5.1 Abstract

Self-modeling curve resolution, implemented using singular value decomposition and non–negative matrix factorization, was used to resolve isolated chromophore spectral and response profiles from colorimetric data collected during Imd/RNO assays performed in phosphate buffer (PB) and sodium dodecyl sulfate (SDS), arranged in matrix format and concatenated to form single matrices that capture the range of responses in each solvent. Spectral isolation was improved through concatenation of a series of calibrations, control, and ROS assay measurements—including molar absorptivities, photodegradation controls, and assay data with varied initial reagent concentration. The resulting resolved response profiles for assay reagents of the Imd plus RNO method were then subjected to kinetic profiling, to compare resolved reaction rate constants to those determined by the traditional, single–wavelength, analysis approach.

The results illustrate the potential for spectral and response resolution of colorimetric data by concatenating data sets collected under varying conditions and subjecting them to numerical analysis techniques. In each of the PB and SDS data sets, nine spectral and response vectors were resolved. In each vector set, eight of the nine vectors were identified as reaction components. The final vector of each set was

resolved as a photoproduct, each illustrating differing spectral and response characteristics.

As was concluded by previous work, the solvent–dependent differences in the performance of the Imd/RNO method continue to indicate that caution is warranted and confirmatory controls are advised when using the assay in any solvent other than PB. Resolving the sensor and sensitizer spectral and response vectors did not have a significant impact on the SDS assay nor controls. On the other hand, significant changes to assay results in PB at low acceptor concentration were observed that may reinforce the validity of the Imd/RNO method for use in aqueous PB. Though spectral and kinetic vectors were resolved during this analysis, spurious correlations between the vectors exist that require additional resolution.

5.2 Introduction

A longstanding interest in reactive oxygen species (ROS) stems from their role in many environmental, biological, clinical, and industrial processes.[16] Molecular spectroscopic methods have largely dominated the field of ROS detection due to its many advantages for real–time, localized, in *situ* analysis, with comparatively modest equipment cost and expertise requirements. This has led to a focus on spectral detection of ROS, and many advances in ROS sensor technologies for spectrophotometric (colorimetric) and luminescence measurements.[15,110,111] Although many advances in ROS sensor technologies for spectrophotometric and luminescence measurements have been made to enhance selectivity and time response in ROS detection, ROS are typically generated and evolve in complex settings, making their detection and quantification challenging. Winterbourn[14] described in 2014 that complete characterization of complex ROS processes requires detection, identification, localization, monitoring, and

quantification; she concluded that these steps are increasingly difficult, particularly in *vivo*. Often, detecting a change in a system's redox status is generally attainable, but accurate quantification is not. Poor selectivity of many classic and novel ROS sensors increases the incidence of overinterpretation of results by the scientific community. Recognizing these limitations in ROS detection and quantification, as a few recent reports have done,[12,13,15–17] is crucial as the field of ROS detection continues forward.

In our previous work (reported in **Chapter 4** of this dissertation),[18] the efficiency of the imidazole plus RNO (Imd/RNO) method, a colorimetric sensor for monitoring the production of singlet oxygen ($^1O_2$), was compared in several solvents using time-resolved, broadband UV–Vis absorbance measurements. Through monitoring the bleaching of the sensor, RNO, and photodegradation of the sensitizer, RB, in reference solvents—PB, EtOH and MeOH—in comparison to biorelevant/complex solvents—SDS, OctOH, and PBOctOH—many discrepancies in the performance of the reaction components were discovered. To summarize, the expected dependence of sensor bleaching and sensitizer photodegradation on the $^1O_2$ acceptor, imidazole (Imd), concentration was observed in PB with maximum sensor bleaching rates in the millimolar range; similar to previous reports.[62,71] In addition, the change in bleaching and acceptor rates with the addition of the reagents in control measurements in PB were consistent with the mechanism proposed for the method. However, that series of control and assay measurements in the comparison solvents indicated discrepancies from the expected mechanism that may undermine the assay in non–aqueous solvents and certainly preclude using the assay in alcohols as references in relative $^1O_2$ determinations—as has often been implemented with the Imd/RNO method.

These previous results raised questions about the robustness of the method in complex samples that contain cells, biological tissues, or nanoparticles. They also underscore the importance of using appropriate controls in ROS detection measurements beyond the specific method used in this study, as the sensors and systems under investigation become increasingly complex. However, these challenges may be mitigated if it were possible to obtain a sensor signal most tightly correlated to the analyte of interest. In other words, the classic methodology for interpreting the correlation between sensor and analyte is by following the sensor appearance or disappearance only at the wavelength of maximum absorbance. This method, relies on the signal at the detector for the single wavelength to change only as a result of the sensor; however, in complex mixtures this may not be the case. Concomitants may exist or form during the progress of the assay that may overlap spectrally with the sensor, weakening the correlation between sensor signal and analyte. Therefore, the research presented here attempts to increase the accuracy of colorimetric data analysis using numerical analysis strategies to isolate or reject overlapping concomitant signals.

It is proposed that self-modeling curve resolution, implemented using singular value decomposition[19] and non–negative matrix factorization,[20] can be used to resolve isolated chromophore spectral and response profiles from colorimetric data resulting from the use of the Imd plus RNO method using numerical analysis strategies. Collecting broadband spectral measurements over time as a response to varying sample or reaction properties generates a matrix of the form $\boldsymbol{A} = \boldsymbol{E}\boldsymbol{C}^T$, where the columns of matrices $\boldsymbol{E}$ and $\boldsymbol{C}$ are the spectra (absorptivities) and response (concentration) profiles of the mixture components, respectively, in adherence with Beer's Law. Matrix formatting of data with variations in conditions increases the selectively of spectral

measurements because matrices are amenable to numerical analyses that have the ability to resolve isolated chromophore spectral and response profiles.

This report describes the resolution of component spectra from matrix-formatted broadband UV–Vis spectra collected during Imd/RNO assays under varying conditions. In this report, the selectivity of the measurement is increased by concatenating each of the original time-dependent assay spectral matrix with assay controls, and reagent calibrations. The concatenated data set, i.e., calibrations, controls, and assay matrices, was analyzed using a variant of the non-negative matrix factorization (NMF) algorithm developed by Lee and Seung.[20] The bands that appear in the component spectra are assigned and their associated time profiles are interpreted in terms of the traditional kinetic profiling in zero order, then compared to those obtained in previous work[18] using raw, single wavelength time–dependent profiles.

5.3 Methods

5.3.1 Materials

Rose Bengal (RB, Aldrich Chem. Co.), p-nitrosodimethylaniline (RNO, Acros Organics), imidazole (Imd, Fisher Scientific), sodium lauryl (dodecyl) sulfate (Fisher Scientific), octanol (OctOH, 99% pure, Acros Organics), methanol (MeOH, HPLC grade Fisher Chemical), ethanol (EtOH, Decon Laboratories, Inc.), and HPLC-grade lab water (HOH, Fisher Chemical) were purchased and used as received. Phosphate buffer was prepared by combining 1.0 M sodium phosphate dibasic (Na_2HPO_4, Fisher Scientific) and 1.0 M sodium phosphate monobasic (NaH_2PO_4, Fisher Scientific) in a 7.74:2.26 volume ratio, then diluted with HOH; resulting in a buffer salt concentration of 0.01 M, and pH of approximately 7.4 (as measured by glass electrode). Sodium

dodecyl sulfate 5% micellar solution (SDS) was prepared by dissolving 25 grams of sodium lauryl (dodecyl) sulfate into 500 mL HPLC grade water. Phosphate buffer saturated octanol (PBOctOH) was prepared by combining an equal volume ratio of PB and OctOH, vigorously stirring on an electronic stir box for approximately 4–6 hours, and then allowing the mixture to rest for at least 72 hours before removing the organic layer for use.

Stocks of RB and RNO were prepared by solvation in EtOH to obtain stock concentrations of approximately 5 mM and 1 mM, respectively. Imd was prepared in each of the six assay solvents at a concentration of 5 mM – 1.5 M to achieve a broad range of concentrations. All stock solutions were wrapped in tin foil, refrigerated, and monitored by UV–Vis absorption spectroscopy for signs of decay or contamination, and discarded if their peak absorption decreased by more than 5%.

5.3.2 Molar Absorptivities

Molar absorptivities were obtained using solutions with increasing concentrations in a single cuvette. Starting with 1.8–2.0 mL of solvent in a 3.5 mL quartz cuvette, μL additions of chromophore stock solution were added to the cuvette, and spectra collected by a diode array spectrophotometer (HP, 8452A). Molar absorptivities were, at minimum, completed in duplicates, with at least one trail wherein the spectrometer was calibrated with an air blank (empty cuvette), and one with a solvent blank (cuvette filled with solvent). Absorption spectra were then used to construct a Beer's Law plot of absorbance versus concentration, and the molar absorptivity computed from the slope of the linear line of best fit at each measured wavelength.

5.3.3 Imd Plus RNO Assays

Solutions of 5.0 mL were prepared in volumetric glassware with an RB and RNO final concentration of 10 μM and 50 μM, respectively, while Imd was varied logarithmically between 50 μM–0.5 M. Assays and a series of controls were conducted in each solvent, in at least triplicate and duplicate, respectively.

A 300 W xenon arc lamp (ILC Technologies, R300-3) was used to irradiate samples with simulated sunlight, as shown in **Figure 2.3**. Following the lamp, an 18 cm temperature-controlled water column fitted with quartz lenses was used to collimate the incident light and filter out a majority of the IR irradiation. A chemical actinometer, Trioxalate Fe(III) complex (FeOx), in which Fe(III) is reduced to Fe(II) and quantified colorimetrically by complexation with 1,10–phenanthroline (described in **Chapter 2**), was used to determine the affective irradiance at the surface of the quartz cuvette. The irradiance was determined to be 41.17 mW/cm^2 (411.7 W/m^2, 0.30 suns).

For photooxidation studies and control measurements, 3.0 mL of the prepared solution was placed into a 10 mm pathlength quartz cuvette (FireflySci), placed on a magnetic stir plate, and irradiated. All UV–Vis assay and control spectra were collected by a diode array spectrophotometer (HP, 8452A) calibrated with an air blank. Measurements were collected every 3 seconds to 5 minutes, depending on the rate of RNO bleaching, for fifteen consecutive measurements (beginning with time "0") by manually shielding the sample with a metal plate, moving the sample cuvette to the UV–Vis sample chamber for measurement, then returning the sample to the stir box and removing the shield for further irradiation. To avoid the accumulation and potential interference from secondary products, the sensor bleaching was capped to no more than a 15% reduction of the initial absorbance at the sensor's wavelength of maximum absorbance.

To investigate the impact of an oxygen–free solution, some controls sample solutions were purged of oxygen (degassed). To do so, the solution was contained in the capped UV quartz cuvette, and two HPLC–type needles (Hamilton) with beveled, curved non–coring points were pierced through the SEPTA of the screw cap. The first needle was 25–gauge and used as a pressure release for the purge gas, and was kept in the cuvette headspace above the solution. The second needle was 20–gauge and fitted to a 5 mm diameter hose connected to a nitrogen tank valve. This needle was pushed through the septum and submerged in the solution, and left to aerate the solution for 30–60 minutes, depending on the solvent. A stir bar and stir plate was also used to mix the solution throughout the degassing process. When a solution like 5% sodium dodecyl sulfate (SDS) was degassed, in which bubbles formed during the degassing process, a third needle, of 20–gauge, was fitted to a second 5 mm diameter hose connected to the same nitrogen tank using a T–shaped connector. This needle was pushed through the septum and kept in the cuvette headspace to suppress any foam that forms at the surface of the solution. Due to the increase in pressure from two gas needles, the 25–gauge pressure release needle was replaced with a 20–gauge needle.

5.3.4 Numerical Analysis

Data collected in 0.01M pH 7.4 phosphate buffer (PB) and sodium dodecyl sulfate (SDS) were subjected to numerical analysis techniques. The spectra collected during Imd/RNO assays in each solvent were arranged in matrix format (wavelength vs reaction time) and subjected to singular value decomposition (SVD)[19] to resolve the spectral and kinetic profiles of distinguishable components contributing to the matrix. Absorbance data matrices for both solvents were formed by concatenating Imd/RNO assays, controls, and reagent calibrations, then factoring them into chromophore spectra

and relative concentration profiles using a variant of the Non-negative Matrix Factorization (NMF) algorithm described by Lee and Seung.[20] The algorithm requires the number of factors contributing to the matrix as an input, so the number of spectrally distinct species was estimated statistically from the SVD results using several methods[39–42] and the consensus was used as the input. The theory underlying the numerical analysis is briefly summarized below for the reader's convenience. The details of the spectral resolution procedures and algorithms are provided in section 2.6.2 of this dissertation.

Since each spectrum in the matrix is the sum of the products of the absorptivities and concentrations of the sample chromophores according to Beer's Law (the pathlength may be ignored when it is the same for all spectra), a matrix of time-resolved absorbance spectra can be factored into a matrix of N chromophore absorptivities and a matrix of N kinetic, i.e., time-dependent concentration, profiles that track the contributions of the chromophores to the spectra in the matrix:

$$\boldsymbol{A} = \boldsymbol{E}\boldsymbol{C}^T \qquad \textbf{5.1}$$

where **A** is an $I \times J$ matrix formed by concatenating absorbance spectra measured at I wavelengths collected at J reaction times, $\boldsymbol{E}$ is an $I \times N$ matrix that has the spectral profiles of the N chromophores along its columns, and $\boldsymbol{C}$ is a $J \times N$ matrix of the kinetic profiles of the N chromophores at the J time measurements.

With all the measurements of the individual chromophore absorptivities at all the I wavelengths obtained, the matrix $\boldsymbol{A}$ is constructed and used, along with self-modeling curve resolution algorithms, to partition (factor) the matrix $\boldsymbol{A}$ into multiples of the chromophore absorptivity spectra and concentration profiles:

$$\boldsymbol{A} = \widehat{\boldsymbol{E}}\widehat{\boldsymbol{C}}^T \qquad \textbf{5.2}$$

where the superposed carat indicates an estimated parameter. The Lee and Seung non-negative matrix factorization (NMF) algorithm[20] used here locates the non-negative matrices $\widehat{\boldsymbol{E}}$ and $\widehat{\boldsymbol{C}}$ that minimize the difference between the data matrix, $\boldsymbol{A}$, and factor product, $\widehat{\boldsymbol{E}}\widehat{\boldsymbol{C}}^{\boldsymbol{T}}$. The variation in the chromophore concentrations during the assays, controls and reagent calibrations facilitates numerical resolution of the spectrally and temporally distinct chromophore responses. When spectra of known components are available, they can be incorporated into the beginning estimate of the NMF algorithm and locked; in this work this is referred to as constrained NMF. During constrained analysis molar absorptivities and photodegradation controls are each subjected to SVD and NMF to resolve isolated reagent spectra that are used to build initial $\widehat{\boldsymbol{E}}$ estimates.

5.3.5 Kinetic Analysis

Once satisfactory factors are determined, the resulting spectra, $\widehat{\boldsymbol{E}}$, and concentration, $\widehat{\boldsymbol{C}}$, profiles are constructed and subjected to kinetic analysis to obtain zero, first, and second order rate law equations, in a similar manner to the traditional kinetic analysis used previously.[18] Rates determined using this approach will only be substantially different from those calculated using the raw absorbance maxima (as was done in the previous work described above) when multiple species contributed to the raw absorbance. It should also be noted that qualitative differences in the kinetics of uncalibrated components can be reliably assess from their resolved profiles.

5.4 Results & Discussion

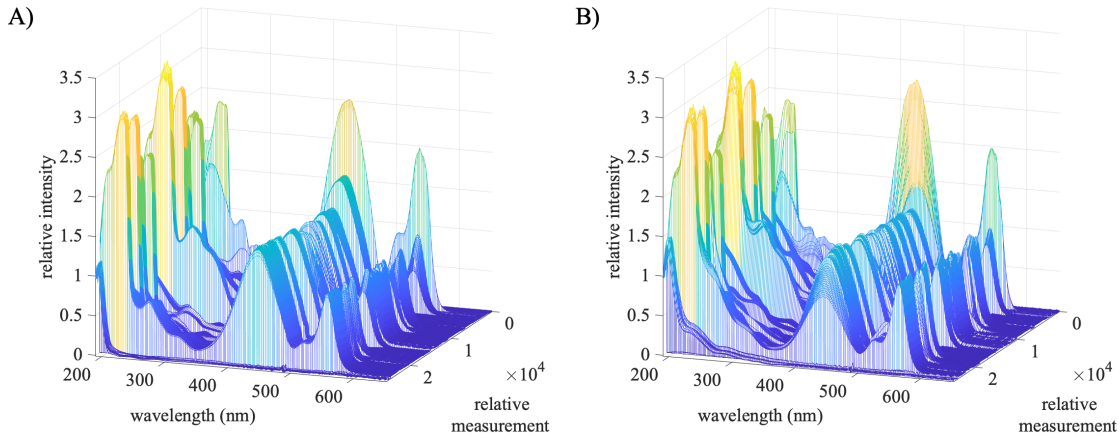

Figure 5.1: Matrix–formatted A) Rose Bengal in 0.01M pH 7.4Phosphate Buffer (RBRNOPB) and B) Rose Bengal in 5% sodium dodecyl sulfate (RBRNOSDS) data sets constructed by concatenating absorbance spectra collected during the singlet oxygen assays, controls and reagent calibrations.

Self-modeling curve resolution, implemented using singular value decomposition[19] and non– negative matrix factorization,[20] was used to resolve isolated chromophore spectral and response profiles from colorimetric data. The data sets collected in the measurements reported here consist of a series of absorbance spectra monitored with respect to time arranged. Series of spectra collected as Rose Bengal sensitized singlet oxygen assays, controls and calibrations were performed in phosphate buffer (PB) and sodium dodecyl sulfate (SDS) were arranged in matrix format and concatenated to form single matrices that capture the range of responses in each solvent. **Figures 5.1A** & **5.1B** depict the data matrices constructed by concatenating spectra collected in 0.01M pH 7.4 phosphate buffer (RBRNOPB) and 5% sodium dodecyl sulfate (RBRNOSDS), respectively. A total of nine factors, i.e., spectral and kinetic profiles, were resolved from each of the data sets, RBRNOPB and RBRNOSDS. Of the

nine spectra depicted in both sets of resolved profiles, eight are recognizable as assay components or reagents, while one component is a suspected photoproduct. The refinement of the spectra from constrained NMF factors for both solvents are described below.

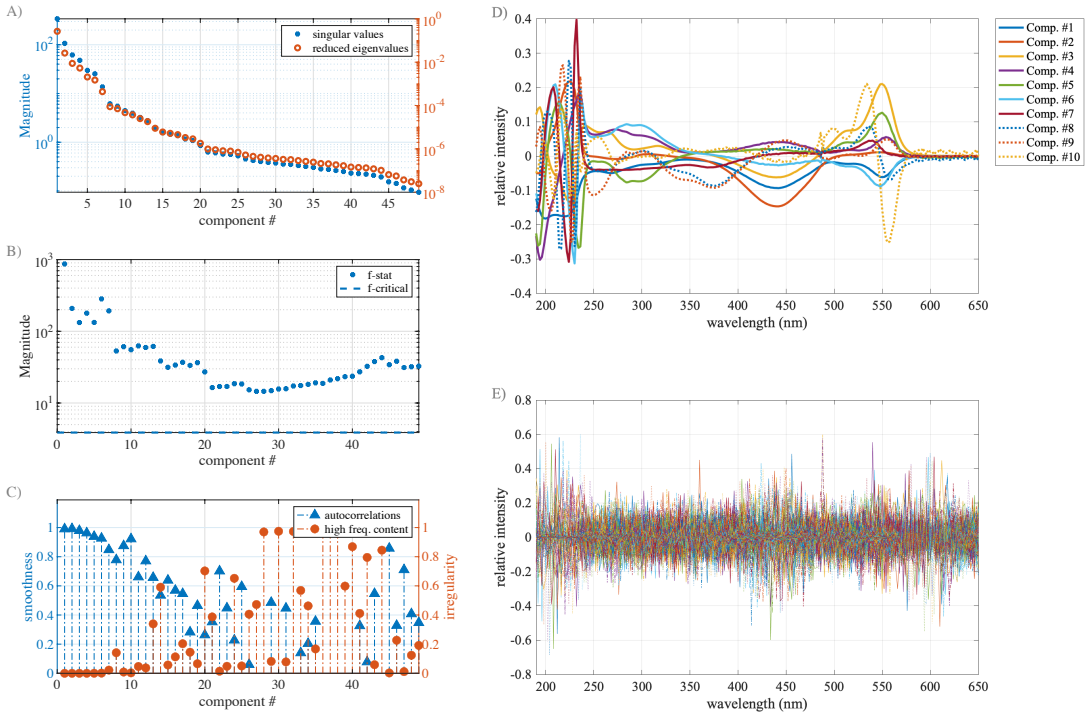

Figure 5.2: Pseudorank estimation of concatenated RBRNOPB data sets. A) Log of singular values and reduced eigenvalues.[43] B) F–test of reduced eigenvalues.[39] C) Column (spectral) singular vector autocorrelations (blue Δ's) and high–frequency content (orange O's).[40,42] D) The first ten column (wavelength) singular vectors; determined as significant. E) The remaining column singular vectors; determined as insignificant.

In PB, pseudorank estimation using SVD (**Figure 5.2**) revealed a likely seven factors, i.e. spectra and response profiles, with factors 8–13 having possible significance. Following SVD analysis, reagent calibrations were subjected individually

to SVD and NMF analysis to compile resolved spectra of isolated reagent profiles. This was done to minimize spurious correlations among spectra of reagents and possible photoproducts during the constrained NMF analysis. As an example, the results of applying the NMF algorithm to sensitizer (RB) calibrations are shown in **Figure 5.3**, in which three factors were identified. The first component is the solvent (blue) that absorbs a dominant band in the near UV. The second factor (yellow) is the expected profile of the pure sensitizer in PB. The third factor (orange) is a result of aggregate formation at high sensitizer concentrations, as is evidenced by the factor's response profile in the basis vector that shows the factor present only at high measurement values (i.e. higher concentrations).

From the individual analysis of reagent calibrations for the sensitizer, sensor (RNO), and acceptor (Imd), a total of nine factors were distinguished. Of the nine factors, one was for the solvent, two for the sensitizer, one for the sensor, and four for the quencher. The acceptor (Imd) spectrum shifts considerably with concentration (discussed previously in section 3.4.3), so that four linear factors are needed to describe its response in both solvents across the range of concentrations used in the assays. The complex nature of the acceptor absorptivity does make resolution in the near UV region of the spectra.

These nine resolved spectral factors were incorporated into the beginning estimate of the constrained analysis of the RBRNOPB data set NMF algorithm and locked. The results of this are presented in **Figure 5.4**. The response factors of the nine resolved spectral factors correlate well to expectations. Each of the isolated spectral factors only show non–zero response factors in the measurements where their respective compound is expected to be present. In addition, during assays, the sensor and sensitizer

response profiles decrease over time, as expected. In PB there is one resolved unknown factor set, indicated as a photoproduct in **Figure 5.4**. This possible photoproduct has a wavelength of maximum absorbance of 552 nm, similar to that of the sensitizer's main absorption band (550 nm). The response vector of this photoproduct only appears in the ambient assay measurements (unique data types #13–17, as listed in **Table 5.1**), and does not appear in any controls nor the degassed assays. These results suggest that this is a photoproduct reliant on the presence of molecular oxygen. However, these results are not without limitation. There appears to be some minor spurious correlation between the previously resolve sensitizer vectors among the assay measurements. This correlation may undermine the partitioning of the data matrix, leading to incorrect kinetic resolution of the sensitizer.

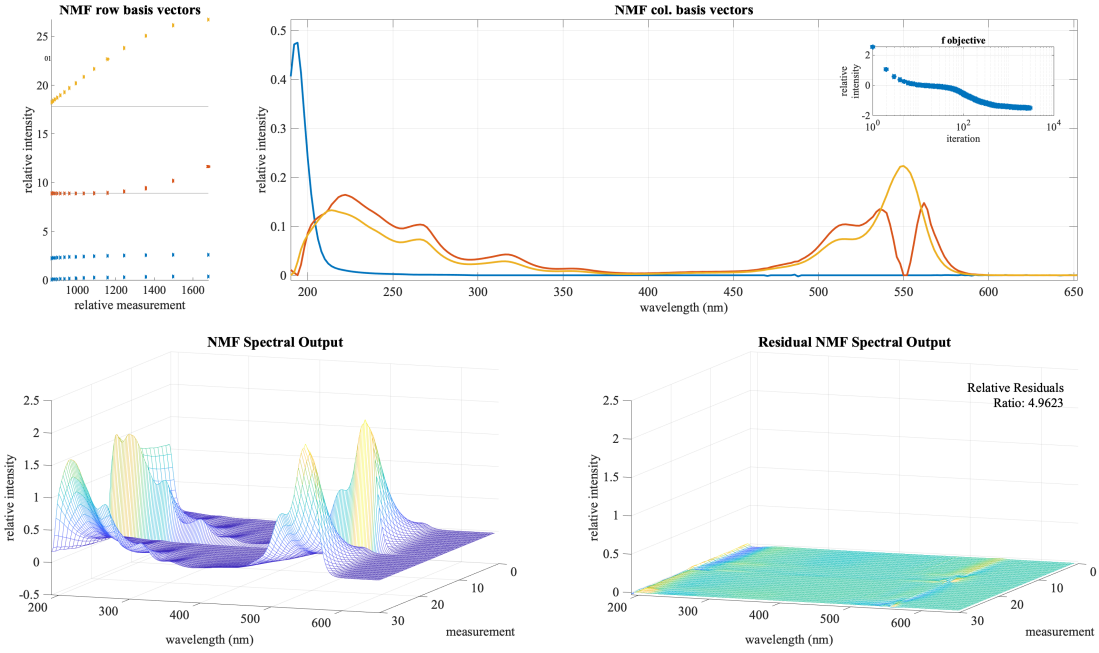

Figure 5.3: Non-negative matrices (row and column basis vectors) resulting from the NMF algorithm applied to sensitizer (RB) reagent calibrations.

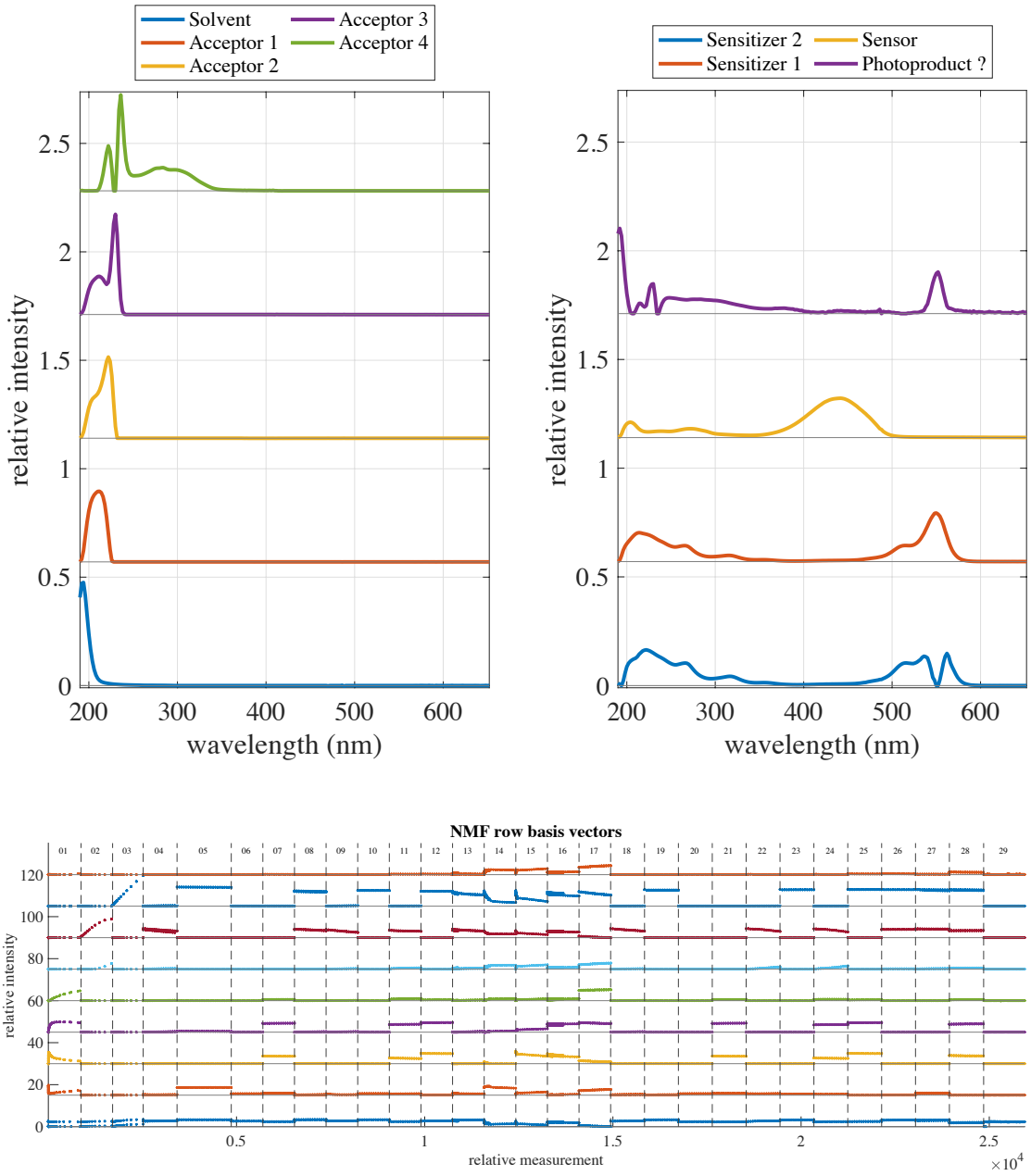

Figure 5.4: Spectral (top) and response (bottom) factors resolved from the PB data set (RBRNOPB). Unique data types are grouped and numbered; conditions of each data type are listed in **Table 5.1** below.

In SDS, pseudorank estimation using SVD (**Figure 5.5**) revealed a likely five factors, i.e. spectra and response profiles, with factors 6–10 having possible significance. Like with the RBRNOPB data set, following SVD analysis, reagent calibrations were subjected individually to SVD and NMF analysis to compile resolved spectra of isolated reagent profiles. From the individual analysis of reagent calibrations for the sensitizer (RB), sensor (RNO), and acceptor (Imd), a total of eight factors were distinguished. Of the nine factors, one was for the solvent, two for the sensitizer, one for the sensor, and four for the quencher. Just as in PB, the acceptor (Imd) spectrum shifts considerably with concentration, so that four linear factors are needed to describe its response in both solvents across the range of concentrations used in the assays. Also, as with PB, the sensitizer showed signs of aggregates at high concentrations within the calibrations, and therefore required two factors.

These nine resolved spectral factors were incorporated into the beginning estimate of the constrained analysis of the RBRNOSDS data set NMF algorithm and locked. The results of this are presented in **Figure 5.6**. The response factors of the nine resolved spectral factors correlate well to expectations. Each of the isolated spectral factors only show non–zero responses in the measurements where their corresponding compound is expected to be present. In addition, during assays, the sensor and sensitizer response profiles decrease over time, as expected. In SDS there is one resolved unknown factor set, indicated as a photoproduct in **Figure 5.6**. This possible photoproduct has a wavelength of maximum absorbance of 532 nm, significantly shifted from that of the sensitizer's main absorption band (550 nm). Unlike the photoproduct isolated in PB, the response vector of this photoproduct appears in both the ambient assay measurements, and the degassed assays, as well as select controls where the sensitizer and acceptor are

present. In addition, the photoproduct appearance occurs at a much faster rate with increased acceptor concentration. These results suggest that this is a photoproduct resulting from interaction between the sensitizer (RB) and acceptor (Imd), that does not rely on the presence of molecular oxygen—in fact it appears at its highest rate in the sensitizer/high acceptor/degassed data set (#24). However, these results are also not without limitation. There appears to be some minor spurious correlation between the second resolve sensitizer vector (vector present at high [RB]) and the photoproduct among the assay measurements. This correlation may undermine the partitioning of the data matrix, leading to incorrect kinetic resolution of the sensitizer and photoproduct.

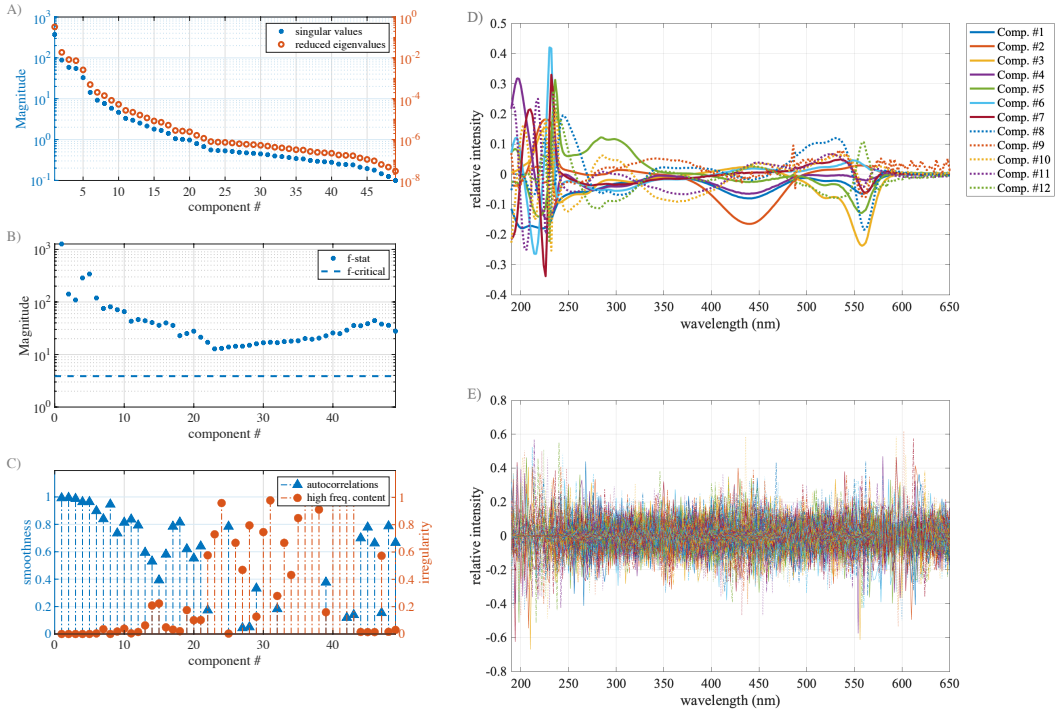

Figure 5.5: Pseudorank estimation of concatenated RBRNOSDS data sets. A) Log of singular values and reduced eigenvalues.[43] B) F–test of reduced eigenvalues.[39] C) Column (spectral) singular vector autocorrelations (blue Δ's) and high–frequency content (orange O's).[40,42] D) The first ten column (wavelength) singular vectors; determined as significant. E) The remaining column singular vectors; determined as insignificant.

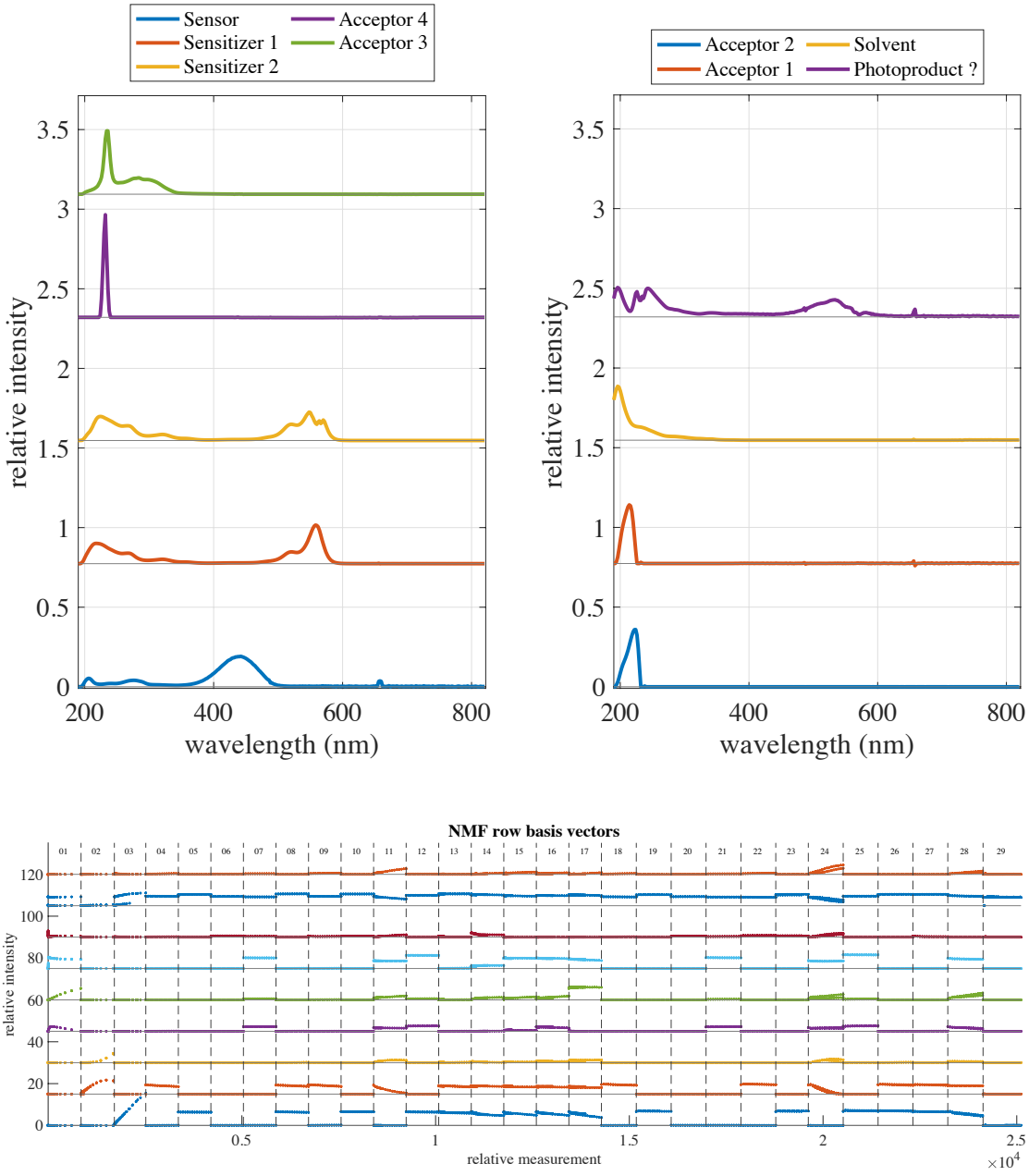

Figure 5.6: Spectral (top) and response (bottom) factors resolved from the SDS data set (RBRNOSDS). Unique data types are grouped and numbered; conditions of each data type are listed in **Table 5.1** below.

Table 5.1: Assay conditions for **Figures 5.4** & **5.6**. Reagents present in sample are listed followed by their concentrations in parenthesis. Samples that were degassed are indicated. Data sets that were calibrations (molar absorptivities) are also indicated.

#	Reaction Components	#	Reaction Components
1	Imd (MolarAbs)	16	RB (1e-05 µM) RNO (5e-05 µM) Imd (0.05 µM)
2	RB (MolarAbs)	17	RB (1e-05 µM) RNO (5e-05 µM) Imd (0.5 µM)
3	RNO (MolarAbs)	18	RB (1e-05 µM) (degassed)
4	RB (0.01 µM)	19	RNO (5e-05 µM) (degassed)
5	RNO (5e-05 µM)	20	Imd (5e-05 µM) (degassed)
6	Imd (5e-05 µM)	21	Imd (0.05 µM) (degassed)
7	Imd (0.05 µM)	22	RB (1e-05 µM) Imd (5e-05 µM) (degassed)
8	RB (1e-05 µM) RNO (5e-05 µM)	23	RNO (5e-05 µM) Imd (5e-05 µM) (degassed)
9	RB (1e-05 µM) Imd (5e-05 µM)	24	RB (1e-05 µM) Imd (0.05 µM) (degassed)
10	RNO (5e-05 µM) Imd (5e-05 µM)	25	RNO (5e-05 µM) Imd (0.05 µM) (degassed)
11	RB (1e-05 µM) Imd (0.05 µM)	26	RB (1e-05 µM) RNO (5e-05 µM) (degassed)
12	RNO (5e-05 µM) Imd (0.05 µM)	27	RB (1e-05 µM) RNO (5e-05 µM) Imd (5e-05 µM) (degassed)
13	RB (1e-05 µM) RNO (5e-05 µM) Imd (5e-05 µM)	28	RB (1e-05 µM) RNO (5e-05 µM) Imd (0.05 µM) (degassed)
14	RB (1e-05 µM) RNO (5e-05 µM) Imd (0.0005 µM)	29	Compiled Solvent Spectra
15	RB (1e-05 µM) RNO (5e-05 µM) Imd (0.005 µM)		

Resolved spectral and response factors for the sensor and sensitizer of the RBRNOPB and RBRNOSDS data sets were subjected to kinetic analysis, and compared to previous results obtained from raw, unresolved data at single wavelengths of maximum absorbance. The results from the resolved factors are depicted in **Figure 5.7** as dashed lines, while the previous results are depicted as solid lines. In PB, the resolved kinetics for the sensor were not significantly different from the previous results. A peak in sensor bleaching in the millimolar range was observed. On the other hand, resolved

kinetics for the sensitizer are significantly altered at low acceptor concentrations, lower than 5 mM. The dependence of the sensitizer degradation in relation to acceptor concentration now mirrors than of the sensor, with a peak degradation rate at 5 mM. In SDS, the sensor rates at relatively higher acceptor concentration, greater than 5 mM, were altered; however, in considering the measurement errors, the change may be negligible. Likewise, little difference was observed between the resolved and previous kinetic results of the sensitizer in SDS. These results indicate that the sensitizer degradation rate determinations are most affected by resolution, while the sensor bleaching is least affected. This suggest that within the conditions of this work, traditional single–wavelength kinetic analysis of the RNO sensor is sufficient in determining sensors bleaching rates.

In addition to comparing the resolved and previous sensor and sensitizer bleaching rates within assay measurements, rates within controls measurements were also compared. As is depicted in **Figures 5.8** & **5.9**, no substantial changes in either set of control measurements were observed. This could indicate that the results are a reflection of discrepancies from the expected mechanism that may undermine the assay's use in across solvents. Again, these results underscore the importance of using appropriate controls in ROS detection measurements beyond the specific method used in this study. In addition, it appears that spectral resolution had no effect on the kinetic results of these control data sets.

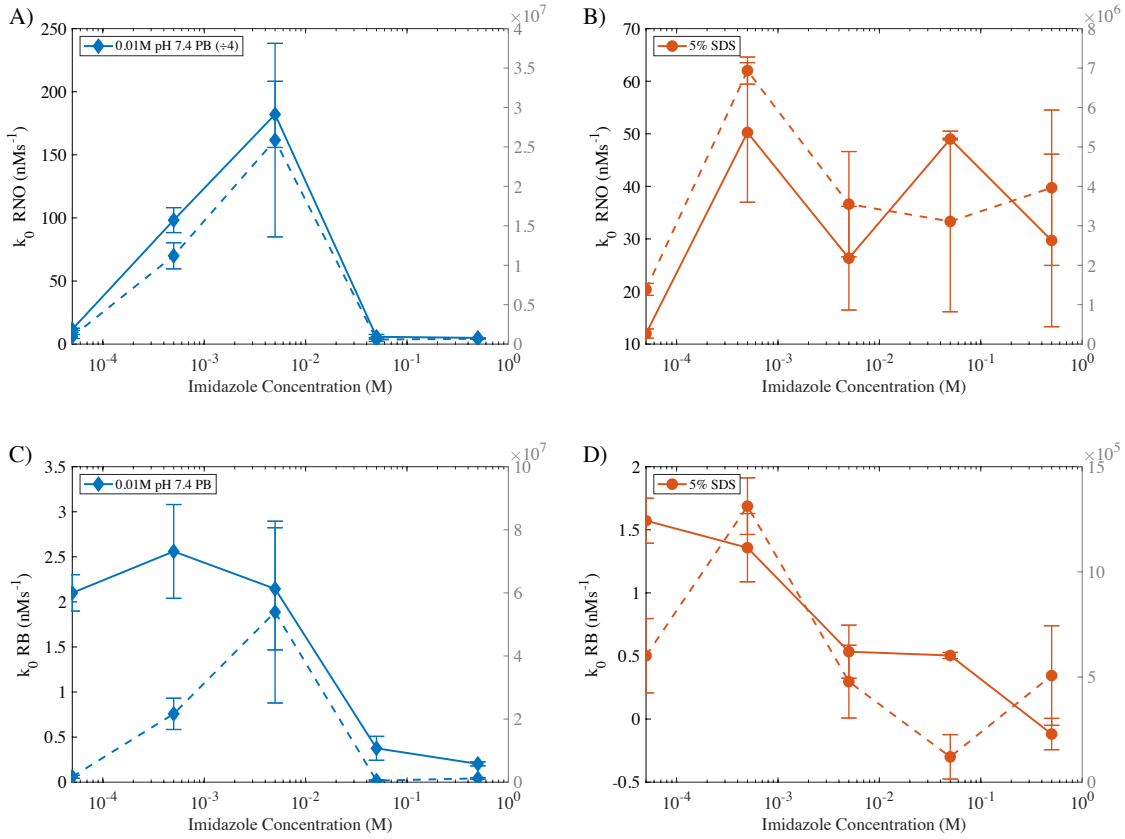

Figure 5.7: Comparison of zero order photobleaching rate constants of the sensor (A & B) and sensitizer (C & D) at various Imd concentrations as a result of RB photosensitization and subsequent $^1O_2$ production in PB (blue) and SDS (orange). Solid lines represent kinetic results obtained by traditional methods, while the dashed lines represent kinetic results obtained from multivariate methods. Uncertainties represent 1 standard deviation from the mean; $N \geq 3$.

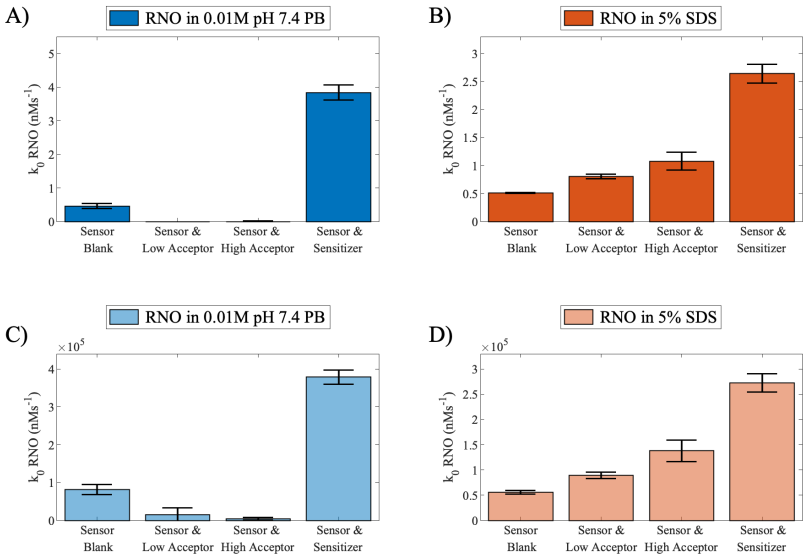

Figure 5.8: Comparison of zero order photobleaching rate constants of the sensor during control measurements of the Imd/RNO method in PB (blue) and SDS (orange). Subplots A & B depict kinetic results obtained by traditional methods, while subplots C & D depict kinetic results obtained from multivariate methods.

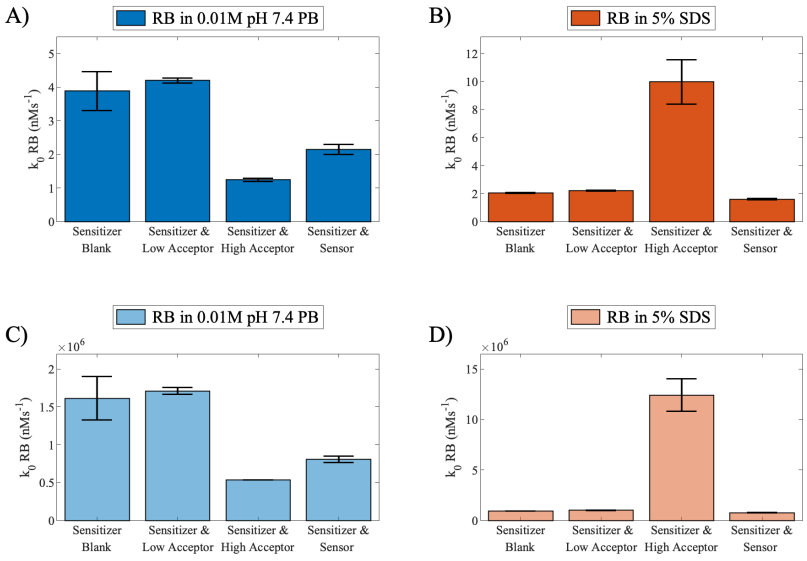

Figure 5.9: Comparison of zero order photobleaching rate constants of the sensitizer during control measurements of the Imd/RNO method in PB (blue) and SDS (orange). Subplots A & B depict kinetic results obtained by traditional methods, while subplots C & D depict kinetic results obtained from multivariate methods.

5.5 Conclusion

Singular value decomposition[19] and non–negative matrix factorization[20] were used to resolve isolated chromophore spectral and response profiles from colorimetric data collected during Imd/RNO assays. The data sets collected in the measurements reported here consist of a series of absorbance spectra monitored with respect to time arranged. Series of spectra collected as Rose Bengal sensitized singlet oxygen assays, controls and calibrations were performed in phosphate buffer (PB) and sodium dodecyl sulfate (SDS) were arranged in matrix format and concatenated to form single matrices that capture the range of responses in each solvent. Spectral isolation was improved through concatenation of a series of calibrations, control, and ROS assay measurements—including molar absorptivities, photodegradation controls, and assay data with varied initial reagent concentration. The resulting resolved response profiles for assay reagents of the Imd plus RNO method were then subjected to kinetic profiling, to compare resolved reaction rate constants to those determined by the traditional, single–wavelength, analysis approach.

The results of this research illustrate the potential for spectral and response resolution of colorimetric data as a result of concatenating data sets and subjecting them to numerical analysis techniques. In each of the PB and SDS data sets, nine spectral and response vectors were resolved. In each vector set, eight of the nine vectors were identified as reaction components—solvent (one vector), acceptor (four vectors), sensitizer (two vectors), and sensor (one vector). Among the identified vectors, the acceptor (Imd) required four vectors due to its complex absorptivity profiles; this complex nature created challenges in resolving the near UV region of the spectral vectors. In addition, the sensitizer (RB) required two vectors to account for the pure sensitizer and aggregation at high concentration. The sensitizers second vector added

challenges to resolution of the sensitizer due to some spurious correlations between the two vectors. The final vector of each set was resolved as a photoproduct. In PB the photoproduct appeared only in ambient assay conditions, with no appearance in the controls, nor degassed assays. While in SDS the photoproduct appeared during all assay and control measurements where the sensitizer and acceptor were present, particularly at high acceptor concentrations.

Following resolving the spectral and response profiles, the resulting vectors were subjected to kinetic analysis and compared to kinetic results obtained previously though a traditional single–wavelength approach. Despite the relatively successful isolation of the sensor and sensitizer vectors, minimal changes in the assay and control bleaching rates for both the sensors or sensitizer were observed. In the assays the only significant change was observed for the sensitizer degradation in PB at low acceptor concentrations. Previously, results indicated that the sensitizer in PB degraded the fastest at low acceptor concentrations; however, the results presented in this research illustrate a sensitizer degradation dependence on acceptor concentration mirror the bleaching dependence of the sensor, with a peak rate in the millimolar range. This, however, was the only significant change among the assay and control measurements analyzed by this work.

As was concluded by previous work,[18] the solvent–dependent differences in the performance of the Imd/RNO method continue to indicate that caution is warranted and confirmatory controls are advised when using the assay in any solvent other than PB. They also raise questions about the robustness of the method in complex samples that contain cells, biological tissues, or nanoparticles, and underscore the importance of using appropriate controls in ROS detection measurements beyond the specific method

used in this study, as the sensors and systems under investigation become increasingly complex. Resolving the sensor and sensitizer spectral and response vectors did not have a significant impact on the SDS assay nor controls. On the other hand, significant changes to assay results in PB at low acceptor concentration were observed that may reinforce the validity of the Imd/RNO method for use in aqueous PB. Though vectors were resolved during this analysis, spurious correlations between vectors do remain that require additional work.

Chapter 6

CONCLUSION

6.1 Summary

The objectives for the research contained in this dissertation was the demonstration of the efficiency, or lack thereof, of select commercially available colorimetric ROS sensors for their use in environmentally and biologically relevant samples, as well as investigating the potential improvements to the kinetic analysis of optical data resulting from sensor measurements using a vigorous series of control measurements and numerical analysis strategies. Fundamental methodology for the instrumentation—including broadband UV–Vis spectrophotometry and solar simulation—and data analysis—including singular value decomposition and non–negative matrix factorization—used for the research contained in this dissertation were described in **Chapter 2**.

The first study, presented in **Chapter 3**, was a compilation of the stability controls used to initially assess the use of selected common ROS sensors in environmentally or biologically relevant samples. Sensor stability was evaluated using two types of assay control measurements: broadband molar absorptivity, and photostability under broadband simulated sunlight. The stability of three singlet oxygen sensors—1,3-diphenylisobenzofuran (DPBF), 9,10-anthracenedipropionic acid (ADPA), and p-nitrosodimethylaniline (RNO) plus imidazole (Imd)—in addition to three superoxide sensors—7-chloro-4-nitrobenzo-2-oxa-1,3-diazole (NBD-Cl), 1,4-benzoquinone (BQ), and 3-(4,5-dimethyl-2-thiazol)-2,5-di-phenyl-2H-tetrazolium

bromide (MTT)—were evaluated. Out of the six sensors, two were determined acceptable for use in the proposed environmentally and biologically relevant conditions the Imd plus RNO method for $^1O_2$ detection, and the MTT sensor for $O_2^{\bullet-}$ detection. Due to the instability observed in the reaming sensors, caution and attention to control measurements are suggested when using these, and potentially other, ROS chemical sensors in the environmentally and biologically relevant conditions of this, and similar, work.

The second study, presented in **Chapter 4**, the efficiency of the imidazole plus RNO method for singlet oxygen detection in biorelevant solvents was compared. In this portion of this dissertation, the efficiency of the Imd/RNO method in complex, biorelevant solvents was compared to reference solvents using Rose Bengal photosensitization to produce $^1O_2$ monitored using time-resolved, broadband UV–Vis absorbance measurements. Rates of sensor bleaching and sensitizer photodegradation were simultaneously monitored in each solvent to investigate correlations between the disappearance rates of sensor and sensitizer. To illustrate the efficiency of the method across the solvents, the quantum yields of $^1O_2$ production in each solvent were calculated using a relative actinometric method. The dependence of sensor bleaching and sensitizer degradation on acceptor concentration and solvent polarity, and the results of assay controls indicate differences in mechanisms underlying the reactions comprising the Imd/RNO method. These results demonstrate the need for caution and controls when using the method in complex samples including those containing cells, tissues or nanoscale particles.

The last study of this dissertation, presented in **Chapter 5**, was an attempt to improve the analysis of colorimetric data resulting from the use of the Imd plus RNO

method using numerical analysis strategies. In this work singular value decomposition[19] and non–negative matrix factorization[20] were used to resolve isolated chromophore spectral and response profiles from colorimetric data. Spectral isolation was improved through concatenation of a series of calibrations, control, and ROS assay measurements—including molar absorptivities, photodegradation controls, and assay data with varied initial reagent concentration. The results illustrated the potential for spectral and response resolution of colorimetric data by resolving photoproducts that illustrated differing spectral and response characteristics across the two solvents. Resolving the sensor and sensitizer spectral and response vectors did not have a significant impact on the SDS assay nor controls. On the other hand, significant changes to assay results in PB at low acceptor concentration were observed that may reinforce the validity of the Imd/RNO method for use in aqueous PB. Though vectors were resolved during this analysis, spurious correlations between vectors do remain that require additional work.

This work in whole has continuously illustrated the solvent–dependent differences in the performance of the Imd/RNO method, indicating the need for caution and confirmatory controls when using the assay in any solvent other than PB. While many of the sensors in Chapter 3 were only analyzed on a preliminary basis (stability controls), the results pertaining to the Imd/RNO method are significant enough to warrant caution and inclusion of confirmatory controls when using any chemical sensor for ROS detection.

REFERENCES

(1) Hayyan, M.; Hashim, M. A.; Alnashef, I. M. Superoxide Ion: Generation and Chemical Implications. *Chem. Rev.* **2016**, *116* (5), 3029–3085. https://doi.org/10.1021/acs.chemrev.5b00407.

(2) Fu, P. P.; Xia, Q. S.; Hwang, H. M.; Ray, P. C.; Yu, H. T. Mechanisms of Nanotoxicity: Generation of Reactive Oxygen Species. *J. Food Drug Anal.* **2014**, *22* (1), 64–75. https://doi.org/10.1016/j.jfda.2014.01.005.

(3) Holmstrom, K. M.; Finkel, T. Cellular Mechanisms and Physiological Consequences of Redox-Dependent Signalling. *Nat. Rev. Mol. Cell Biol.* **2014**, *15* (6), 411–421. https://doi.org/10.1038/nrm3801.

(4) Bethi, B.; Sonawane, S. H.; Bhanvase, B. A.; Gumfekar, S. P. Nanomaterials-Based Advanced Oxidation Processes for Wastewater Treatment: A Review. *Chem. Eng. Process. Process Intensif.* **2016**, *109*, 178–189. https://doi.org/10.1016/j.cep.2016.08.016.

(5) Zhou, Z. J.; Song, J. B.; Nie, L. M.; Chen, X. Y. Reactive Oxygen Species Generating Systems Meeting Challenges of Photodynamic Cancer Therapy. *Chem. Soc. Rev.* **2016**, *45* (23), 6597–6626. https://doi.org/10.1039/c6cs00271d.

(6) DeRosa, M. C.; Crutchley, R. J. Photosensitized Singlet Oxygen and Its Applications. *Coord. Chem. Rev.* **2002**, *233–234*, 351–371. https://doi.org/10.1016/S0010-8545(02)00034-6.

(7) Schöneich, C.; Sharov, V. S. Mass Spectrometry of Protein Modifications by Reactive Oxygen and Nitrogen Species. *Free Radical Biology and Medicine*. Pergamon November 15, 2006, pp 1507–1520. https://doi.org/10.1016/j.freeradbiomed.2006.08.013.

(8) Butterfield, D. A.; Perluigi, M.; Reed, T.; Muharib, T.; Hughes, C. P.; Robinson, R. A. S.; Sultana, R. Redox Proteomics in Selected Neurodegenerative Disorders: From Its Infancy to Future Applications. *Antioxidants and Redox Signaling*. Mary Ann Liebert, Inc. 140 Huguenot Street, 3rd Floor New Rochelle, NY 10801 USA January 12, 2012, pp 1610–

1655. https://doi.org/10.1089/ars.2011.4109.

(9) Borgmann, S. Electrochemical Quantification of Reactive Oxygen and Nitrogen: Challenges and Opportunities. *Analytical and Bioanalytical Chemistry*. Springer May 12, 2009, pp 95–105. https://doi.org/10.1007/s00216-009-2692-1.

(10) Andina, D.; Leroux, J.-C. C.; Luciani, P. Ratiometric Fluorescent Probes for the Detection of Reactive Oxygen Species. *Chem. - A Eur. J.* **2017**, *23* (55), 13549–13573. https://doi.org/10.1002/chem.201702458.

(11) Wu, H. Y.; Song, Q. J.; Ran, G. X.; Lu, X. M.; Xu, B. G. Recent Developments in the Detection of Singlet Oxygen with Molecular Spectroscopic Methods. *TrAC - Trends Anal. Chem.* **2011**, *30* (1), 133–141. https://doi.org/10.1016/j.trac.2010.08.009.

(12) Chen, X. Q.; Wang, F.; Hyun, J. Y.; Wei, T. W.; Qiang, J.; Ren, X. T.; Shin, I.; Yoon, J. Recent Progress in the Development of Fluorescent, Luminescent and Colorimetric Probes for Detection of Reactive Oxygen and Nitrogen Species. *Chem. Soc. Rev.* **2016**, *45* (10), 2976–3016. https://doi.org/10.1039/C6CS00192K.

(13) Herman, J.; Zhang, Y.; Castranova, V.; Neal, S. L. Emerging Technologies for Optical Spectral Detection of Reactive Oxygen Species. *Anal. Bioanal. Chem.* **2018**, *410* (24), 6079–6095. https://doi.org/10.1007/s00216-018-1233-1.

(14) Winterbourn, C. C. The Challenges of Using Fluorescent Probes to Detect and Quantify Specific Reactive Oxygen Species in Living Cells. *Biochim. Biophys. Acta - Gen. Subj.* **2014**, *1840* (2), 730–738. https://doi.org/10.1016/j.bbagen.2013.05.004.

(15) Chen, X.; Tian, X.; Shin, I.; Yoon, J. Fluorescent and Luminescent Probes for Detection of Reactive Oxygen and Nitrogen Species. *Chem. Soc. Rev.* **2011**, *40* (9), 4783. https://doi.org/10.1039/c1cs15037e.

(16) Fernández-Castro, P.; Vallejo, M.; San Román, M. F.; Ortiz, I. Insight on the Fundamentals of Advanced Oxidation Processes: Role and Review of the Determination Methods of Reactive Oxygen Species. *J. Chem. Technol. Biotechnol.* **2015**, *90* (5), 796–820. https://doi.org/10.1002/jctb.4634.

(17) Nosaka, Y.; Nosaka, A. Y. Generation and Detection of Reactive Oxygen Species in Photocatalysis. *Chem. Rev.* **2017**, *117* (17), 11302–11336. https://doi.org/10.1021/acs.chemrev.7b00161.

(18) Herman, J.; Neal, S. L. Efficiency Comparison of the Imidazole plus RNO Method for Singlet Oxygen Detection in Biorelevant Solvents. *Anal. Bioanal. Chem.* **2019**, *411* (20), 5287–5296. https://doi.org/10.1007/s00216-019-01910-2.

(19) Strang, G. *Linear Algebra and Its Applications*, 3rd ed.; Harcourt Brace Jovanovich, Publishers: San Diego, 1988.

(20) Lee, D. D.; Seung, H. S. Learning the Parts of Objects by Non-Negative Matrix Factorization. *Nature* **1999**, *401* (6755), 788–791.

(21) Ludvíková, L.; Friš, P.; Heger, D.; Šebej, P.; Wirz, J.; Klán, P. Photochemistry of Rose Bengal in Water and Acetonitrile: A Comprehensive Kinetic Analysis: SUPPLEMENTAL INFO. *Phys. Chem. Chem. Phys.* **2016**, *18* (24), 1–15. https://doi.org/10.1039/C6CP01710J.

(22) Neckers, D. C. Rose Bengal. *J. Photochem. Photobiol. A Chem.* **1989**, *47* (1), 1–29. https://doi.org/10.1016/1010-6030(89)85002-6.

(23) Islam, S. D. M.; Ito, O. Solvent Effects on Rates of Photochemical Reactions of Rose Bengal Triplet State Studied by Nanosecond Laser Photolysis. *J. Photochem. Photobiol. A Chem.* **1999**, *123*, 53–59. https://doi.org/10.1016/S1010-6030(99)00042-8.

(24) Wilkinson, F.; Helman, W. P.; Ross, A. B. Quantum Yields for the Photosensitized Formation of the Lowest Electronically Excited Singlet State of Molecular Oxygen in Solution. *J. Phys. Chem. Ref. Data* **1993**, *22* (1), 113–261.

(25) Redmond, R. W.; Gamlin, J. N. A Compilation of Singlet Oxygen Yields from Biologically Relevant Molecules. *Photochem. Photobiol.* **1999**, *70* (4), 391–475. https://doi.org/10.1111/j.1751-1097.1999.tb08240.x.

(26) Schaap, A. P.; Thayer, A. L.; Blossey, E. C.; Neckers, D. C. Polymer-Based Sensitizers for Photooxidations. II. *J. Am. Chem. Soc.* **1975**, *97* (13), 3741–3745. https://doi.org/10.1021/ja00846a030.

(27) Chen, B.; Siepmann, J. I. Microscopic Structure and Solvation in Dry and Wet Octanol. *J. Phys. Chem. B* **2006**, *110* (8), 3555–3563. https://doi.org/10.1021/jp0548164.

(28) Kai, H.; Yan, Z.; Junfeng, S.; Zhenping, J.; Gongzhen, C. Microheterogeneous Structure of 1-Octanol in Neat and Water-Saturated State. *J. Phys. Chem. B* **2007**, *111* (34), 10160–10165. https://doi.org/10.1021/jp072847o.

(29) Stratford, C. Oriel Product Training - Solar Simulation. Newport 2016, p 5.

(30) Esen, V.; Sa, Ş.; Oral, B.; Esen, Ö. C. Spectrum Measurement of Variable Irradiance Controlled LED-Based Solar Simulator. *Int. J. Renew. ENERGY Res.* **2020**, *10* (1).

(31) Leary, G. P. Comparison of Xenon Lamp-Based and Led-Based Solar Simulators. *Mont. State Univ. Thesis* **2016**. https://doi.org/10.1017/CBO9781107415324.004.

(32) Kolberg, D.; Schubert, F.; Lontke, N.; Zwigart, A.; Spinner, D. M. Development of Tunable Close Match LED Solar Simulator with Extended Spectral Range to UV and IR. In *Energy Procedia*; Elsevier Ltd, 2011; Vol. 8, pp 100–105. https://doi.org/10.1016/j.egypro.2011.06.109.

(33) Hatchard, C. G.; Parker, C. A. A New Sensitive Chemical Actinometer - II. Potassium Ferrioxalate as a Standard Chemical Actinometer. *Proc. R. Soc. London. Ser. A. Math. Phys. Sci.* **1956**, *235* (1203), 518–536. https://doi.org/10.1098/rspa.1956.0102.

(34) Laszakovits, J. R.; Berg, S. M.; Anderson, B. G.; O'Brien, J. E.; Wammer, K. H.; Sharpless, C. M. P-Nitroanisole/Pyridine and p-Nitroacetophenone/Pyridine Actinometers Revisited: Quantum Yield in Comparison to Ferrioxalate. *Environ. Sci. Technol. Lett.* **2017**, *4* (1), 11–14. https://doi.org/10.1021/acs.estlett.6b00422.

(35) Asenath-Smith, E.; Ambrogi, E. K.; Moores, L. C.; Newman, S. D.; Brame, J. A. Leveraging Chemical Actinometry and Optical Radiometry to Reduce Uncertainty in Photochemical Research. *J. Photochem. Photobiol. A Chem.* **2019**, *372*, 279–287. https://doi.org/10.1016/j.jphotochem.2018.12.024.

(36) Pozdnyakov, I. P.; Kel, O. V.; Plyusnin, V. F.; Grivin, V. P.; Bazhin, N. M. New Insight into Photochemistry of Ferrioxalate. *J. Phys. Chem. A* **2008**, *112* (36), 8316–8322. https://doi.org/10.1021/jp8040583.

(37) Sigmann, S. B.; Wheeler*, D. E. The Quantitative Determination of Food Dyes in Powdered Drink Mixes. *J. Chem. Educ.* **2004**, *81* (10), 1475–1478.

(38) Neal, S. L. Multivariate Analysis of Mixed Lipid Aggregate Phase Transitions Monitored Using Raman Spectroscopy. *Appl. Spectrosc.* **2018**, *72* (1), 102–113. https://doi.org/10.1177/0003702817729347.

(39) Faber, K.; Kowalski, B. R. Modification of Malinowski's F-Test for Abstract Factor Analysis Applied to the Quail Roost II Data Sets. *J. Chemom.* **1997**, *11*

(1), 53–72.

(40) Rossi, T. M.; Warner, I. M. Rank Estimation of Excitation-Emission Matrices Using Frequency Analysis of Eigenvectors. *Anal. Chem.* **1986**, *58*, 810–815.

(41) Wold, S. Cross-Validatory Estimation of the Number of Cmponents in Factorr and Principal Component Models. *Technometrics* **1978**, *20* (4), 397–405.

(42) Shrager, R. I.; Hendler, R. W. Titration of Individual Components in a Mixture with Resolution of Difference Spectra, PKs and Redox Transitions. *Anal. Chem.* **1982**, *54* (7), 1147–1152.

(43) Malinowski, E. R. *Factor Analysis in Chemistry*, 2nd ed.; Wiley: New York, 1991.

(44) Windig, W.; Guilment, J. Interactive Self-Modeling Mixture Analysis. *Anal. Chem.* **1991**, *63* (14), 1425–1432.

(45) de Juan, A.; VanderHeyden, Y.; Tauler, R.; Massart, D. L. Assessment of New Constraints Applied to the Alternating Least Squares Method. *Anal. Chim. Acta* **1997**, *346* (3), 307–318.

(46) Neal, S. L.; Davidson, E. R.; Warner, I. M. Resolution of Severely Overlapped Spectra from Matrix-Formatted Spectral Data Using Constrained Nonlinear Optimization. *Anal. Chem.* **1990**, *62*, 658–664.

(47) Neal, S. L. Model-Independent Estimation of the Photokinetic Transfer Matrix from Matrix-Formatted Frequency-Domain Fluorescence. *J. Phys. Chem. A* **1997**, *101*, 6883–6889.

(48) Paatero, P.; Tapper, U. Positive Matrix Factorization - A Nonnegative Factor Model With Optimal Utilization Of Error-Estimates Of Data Values. *Environmetrics* **1994**, *5* (2), 111–126.

(49) Van Benthem, M. H.; Keenan, M. R.; Haaland, D. M. Application of Equality Constraints on Variables during Alternating Least Squares Procedures. *J. Chemom.* **2002**, *16* (12), 613–622.

(50) Mirzal, A. Orthogonal Nonnegative Matrix Factorization for Blind Image Separation. In *Advances in Visual Informatics*; Springer International Publishing, 2013; pp 20–35.

(51) Burns, J. M.; Cooper, W. J.; Ferry, J. L.; King, D. W.; DiMento, B. P.; McNeill, K.; Miller, C. J.; Miller, W. L.; Peake, B. M.; Rusak, S. A.; Rose, A. L.; Waite,

T. D. Methods for Reactive Oxygen Species (ROS) Detection in Aqueous Environments. *Aquat. Sci.* **2012**, *74* (4), 683–734. https://doi.org/10.1007/s00027-012-0251-x.

(52) Madesh, M.; Balasubramanillll, K. Microtiter Plate Assay for Superoxide Dismutase Using MTT Reduction by Superoxide. *Indian J Biochem Biophys* **1998**, *35*, 184–188.

(53) Valduga, G.; Nonell, S.; Reddi, E.; Jori, G.; Braslavsky, S. E. The Production of Singlet Molecular Oxygen by Zinc(II) Phthalocyanine in Ethanol And in Unilamellar Vesicles: Chemical Quenching and Phosphorescence Studies. *Photochem. Photobiol.* **1988**, *48* (1), 1–5. https://doi.org/10.1111/j.1751-1097.1988.tb02778.x.

(54) SPILLER, W.; KLIESCH, H.; WÖHRLE, D.; HACKBARTH, S.; RÖDER, B.; SCHNURPFEIL, G. Singlet Oxygen Quantum Yields of Different Photosensitizers in Polar Solvents and Micellar Solutions. *J. Porphyrins Phthalocyanines* **1998**, *02* (02), 145–158. https://doi.org/10.1002/(SICI)1099-1409(199803/04)2:2<145::AID-JPP60>3.0.CO;2-2.

(55) Luengas, S. L. P.; Marin, G. H.; Aviles, K.; Acuña, R. C.; Roque, G.; Nieto, F. R.; Sanchez, F.; Tarditi, A.; Rivera, L.; Mansilla, E. Enhanced Singlet Oxygen Production by Photodynamic Therapy and a Novel Method for Its Intracellular Measurement. *Cancer Biother. Radiopharm.* **2014**, *29* (10), 435–443. https://doi.org/10.1089/cbr.2014.1718.

(56) Bresolí-Obach, R.; Nos, J.; Mora, M.; Sagristà, M. L.; Ruiz-González, R.; Nonell, S. Anthracene-Based Fluorescent Nanoprobes for Singlet Oxygen Detection in Biological Media. *Methods* **2016**, *109*, 64–72. https://doi.org/10.1016/j.ymeth.2016.06.007.

(57) Lindig, B. A.; Rodgers, M. A. J.; Schaaplc, A. P. Determination of the Lifetime of Singlet Oxygen in D20 Using 9,10-Anthracenedipropionic Acid, a Water-Soluble Probe. *J. Am. Chem. Soc.* **1980**, *102* (17), 5590–5593. https://doi.org/10.1021/ja00537a030.

(58) Doria, F.; Manet, I.; Grande, V.; Monti, S.; Freccero, M. Water-Soluble Naphthalene Diimides as Singlet Oxygen Sensitizers. *J. Org. Chem.* **2013**, *78* (16), 8065–8073. https://doi.org/10.1021/jo401347z.

(59) Spanò, V.; Frasson, I.; Giallombardo, D.; Doria, F.; Parrino, B.; Carbone, A.; Montalbano, A.; Nadai, M.; Diana, P.; Cirrincione, G.; Freccero, M.; Richter, S. N.; Barraja, P. Synthesis and Antiproliferative Mechanism of Action of Pyrrolo[3′,2′:6,7] Cyclohepta[1,2-d]Pyrimidin-2-Amines as Singlet Oxygen

Photosensitizers. *Eur. J. Med. Chem.* **2016**, *123*, 447–461. https://doi.org/10.1016/j.ejmech.2016.07.051.

(60) Hasunuma, N.; Kawakami, M.; Hiramatsu, H.; Nakabayashi, T. Preparation and Photo-Induced Activities of Water-Soluble Amyloid β-C60 Complexes. *RSC Adv.* **2018**, *8* (32), 17847–17853. https://doi.org/10.1039/c8ra02789g.

(61) Penon, O.; Marín, M. J.; Amabilino, D. B.; Russell, D. A.; Pérez-García, L. Iron Oxide Nanoparticles Functionalized with Novel Hydrophobic and Hydrophilic Porphyrins as Potential Agents for Photodynamic Therapy. *J. Colloid Interface Sci.* **2016**, *462*, 154–165. https://doi.org/10.1016/j.jcis.2015.09.060.

(62) Kraljić, I.; Mohsni, S. El. A New Method for The Detection of Singlet Oxygen in Aqueous Solutions. *Photochem. Photobiol.* **1978**, *28* (4–5), 577–581. https://doi.org/10.1111/j.1751-1097.1978.tb06972.x.

(63) Rajendran, M.; Inbaraj, J. J.; Gandhidasan, R.; Murugesan, R. Photogeneration of Reactive Oxygen Species by 3-Arylcoumarin and Flavanocoumarin Derivatives. *J. Photochem. Photobiol. A Chem.* **2006**, *182* (1), 67–74. https://doi.org/10.1016/j.jphotochem.2006.01.016.

(64) Fatima, K.; Masood, N.; Luqman, S. Quenching of Singlet Oxygen by Natural and Synthetic Antioxidants and Assessment of Electronic UV/Visible Absorption Spectra for Alleviating or Enhancing the Efficacy of Photodynamic Therapy. *Biomed. Res. Ther.* **2016**, *3* (2), 8. https://doi.org/10.7603/s40730-016-0008-6.

(65) Liu, F.; Zhou, X.; Chen, Z.; Huang, P.; Wang, X.; Zhou, Y. Preparation of Purpurin-18 Loaded Magnetic Nanocarriers in Cottonseed Oil for Photodynamic Therapy. *Mater. Lett.* **2008**, *62* (17–18), 2844–2847. https://doi.org/10.1016/j.matlet.2008.01.123.

(66) Liu, F.; Zhou, X.; Ni, S.; Wang, X.; Zhou, Y.; Chen, Z. Preparation and Properties of Photosensitizer Loaded Magnetic Nanocarriers. *Curr. Nanosci.* **2009**, *5* (3), 293–296. https://doi.org/10.2174/157341309788921480.

(67) Onoue, S.; Yamauchi, Y.; Kojima, T.; Igarashi, N.; Tsuda, Y. Analytical Studies on Photochemical Behavior of Phototoxic Substances; Effect of Detergent Additives on Singlet Oxygen Generation. *Pharm. Res.* **2008**, *25* (4), 861–868. https://doi.org/10.1007/s11095-007-9383-4.

(68) Inbaraj, J. J.; Gandhidasan, R.; Subramanian, S.; Murugesan, R. Photogeneration of Reactive Oxygen Species from Ketocoumarins. *J. Photochem. Photobiol. A Chem.* **1998**, *117* (1), 21–25.

https://doi.org/10.1016/S1010-6030(98)00317-7.

(69) Rajendran, M.; Gandhidasan, R.; Murugesan, R. Photosensitisation and Photoinduced DNA Cleavage by Four Naturally Occurring Anthraquinones. *J. Photochem. Photobiol. A Chem.* **2004**, *168* (1–2), 67–73. https://doi.org/10.1016/j.jphotochem.2004.02.014.

(70) Borisov, S.; Vasillev, V. Formation of Singlet Oxygen Photosensitized by Water-Soluble Metalloporphyrins. *Russ. J. Physcial Chem.* **2001**, *75* (11), 1890–1895.

(71) Krishna, C. M.; Uppuluri, S.; Riesz, P.; JR, J. S. Z.; Balasubramanian, D. A Study of the Photodynamic Efficiencies of Some Eye Lens Constituents. *Photochem. Photobiol.* **1991**, *54* (1), 51–58. https://doi.org/10.1111/j.1751-1097.1991.tb01984.x.

(72) Kim, C. S.; Jung, J. Iron-Sulfur Centers as Endogenous Blue Light Sensitizers in Cells: A Study With an Artificial Non-Heme Iron Protein. *Photochem. Photobiol.* **1992**, *56* (1), 63–68. https://doi.org/10.1111/j.1751-1097.1992.tb09603.x.

(73) Olojo, R. O.; Xia, R. H.; Abramson, J. J. Spectrophotometric and Fluorometric Assay of Superoxide Ion Using 4-Chloro-7-Nitrobenzo-2-Oxa-1,3-Diazole. *Anal. Biochem.* **2005**, *339* (2), 338–344. https://doi.org/10.1016/j.ab.2005.01.032.

(74) Heller, M. I.; Croot, P. L. Application of a Superoxide (O2-) Thermal Source (SOTS-1) for the Determination and Calibration of O2- Fluxes in Seawater. *Anal. Chim. Acta* **2010**, *667* (1–2), 1–13. https://doi.org/10.1016/j.aca.2010.03.054.

(75) Bartosz, G. Use of Spectroscopic Probes for Detection of Reactive Oxygen Species. *Clin. Chim. Acta* **2006**, *368* (1–2), 53–76. https://doi.org/10.1016/j.cca.2005.12.039.

(76) Sutherland, M. W.; Learmonth, B. A. The Tetrazolium Dyes MTS and XTT Provide New Quantitative Assays for Superoxide and Superoxide Dismutase. *Free Radic. Res.* **1997**, *27* (3), 283–289. https://doi.org/10.3109/10715769709065766.

(77) Lambert, C. R.; Kochevar, I. E. Does Rose Bengal Triplet Generate Superoxide Anion? *J. Am. Chem. Soc.* **1996**, *118* (13), 3297–3298. https://doi.org/10.1021/ja9600800.

(78) Peters, G.; Rodgers, M. A. J. Single-Electron Transfer from NADH Analogues to Singlet Oxygen. *BBA - Bioenerg.* **1981**, *637* (1), 43–52. https://doi.org/10.1016/0005-2728(81)90208-5.

(79) Willson, R. L. Pulse Radiolysis Studies of Electron Transfer in Aqueous Quinone Solutions. *Trans. Faraday Soc.* **1971**, *67* (1), 3020. https://doi.org/10.1039/tf9716703020.

(80) Lee, P. C. C.; Rodgers, M. A. J. Laser Flash Photokinetic Studies of Rose Bengal Sensitized Photodynamic Interactions of Nucleotides and Dna. *Photochem. Photobiol.* **1987**, *45* (1), 79–86. https://doi.org/10.1111/j.1751-1097.1987.tb08407.x.

(81) Xu, F.; Song, X. N.; Sheng, G. P.; Luo, H. W.; Li, W. W.; Yao, R. S.; Yu, H. Q. Sunlight-Mediated Degradation of Methyl Orange Sensitized by Riboflavin: Roles of Reactive Oxygen Species. *Sep. Purif. Technol.* **2015**, *142*, 18–24. https://doi.org/10.1016/j.seppur.2014.12.031.

(82) Mojarrad, A. G.; Zakavi, S. A Novel Porphyrinic Photosensitizer Based on the Molecular Complex of Meso -Tetraphenylporphyrin with 2,3-Dichloro-5,6-Dicyano-1,4-Benzoquinone: Higher Photocatalytic Activity, Photooxidative Stability and Solubility in Non-Chlorinated Solvents. *RSC Adv.* **2016**, *6* (103), 100931–100938. https://doi.org/10.1039/c6ra21575k.

(83) Mojarrad, A. G.; Zakavi, S. Photocatalytic Activity of the Molecular Complexes of Meso-Tetraarylporphyrins with Lewis Acids for the Oxidation of Olefins: Significant Effects of Lewis Acids and Meso Substituents. *Eur. J. Inorg. Chem.* **2017**, *2017* (21), 2854–2862. https://doi.org/10.1002/ejic.201700264.

(84) Demirbaş, Ü.; Göl, C.; Barut, B.; Bayrak, R.; Durmuş, M.; Kantekin, H.; Değirmencioğlu, İ. Peripherally and Non-Peripherally Tetra-Benzothiazole Substituted Metal-Free Zinc (II) and Lead (II) Phthalocyanines: Synthesis, Characterization, and Investigation of Photophysical and Photochemical Properties. *J. Mol. Struct.* **2017**, *1130*, 677–687. https://doi.org/10.1016/j.molstruc.2016.11.017.

(85) Heydari-Turkmani, A.; Zakavi, S.; Nikfarjam, N. Novel Metal Free Porphyrinic Photosensitizers Supported on Solvent-Induced Amberlyst-15 Nanoparticles with a Porous Structure. *New J. Chem.* **2017**, *41* (12), 5012–5020. https://doi.org/10.1039/c7nj00791d.

(86) Rajendran, M. Quinones as Photosensitizer for Photodynamic Therapy: ROS Generation, Mechanism and Detection Methods. *Photodiagnosis Photodyn.*

Ther. **2016**, *13*, 175–187. https://doi.org/10.1016/j.pdpdt.2015.07.177.

(87) Wang, S.; Yu, H.; Wickliffe, J. K. Limitation of the MTT and XTT Assays for Measuring Cell Viability Due to Superoxide Formation Induced by Nano-Scale TiO 2. *Toxicol. Vitr.* **2011**, *25* (8), 2147–2151. https://doi.org/10.1016/j.tiv.2011.07.007.

(88) Angius, F.; Floris, A. Liposomes and MTT Cell Viability Assay: An Incompatible Affair. *Toxicol. Vitr.* **2015**, *29* (2), 314–319. https://doi.org/10.1016/j.tiv.2014.11.009.

(89) Goodwin, C. J.; Holt, S. J.; Downes, S.; Marshall, N. J. The Use of Intermediate Electron Acceptors to Enhance MTT Bioreduction in a Microculture Tetrazolium Assay for Human Growth Hormone. *Life Sci.* **1996**, *59* (20), 1745–1753. https://doi.org/10.1016/S0024-3205(96)00512-7.

(90) Dhanjaland, P.; Fry, J. R. Determinants of MTT Reduction in Rat Hepatocytes. *Biomarkers* **2002**, *2* (2), 111–116. https://doi.org/10.1080/135475097231832.

(91) Maryott, A. A.; R., S. E. *Table of Dielectric Constants of Pure Liquids*; National Bureau of Standards circular, 1951.

(92) Chaudhuri, A.; Haldar, S.; Chattopadhyay, A. Organization and Dynamics in Micellar Structural Transition Monitored by Pyrene Fluorescence. *Biochem. Biophys. Res. Commun.* **2009**, *390* (3), 728–732. https://doi.org/10.1016/j.bbrc.2009.10.037.

(93) Steinebrunner, D.; Schnurpfeil, G.; Wöhrle, D.; Wittstock, A. Photocatalytic Coatings Based on a Zinc(Ii) Phthalocyanine Derivative Immobilized on Nanoporous Gold Leafs with Various Pore Sizes. *RSC Adv.* **2019**, *10* (1), 53–59. https://doi.org/10.1039/c9ra08841e.

(94) Espitia-Almeida, F.; Díaz-Uribe, C.; Vallejo, W.; Gómez-Camargo, D.; Romero Bohórquez, A. R. In Vitro Anti-Leishmanial Effect of Metallic Meso-Substituted Porphyrin Derivatives against Leishmania Braziliensis and Leishmania Panamensis Promastigotes Properties. *Molecules* **2020**, *25* (8), 1–11. https://doi.org/10.3390/molecules25081887.

(95) Blacha-Grzechnik, A.; Drewniak, A.; Walczak, K. Z.; Szindler, M.; Ledwon, P. Efficient Generation of Singlet Oxygen by Perylene Diimide Photosensitizers Covalently Bound to Conjugate Polymers. *J. Photochem. Photobiol. A Chem.* **2020**, *388*. https://doi.org/10.1016/j.jphotochem.2019.112161.

(96) Entradas, T.; Waldron, S.; Volk, M. The Detection Sensitivity of Commonly

Used Singlet Oxygen Probes in Aqueous Environments. *J. Photochem. Photobiol. B Biol.* **2020**, *204*. https://doi.org/10.1016/j.jphotobiol.2020.111787.

(97) Pibiri, I.; Buscemi, S.; Palumbo Piccionello, A.; Pace, A. Photochemically Produced Singlet Oxygen: Applications and Perspectives. *ChemPhotoChem* **2018**, *2* (7), 535–547. https://doi.org/10.1002/cptc.201800076.

(98) Pastore, D.; Laus, M. N.; Tozzi, D.; Fogliano, V.; Soccio, M.; Flagella, Z. New Tool to Evaluate a Comprehensive Antioxidant Activity in Food Extracts: Bleaching of 4-Nitroso-N,N-Dimethylaniline Catalyzed by Soybean Lipoxygenase-1. *J. Agric. Food Chem.* **2009**, *57* (20), 9682–9692. https://doi.org/10.1021/jf901509b.

(99) Fasnacht, M. P.; Blough, N. V. Kinetic Analysis of the Photodegradation of Polycyclic Aromatic Hydrocarbons in Aqueous Solution. *Aquat. Sci. - Res. Across Boundaries* **2003**, *65* (4), 352–358. https://doi.org/10.1007/s00027-003-0680-7.

(100) Ray, R. S.; Mujtaba, S. F.; Dwivedi, A.; Yadav, N.; Verma, A.; Kushwaha, H. N.; Amar, S. K.; Goel, S.; Chopra, D. Singlet Oxygen Mediated DNA Damage Induced Phototoxicity by Ketoprofen Resulting in Mitochondrial Depolarization and Lysosomal Destabilization. *Toxicology* **2013**, *314* (2–3), 229–237. https://doi.org/10.1016/J.TOX.2013.10.002.

(101) Li, B.; Lin, L.; Lin, H.; Wilson, B. C. Photosensitized Singlet Oxygen Generation and Detection: Recent Advances and Future Perspectives in Cancer Photodynamic Therapy. *J. Biophotonics* **2016**, *9* (11–12), 1314–1325. https://doi.org/10.1002/jbio.201600055.

(102) Trashin, S.; Rahemi, V.; Ramji, K.; Neven, L.; Gorun, S. M.; De Wael, K. Singlet Oxygen-Based Electrosensing by Molecular Photosensitizers. *Nat. Commun.* **2017**, *8* (16108). https://doi.org/10.1038/ncomms16108.

(103) García-Fresnadillo, D. Singlet Oxygen Photosensitizing Materials for Point-of-Use Water Disinfection with Solar Reactors. *ChemPhotoChem* **2018**, *2* (7), 512–534. https://doi.org/10.1002/cptc.201800062.

(104) You, Y. Chemical Tools for the Generation and Detection of Singlet Oxygen. *Org. Biomol. Chem.* **2018**, *16* (22), 4044–4060. https://doi.org/10.1039/c8ob00504d.

(105) Zhang, S. P.; Zhao, J. Q.; Jiang, L. J. Photosensitized Formation of Singlet Oxygen by Phycobiliproteins in Neutral Aqueous Solutions. *Free Radic. Res.* **2000**, *33* (5), 489–496. https://doi.org/10.1080/10715760000301031.

(106) Gottschalk, P.; Paczkowski, J.; Neckers, D. C. Factors Influencing the Quantum Yields for Rose Bengal Formation of Singlet Oxygen. *J. Photochem.* **1986**, *35* (3), 277–281. https://doi.org/10.1016/0047-2670(86)87059-9.

(107) W.H., S.; C.L., B.; Walker, R. A. Solvent Polarity across Weakly Associating Interfaces. *J Phys Chem B.* **2004**, *108* (41), 16107–16116.

(108) Bregnhøj, M.; Westberg, M.; Jensen, F.; Ogilby, P. R. Solvent-Dependent Singlet Oxygen Lifetimes: Temperature Effects Implicate Tunneling and Charge-Transfer Interactions. *Phys. Chem. Chem. Phys.* **2016**, *18* (33), 22946–22961. https://doi.org/10.1039/C6CP01635A.

(109) Kraljić, I.; Lindqvist, L. Laser Photolysis Study of Triplet Eosin and Thionine Reactions in Photosensitized Oxidations. *Photochem. Photobiol.* **1974**, *20* (4), 351–355. https://doi.org/10.1111/j.1751-1097.1974.tb06587.x.

(110) Burns, J. M.; Cooper, W. J.; Ferry, J. L.; King, D. W.; DiMento, B. P.; McNeill, K.; Miller, C. J.; Miller, W. L.; Peake, B. M.; Rusak, S. A.; Rose, A. L.; Waite, T. D. Methods for Reactive Oxygen Species (ROS) Detection in Aqueous Environments. *Aquat. Sci.* **2012**, *74* (4), 683–734. https://doi.org/10.1007/s00027-012-0251-x.

(111) Chen, X. Q.; Wang, F.; Hyun, J. Y.; Wei, T. W.; Qiang, J.; Ren, X. T.; Shin, I.; Yoon, J. Recent Progress in the Development of Fluorescent, Luminescent and Colorimetric Probes for Detection of Reactive Oxygen and Nitrogen Species. *Chem. Soc. Rev.* **2016**, *45* (10), 2976–3016. https://doi.org/10.1039/C6CS00192K.

Appendix

PERMISSIONS

A.1 Permissions for Chapter 1 Content

SPRINGER NATURE LICENSE
TERMS AND CONDITIONS

Jun 14, 2020

This Agreement between Mrs. Johanna Herman ("You") and Springer Nature ("Springer Nature") consists of your license details and the terms and conditions provided by Springer Nature and Copyright Clearance Center.

License Number	4847860780826
License date	Jun 14, 2020
Licensed Content Publisher	Springer Nature
Licensed Content Publication	Analytical and Bioanalytical Chemistry
Licensed Content Title	Emerging technologies for optical spectral detection of reactive oxygen species
Licensed Content Author	Johanna Herman et al
Licensed Content Date	Jul 28, 2018
Type of Use	Thesis/Dissertation
Requestor type	academic/university or research institute
Format	print and electronic
Portion	full article/chapter
Will you be	no

translating?	
Circulation/distribution	50000 or greater
Author of this Springer Nature content	yes
Title	Assessing the Efficiency of Reactive Oxygen Species Colorimetric Sensors in Environmentally & Biologically Relevant Conditions
Institution name	University of Delaware
Expected presentation date	Jun 2020
Requestor Location	Mrs. Johanna Herman University of Delaware 163 The Green 173 Brown Lab NEWARK, DE 19711 United States Attn: Mrs. Johanna Herman
Total	0.00 USD

Terms and Conditions

Springer Nature Customer Service Centre GmbH
Terms and Conditions

This agreement sets out the terms and conditions of the licence (the **Licence**) between you and **Springer Nature Customer Service Centre GmbH** (the **Licensor**). By clicking 'accept' and completing the transaction for the material (**Licensed Material**), you also confirm your acceptance of these terms and conditions.

1. Grant of License

1. 1. The Licensor grants you a personal, non-exclusive, non-transferable, world-wide licence to reproduce the Licensed Material for the purpose specified in your order only. Licences are granted for the specific use requested in the order and for no other use, subject to the conditions below.

1. 2. The Licensor warrants that it has, to the best of its knowledge, the rights to license reuse of the Licensed Material. However, you should ensure that the material you are requesting is original to the Licensor and does not carry the copyright of

another entity (as credited in the published version).

1. 3. If the credit line on any part of the material you have requested indicates that it was reprinted or adapted with permission from another source, then you should also seek permission from that source to reuse the material.

2. Scope of Licence

2. 1. You may only use the Licensed Content in the manner and to the extent permitted by these Ts&Cs and any applicable laws.

2. 2. A separate licence may be required for any additional use of the Licensed Material, e.g. where a licence has been purchased for print only use, separate permission must be obtained for electronic re-use. Similarly, a licence is only valid in the language selected and does not apply for editions in other languages unless additional translation rights have been granted separately in the licence. Any content owned by third parties are expressly excluded from the licence.

2. 3. Similarly, rights for additional components such as custom editions and derivatives require additional permission and may be subject to an additional fee. Please apply to Journalpermissions@springernature.com/bookpermissions@springernature.com for these rights.

2. 4. Where permission has been granted **free of charge** for material in print, permission may also be granted for any electronic version of that work, provided that the material is incidental to your work as a whole and that the electronic version is essentially equivalent to, or substitutes for, the print version.

2. 5. An alternative scope of licence may apply to signatories of the STM Permissions Guidelines, as amended from time to time.

3. Duration of Licence

3. 1. A licence for is valid from the date of purchase ('Licence Date') at the end of the relevant period in the below table:

Scope of Licence	Duration of Licence
Post on a website	12 months
Presentations	12 months
Books and journals	Lifetime of the edition in the language purchased

4. Acknowledgement

4. 1. The Licensor's permission must be acknowledged next to the Licenced Material in print. In electronic form, this acknowledgement must be visible at the same time as the figures/tables/illustrations or abstract, and must be hyperlinked to the journal/book's homepage. Our required acknowledgement format is in the Appendix below.

9. 1. Licences will expire after the period shown in Clause 3 (above).

9. 2. Licensee reserves the right to terminate the Licence in the event that payment is not received in full or if there has been a breach of this agreement by you.

Appendix 1 — Acknowledgements:

For Journal Content:
Reprinted by permission from [**the Licensor**]: [**Journal Publisher** (e.g. Nature/Springer/Palgrave)] [**JOURNAL NAME**] [**REFERENCE CITATION** (Article name, Author(s) Name), [**COPYRIGHT**] (year of publication)

For **Advance Online Publication papers:**
Reprinted by permission from [**the Licensor**]: [**Journal Publisher** (e.g. Nature/Springer/Palgrave)] [**JOURNAL NAME**] [**REFERENCE CITATION** (Article name, Author(s) Name), [**COPYRIGHT**] (year of publication), advance online publication, day month year (doi: 10.1038/sj.[JOURNAL ACRONYM].)

For Adaptations/Translations:
Adapted/Translated by permission from [**the Licensor**]: [**Journal Publisher** (e.g. Nature/Springer/Palgrave)] [**JOURNAL NAME**] [**REFERENCE CITATION** (Article name, Author(s) Name), [**COPYRIGHT**] (year of publication)

Note: For any republication from the British Journal of Cancer, the following credit line style applies:

Reprinted/adapted/translated by permission from [**the Licensor**]: on behalf of Cancer Research UK: : [**Journal Publisher** (e.g. Nature/Springer/Palgrave)] [**JOURNAL NAME**] [**REFERENCE CITATION** (Article name, Author(s) Name), [**COPYRIGHT**] (year of publication)

For **Advance Online Publication** papers:
Reprinted by permission from The [**the Licensor**]: on behalf of Cancer Research UK: [**Journal Publisher** (e.g. Nature/Springer/Palgrave)] [**JOURNAL NAME**] [**REFERENCE CITATION** (Article name, Author(s) Name), [**COPYRIGHT**] (year of publication), advance online publication, day month year (doi: 10.1038/sj.[JOURNAL ACRONYM])

For Book content:
Reprinted/adapted by permission from [**the Licensor**]: [**Book Publisher** (e.g. Palgrave Macmillan, Springer etc) [**Book Title**] by [**Book author**(s)] [**COPYRIGHT**] (year of publication)

Other Conditions:

Version 1.2

Questions? customercare@copyright.com or +1-855-239-3415 (toll free in the US) or +1-978-646-2777.

A.1 Permissions for Chapter 4 Content

SPRINGER NATURE LICENSE
TERMS AND CONDITIONS

Jun 14, 2020

This Agreement between Mrs. Johanna Herman ("You") and Springer Nature ("Springer Nature") consists of your license details and the terms and conditions provided by Springer Nature and Copyright Clearance Center.

License Number	4847860567925
License date	Jun 14, 2020
Licensed Content Publisher	Springer Nature
Licensed Content Publication	Analytical and Bioanalytical Chemistry
Licensed Content Title	Efficiency comparison of the imidazole plus RNO method for singlet oxygen detection in biorelevant solvents
Licensed Content Author	Johanna Herman et al
Licensed Content Date	Jun 15, 2019
Type of Use	Thesis/Dissertation
Requestor type	academic/university or research institute
Format	print and electronic
Portion	full article/chapter
Will you be	no

translating?	
Circulation/distribution	50000 or greater
Author of this Springer Nature content	yes
Title	Assessing the Efficiency of Reactive Oxygen Species Colorimetric Sensors in Environmentally & Biologically Relevant Conditions
Institution name	University of Delaware
Expected presentation date	Jun 2020
Requestor Location	Mrs. Johanna Herman University of Delaware 163 The Green 173 Brown Lab NEWARK, DE 19711 United States Attn: Mrs. Johanna Herman
Total	0.00 USD

Terms and Conditions

Springer Nature Customer Service Centre GmbH
Terms and Conditions

This agreement sets out the terms and conditions of the licence (the **Licence**) between you and **Springer Nature Customer Service Centre GmbH** (the **Licensor**). By clicking 'accept' and completing the transaction for the material (**Licensed Material**), you also confirm your acceptance of these terms and conditions.

1. Grant of License

1. 1. The Licensor grants you a personal, non-exclusive, non-transferable, world-wide licence to reproduce the Licensed Material for the purpose specified in your order only. Licences are granted for the specific use requested in the order and for no other use, subject to the conditions below.

1. 2. The Licensor warrants that it has, to the best of its knowledge, the rights to license reuse of the Licensed Material. However, you should ensure that the material you are requesting is original to the Licensor and does not carry the copyright of

another entity (as credited in the published version).

1. 3. If the credit line on any part of the material you have requested indicates that it was reprinted or adapted with permission from another source, then you should also seek permission from that source to reuse the material.

2. Scope of Licence

2. 1. You may only use the Licensed Content in the manner and to the extent permitted by these Ts&Cs and any applicable laws.

2. 2. A separate licence may be required for any additional use of the Licensed Material, e.g. where a licence has been purchased for print only use, separate permission must be obtained for electronic re-use. Similarly, a licence is only valid in the language selected and does not apply for editions in other languages unless additional translation rights have been granted separately in the licence. Any content owned by third parties are expressly excluded from the licence.

2. 3. Similarly, rights for additional components such as custom editions and derivatives require additional permission and may be subject to an additional fee. Please apply to Journalpermissions@springernature.com/bookpermissions@springernature.com for these rights.

2. 4. Where permission has been granted **free of charge** for material in print, permission may also be granted for any electronic version of that work, provided that the material is incidental to your work as a whole and that the electronic version is essentially equivalent to, or substitutes for, the print version.

2. 5. An alternative scope of licence may apply to signatories of the STM Permissions Guidelines, as amended from time to time.

3. Duration of Licence

3. 1. A licence for is valid from the date of purchase ('Licence Date') at the end of the relevant period in the below table:

Scope of Licence	Duration of Licence
Post on a website	12 months
Presentations	12 months
Books and journals	Lifetime of the edition in the language purchased

4. Acknowledgement

4. 1. The Licensor's permission must be acknowledged next to the Licenced Material in print. In electronic form, this acknowledgement must be visible at the same time as the figures/tables/illustrations or abstract, and must be hyperlinked to the journal/book's homepage. Our required acknowledgement format is in the Appendix below.

9. 1. Licences will expire after the period shown in Clause 3 (above).

9. 2. Licensee reserves the right to terminate the Licence in the event that payment is not received in full or if there has been a breach of this agreement by you.

Appendix 1 — Acknowledgements:

For Journal Content:
Reprinted by permission from [**the Licensor**]: [**Journal Publisher** (e.g. Nature/Springer/Palgrave)] [**JOURNAL NAME**] [**REFERENCE CITATION** (Article name, Author(s) Name), [**COPYRIGHT**] (year of publication)

For **Advance Online Publication papers:**
Reprinted by permission from [**the Licensor**]: [**Journal Publisher** (e.g. Nature/Springer/Palgrave)] [**JOURNAL NAME**] [**REFERENCE CITATION** (Article name, Author(s) Name), [**COPYRIGHT**] (year of publication), advance online publication, day month year (doi: 10.1038/sj.[JOURNAL ACRONYM].)

For Adaptations/Translations:
Adapted/Translated by permission from [**the Licensor**]: [**Journal Publisher** (e.g. Nature/Springer/Palgrave)] [**JOURNAL NAME**] [**REFERENCE CITATION** (Article name, Author(s) Name), [**COPYRIGHT**] (year of publication)

Note: For any republication from the British Journal of Cancer, the following credit line style applies:

Reprinted/adapted/translated by permission from [**the Licensor**]: on behalf of Cancer Research UK: : [**Journal Publisher** (e.g. Nature/Springer/Palgrave)] [**JOURNAL NAME**] [**REFERENCE CITATION** (Article name, Author(s) Name), [**COPYRIGHT**] (year of publication)

For **Advance Online Publication** papers:
Reprinted by permission from The [**the Licensor**]: on behalf of Cancer Research UK: [**Journal Publisher** (e.g. Nature/Springer/Palgrave)] [**JOURNAL NAME**] [**REFERENCE CITATION** (Article name, Author(s) Name), [**COPYRIGHT**] (year of publication), advance online publication, day month year (doi: 10.1038/sj.[JOURNAL ACRONYM])

For Book content:
Reprinted/adapted by permission from [**the Licensor**]: [**Book Publisher** (e.g. Palgrave Macmillan, Springer etc) [**Book Title**] by [**Book author**(s)] [**COPYRIGHT**] (year of publication)

Other Conditions:

Version 1.2

Questions? customercare@copyright.com or +1-855-239-3415 (toll free in the US) or +1-978-646-2777.